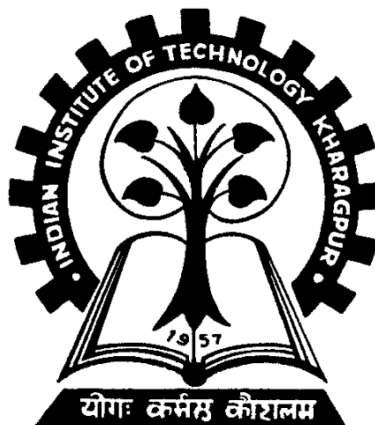


Seismic Moment Tensor Inversion in Alaska using Body and Surface waves

Thesis by
Vipul Silwal

In Partial Fulfillment of the Requirements for the Degree of
Master of Science

Under the guidance of
Prof William Mohanty and Prof Carl Tape



Department of Geology and Geophysics

Indian Institute of Technology

Kharagpur

May 2012

Certificate

This is to certify that the thesis entitled “SEISMIC MOMENT TENSOR INVERSION IN ALASKA USING BODY AND SURFACE WAVES” is an authentic record of the work carried out by **Mr Vipul Silwal (Roll No 07EX2001)** under our guidance and supervision. The thesis is submitted to the Department of Geology and Geophysics, Indian Institute of Technology, Kharagpur, in the partial fulfillment of the requirements for the degree of Master of Science in Exploration Geophysics during the academic year 2011-2012.

Date:

Dr. William K. Mohanty
Associate Professor
Department of Geology and Geophysics
Indian Institute of Technology
Kharagpur



April 26, 2012

Dr. Carl Tape
Assistant Professor
Department of Geology and Geophysics
University of Alaska
Fairbanks, USA

Prof. Biswajit Mishra
Head of the Department
Department of Geology and Geophysics
Indian Institute of Technology
Kharagpur

Acknowledgement

I thank Prof. Carl Tape and University of Alaska Fairbanks, for providing me the internship opportunity in summer last year which lead to the inception of this project. Prof. Tape has been a great guide, teacher and motivator throughout this journey. I certainly have learnt a lot from his constant guidance, insight, way of approach to the problem and knowledgeable discussions. He also introduced me to the whole new world of research which has helped me choose what career to pursue in life. I definitely look forward to continue working with him in future.

I thank Prof. William Mohanty for providing constant support during this project. Without his support and guidance this project would have been incomplete. I also thank all the faculty of Department of Geology and Geophysics, IIT Kharagpur for introducing me to Earth Sciences and Seismology. I thank Prof. S. K. Nath for his wonderful, scientific and motivating lectures on Seismology.

We had to face many logistical difficulties while shifting the working base from Geological Institute (GI) to IIT Kharagpur. During this phase Computer and Informatics Center (CIC) provided great support and facility to access the GI server (UAF) from IIT. Whole of this project have been completed on the server that is set up at GI. I thank all the people who keep the server up and running.

I would also like to thank Prof. Roger Hansen and Alaska Earthquake Information Center (AEIC) for making the data and seismograms readily available, without which, this thesis would have never completed. I also thank Prof. Mike West (UAF) for the valuable discussions and comments. He also provided us with many codes which had helped us a lot in completion of this project. I am thankful to Prof. L Zhu (Saint Louis University) for providing the reflectivity code, FK-synthetics (for green's function) and CAP inversion code.

Last but not the least, I would like to thank IIT Kharagpur which have been a wonderful place to live and learn. I would like to thank my friends and colleagues for making it even more amazing without which this journey would have been incomplete.

Finally, I would like to dedicate this thesis to my loving mom and dad. They have not only been great parents, but also a motivating teacher and supporting friend. They have helped me achieve whatever I aspired to.

Abstract

Due to our inability to map the extreme heterogeneity of earth, there will always be inherent errors in any earth model that we assume. With the use of this erroneous earth model, we will never be able to achieve accurate green's function and hence the synthetics. We can compensate for the errors in green's functions by allowing differential time shifts between the principal crustal arrivals (*Zhao and Helmberger (1994)*). In Cut-and-Paste approach the waveform is divided into 5 parts: Pnl V, Pnl R, Surf V, Surf R and SH; and then each phase is fitted independently while allowing for a acceptable amount of shift.

Two kinds of waveforms are used for source estimation: body waves and surface waves. Generally, the body waves are less affected by shallow heterogeneities and are more stable than surface waves (*Zhu and Helmberger (1996)*). Inversion in itself is more stable at longer period because of higher S/N ratio. While using full waveform for carrying out inversion at long period, it is the surface wave which generally dominates. Long period inversion provide us with more stability but restricts the full utilization of station records. With the advent of broadband seismometry, it calls upon for methods that make full utilization of its wide range.

In this thesis I present the focal mechanism solution for 3 different Alaska earthquakes: eid 319605, eid 289317 and Nenana earthquake. Eid 319605 serves as an example of shallow event with 45 km depth and Normal faulting mechanism. Eid 289317 serves as an example of deep event with 165 km depth and has a major component of reverse faulting mechanism. Deep events in general produce stronger body wave than shallow ones. We used long period body waves (6.6 - 20 sec) and surface waves (16.6 - 50 sec) for these events. Both these events were of magnitude $M_w > 4.5$ and hence long period waveforms could be used. For smaller events, we need to go at even higher frequency for a stable moment tensor solution.

We also present the solution of Nenana earthquake, 11 April 2012, $M_w 3.8$. The earthquake triggered during the passage of the peak of love waves generated by Sumatra earthquake. For a stable solution of this event we used body waves in 1 - 3 sec, and surface waves in 2 - 4 sec range. Inversion resulted in a predominant strike-slip mechanism very much similar to 1995 earthquake that occurred in same fault system. The solutions obtained by CAP inversion have also been compared with those obtained by AEIC. For these tests we have only considered the deviatoric part (double couple solution) and have not estimated the isotropic component unlike that of AEIC.

Contents

Certificate	ii
Acknowledgement	iii
Abstract	iv
1 Introduction	1
1.1 Study Region	2
1.2 Tectonic setting and Structural Model	2
2 Seismic Moment Tensor	8
2.1 Moment Tensor	8
2.1.1 Single forces	8
2.1.2 Force couples	9
2.1.3 Double couple	9
2.1.4 Isotropic and CLVD moment tensors	11
3 Forward Modeling	13
3.1 Equation of motion	13
3.2 Betti's, Green's and Representation	14
3.2.1 Synthetic Seismogram	15
3.3 Numerical Modeling	15
3.4 Basic working of reflectivity code	16
3.5 Preparing Synthetics	20
3.5.1 Model Used	20
3.5.2 Azimuthal check	20
3.5.3 Depth check	20
3.5.4 Epicentral distance check	20
3.5.5 Compatibility of double couple and fault	21
3.5.6 Testing different models	21
3.6 Synthetics for various Alaska models	30
3.7 Comparision between 1D synthetics from SPECFEM3D and FK	33

4 CAP Inversion	36
4.1 Basic Idea	36
4.2 Test events	38
4.2.1 Depth Estimate	38
4.3 AEIC Moment Tensor Inversion	39
4.4 EXAMPLE EVENT (eid 319605)	40
4.4.1 Stations: MOOS and AEIC	40
4.4.2 AEIC inversion	41
4.4.3 Commands used	41
4.4.4 CAP output details	41
4.4.5 Structural Model	42
4.4.6 Surface wave Inversion	43
4.4.7 Observational Conclusion:	43
4.4.8 Body wave Inversion	47
4.4.9 Inversion with Body and Surface waves	50
4.4.10 Results	55
4.5 EXAMPLE EVENT 2 (eid 289317)	57
4.5.1 Comparison: AEIC moment tensor solution with CAP	57
4.5.2 Results	60
4.5.3 ‘tshift’ plot	60
4.6 Special event: Nenana earthquake	69
4.6.1 Sumatra earthquake	69
4.6.2 CAP inversion	69
4.6.3 Results	70
4.6.4 Record section	72
4.6.5 Tectonic setting	74
4.6.6 CAP_MT inversion	76
5 Results and Conclusions	78
A Propagator Matrix Method	80
A.1 Seismic Waves	80
A.1.1 Surface wave dispersion (<i>Aki and Richards</i> , 1980)	81
A.1.2 Displacement-Stress vector (<i>Aki and Richards</i> , 1980)	81
A.1.3 Propagator Matrix(<i>Udias</i> , 1999)	85
Bibliography	89

List of Figures

1.1	Study region: Alaska	4
1.2	South central Alaska Map	5
1.3	P and S wave velocity variation with depth for different Alaska models	6
1.4	Comparison of SCAK and TACTMOD	7
2.1	Moment Tensor Force couples	12
3.1	Azimuthal test	23
3.2	Source depth check	24
3.3	Epicentral distance check	25
3.4	Homogeneous SOCAL model	26
3.5	Radiation directivity for homogeneous SOCAL model	27
3.6	Energy dominance of different phases	27
3.7	Depth test for homogeneous SOCAL	28
3.8	Single crustal layer: SOCAL	29
3.9	Density variation with depth for different Alaska models	30
3.10	Radial component seismogram using different Alaska models	31
3.11	Transverse component seismogram using different Alaska models	32
3.12	Comparison between synthetics from SPECFEM3D and FK - 1	34
3.13	Comparison between synthetics from SPECFEM3D and FK - 2	35
4.1	Pnl phase	37
4.2	Depth variation between AEIC catalog and MT inversion	39
4.3	AEIC moment tensor solution for 319605	41
4.4	CAP moment tensor inversion of 319605 using surface waves (cont'd.)	45
4.5	Depth estimation of 319605 (surface wave inversion)	47
4.6	CAP moment tensor inversion of 319605 using body waves	49
4.7	Depth estimation of 319605 (body wave inversion)	50
4.8	MT solution for 319605 using both body and surface waves	52
4.9	Depth estimation of 319605 using both the surface and the body waves	55
4.10	319605 beachball plot	56
4.11	AEIC moment tensor solution for 289317	57

4.12 Record section of 289317 at 60 stations	58
4.13 CAP moment tensor solution for 289317	59
4.14 'tshift' plot for 289317	61
4.15 Sumatra Earthquake	71
4.16 Surface waves from Sumatra earthquake	72
4.17 Nenana Earthquake	73
4.18 Interior Alaska map	74
4.19 Map showing 2012 and 1995 Nenana events	75
4.20 CAP inversion of 2012 Nenana event	76
4.21 Depth estimation of 2012 Nenana event	77
A.1 Love wave dispersion in a single layer over half sapce	82
A.2 Stratified layer over half-sapce	86

Chapter 1

Introduction

Inaccuracy in the structural model (velocity model) have always been a major setback while trying to obtain a moment tensor solution of any earthquake. This moment tensor solution helps in defining the faulting mechanism of the earthquake. But due to an inherent inaccuracy in the velocity model, we always incorporate some error in the green's function. During inversion, for obtaining a good solution, we match the synthetics obtained from green's function and the recorded data, and try to minimize the misfit error. In a 1-D structural model with gradually increasing velocity, the errors in the green's function would cause misalignment of the arrival of different phases i.e. body wave or surface wave either coming slightly earlier or late depend on how fast or slower our model is from the actual model. To compensate for these errors, we allow for slight shifting of different phases when trying to match the data and the synthetics. This approach is known as Cut-and-Paste approach (CAP) and had been developed by (*Zhao and Helmberger, 1994*) and (*Zhu and Helmberger, 1996*).

The thesis have be mainly divided into two parts. First part deals with Forward modeling and preparation of green's function and synthetic seismograms. This is the most important on primarily the most fundamental step towards any inversion process. In the second part, inversion results have been shown for three different earthquakes. Prior to that, a brief introduction about moment tensor have been presented in Chapter 2.

The forward problem deals with the preparation of green's function and synthetic seismograms. The underlying differential equations and the related boundary conditions, for the propagation of seismic waves through a realistic media is so complicated that it often very difficult and even impossible to find the solutions analytically. Numerical seismic modelling methods may be divided into three main categories: direct methods, integral-equation methods and ray-tracing methods. For the preparation of this thesis, I used direct method (reflectivity code by L Zhu). This requires double fourier integration over frequency and wavenumber domain and hence sometimes referred as FK-synthetics. More details about forward modelling, FK-synthetics and example figure have been presented in Chapter 3.

Finally, in Chapter 4 I present the results of CAP for three different Alaska earthquakes. The results have been compared with those that have been estimated by AEIC (Alaska Earthquake Information Center).

1.1 Study Region

Alaska is one of the most tectonically active regions in the world. It experiences more than half of the earthquakes recorded in Northern America. More than 80 percent of the planet's tremors occur in the circum-Pacific belt, and about six percent of the large, shallow earthquakes are in the Alaska area, where as many as 4,000 earthquakes at various depths are detected in a year. At the northwest corner of the North America, Alaska is situated at the receiving end of the Pacific Plate as it slides laterally past southeast Alaska and collides directly with the North American Plate across south-central Alaska and along the length of Aleutian Island Chain.

In this thesis, I have presented the seismic moment tensor solution of 3 different earthquakes of Alaska. They are different in **magnitude**, **hypocentral depth**, **focal mechanism** and perhaps most importantly the cause of triggering (discussed for one). The most special event being the one which seem to triggered by the passage of huge love waves generated by the Sumatra earthquake. Since this earthquake occurred in different regions, different structural models were used for generating the synthetics. Two of the events occurred in southern Alaska region, whereas one in the interior Alaska. The major earthquakes that have been investigated along with the seismic stations used have been shown in Figure 1.2.

1.2 Tectonic setting and Structural Model

Earthquake activity in Alaska is concentrated along the boundary between the Pacific Plate and the North America continent, as well as in the interior of Alaska where tectonic stresses are translated from the plate boundary. Earthquakes of large magnitude occur at depth along the Aleutian Megathrust; the fault surface on which the Pacific Plate slides beneath Alaska as it is subducted into the earth's mantle. Earthquakes of small to large magnitude are also distributed throughout southeastern, **south-central (SCAK)**, **interior (TACTMOD)**, and northern Alaska at shallower depths within the crust. This crustal earthquake activity is concentrated along several major faults that allow for the displacement of segments of the crust being pushed into southern Alaska by the collision with the Pacific Plate.

Despite of substantial seismic activities and the richness in the seismic data, little is known about the geologic setting. Since the geological setting is very complex, different structural models have been proposed for different regions. The two most important structural model

used in thesis were for South Central Alaska (SCAK) and Central Alaska (TACTMOD). For purpose of estimation of moment tensor three structural models are use:

1. SCAK Includes southern and south-central Alaska combined (except Aleutian). For regions below 62.5N and east of 157W.
2. TACTMOD Includes interior and Northern Alaska combined. For region above 62.5N.
3. ALEUT Used for Aleutian Island range west of 157 W.

Each of the region of study (SCAK and TACTMOD) have a sedimentary basin. Cook Inlet basin in south-central Alaska and Nenana basin in the interior Alaska. Both of these act as low velocity layer and have a significant impact in perturbing the seismic signal prominently by damping the amplitude and trapping the energy in top layer (causing reverberations and later arrivals of seismic phases in waveform).

SCAK (*Matumoto and Page, 1969*)

thickness	V_s	V_p	density	Q_p	Q_s
4.0000	3.0100	5.3000	2.5200	300.0000	600.0000
5.0000	3.1800	5.6000	2.6100	300.0000	600.0000
5.0000	3.5200	6.2000	2.7800	300.0000	600.0000
5.0000	3.9200	6.9000	2.9700	300.0000	600.0000
5.0000	4.2000	7.4000	3.1200	300.0000	600.0000
9.0000	4.3700	7.7000	3.2000	300.0000	600.0000
16.0000	4.4900	7.9000	3.2600	300.0000	600.0000
17.0000	4.6000	8.1000	3.3200	300.0000	600.0000
0	4.7200	8.3000	3.3700	300.0000	600.0000

TACTMOD (*Brocher et al., 1992*)

thickness	V_s	V_p	density	Q_p	Q_s
3.0000	3.0700	5.4000	2.5500	300.0000	600.0000
8.0000	3.3500	5.9000	2.6900	300.0000	600.0000
13.0000	3.5500	6.2500	2.7900	300.0000	600.0000
7.0000	4.0300	7.1000	3.0300	300.0000	600.0000
45.0000	4.4900	7.9000	3.2600	300.0000	600.0000
0.0000	4.7100	8.2900	3.3700	300.0000	600.0000

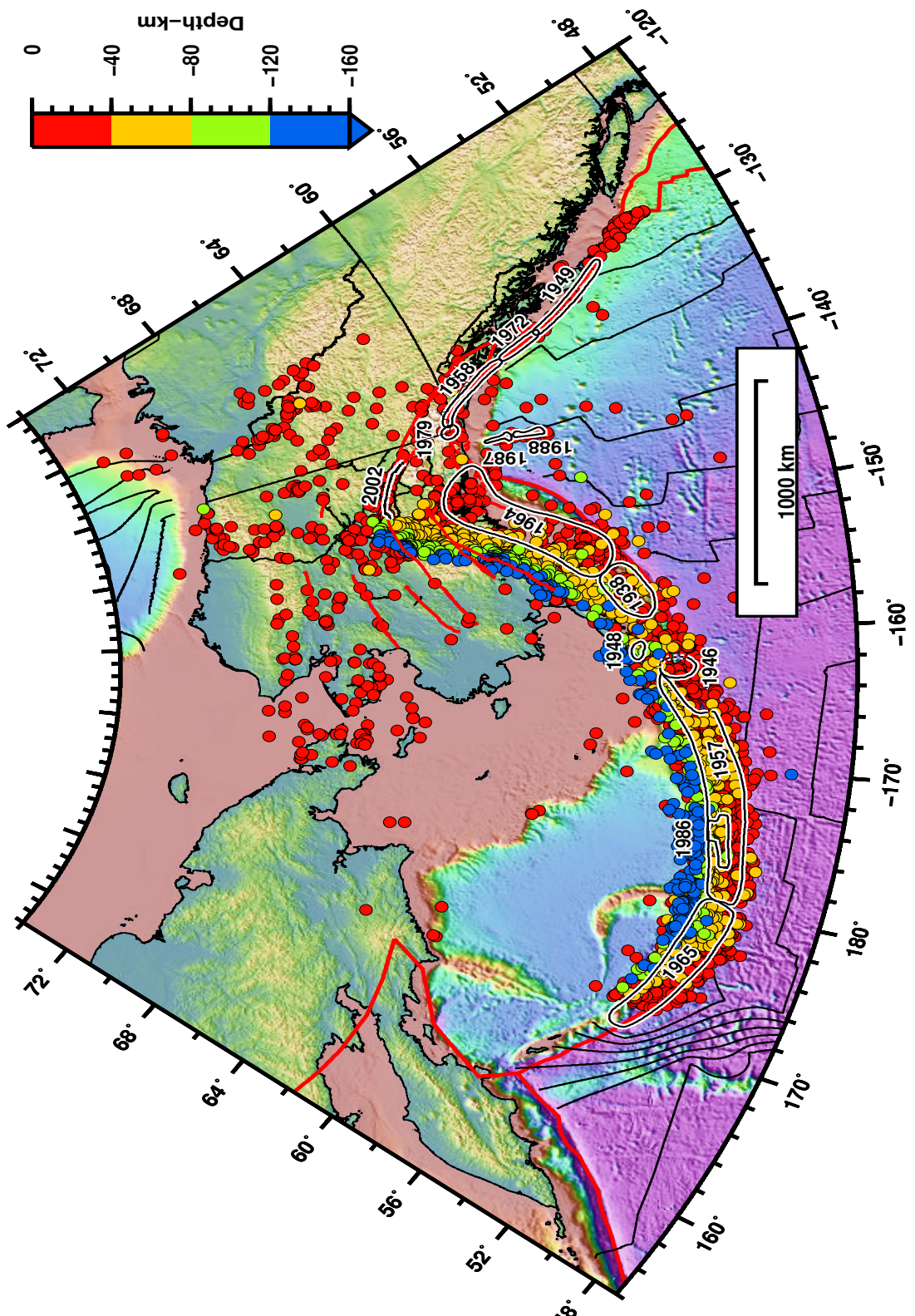


Figure 1.1: Study region: Seismicity map of Alaska; aftershock zones of major earthquakes, contours of plate age, seismicity $M \geq 4$ from 1990 to 2010 AEIC catalog.

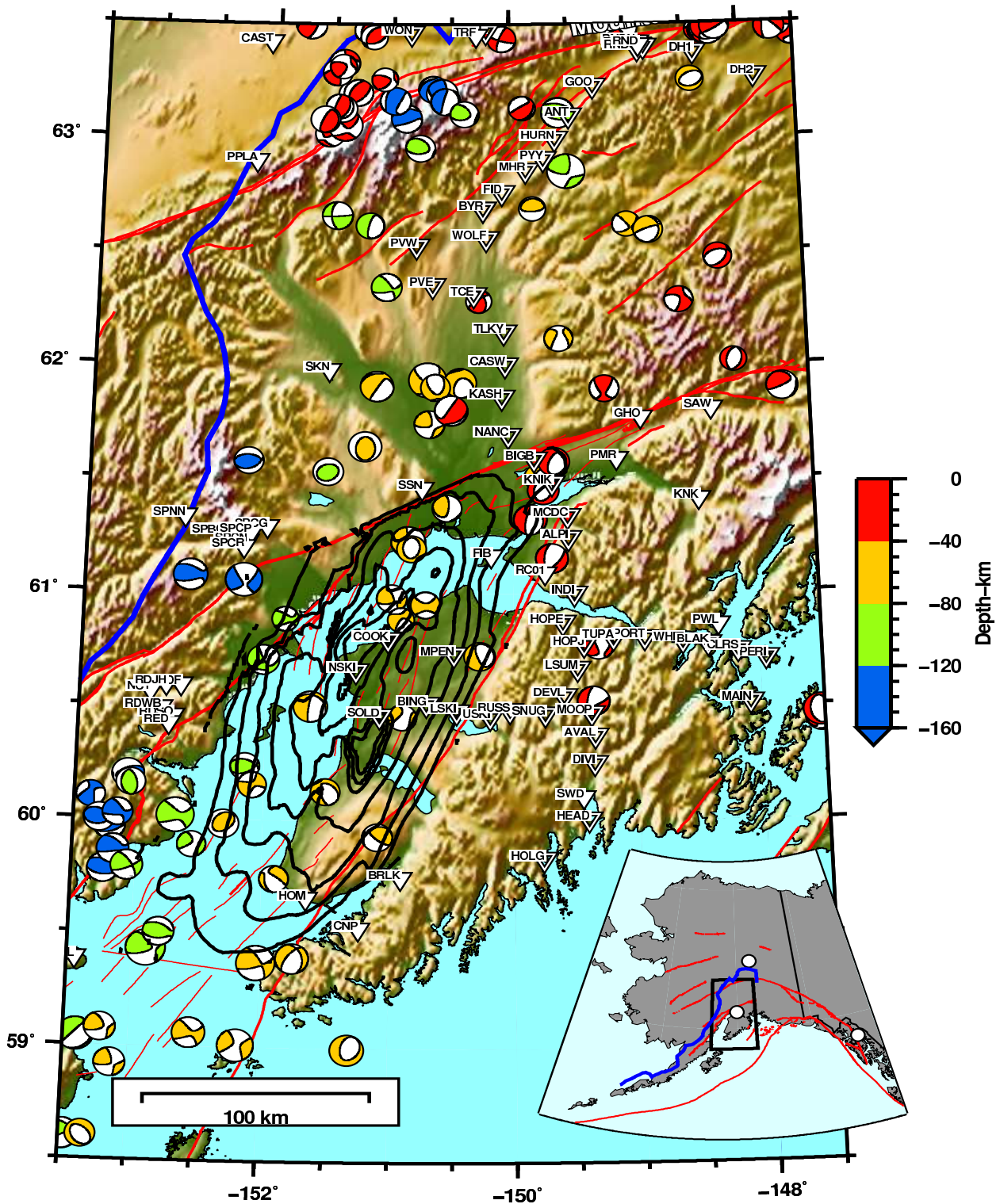


Figure 1.2: South central Alaska (SCAK) map showing major events and MOOS seismic array (Black contour shows Cook Inlet basin; Red lines marks the faults; Blue lines for rivers).

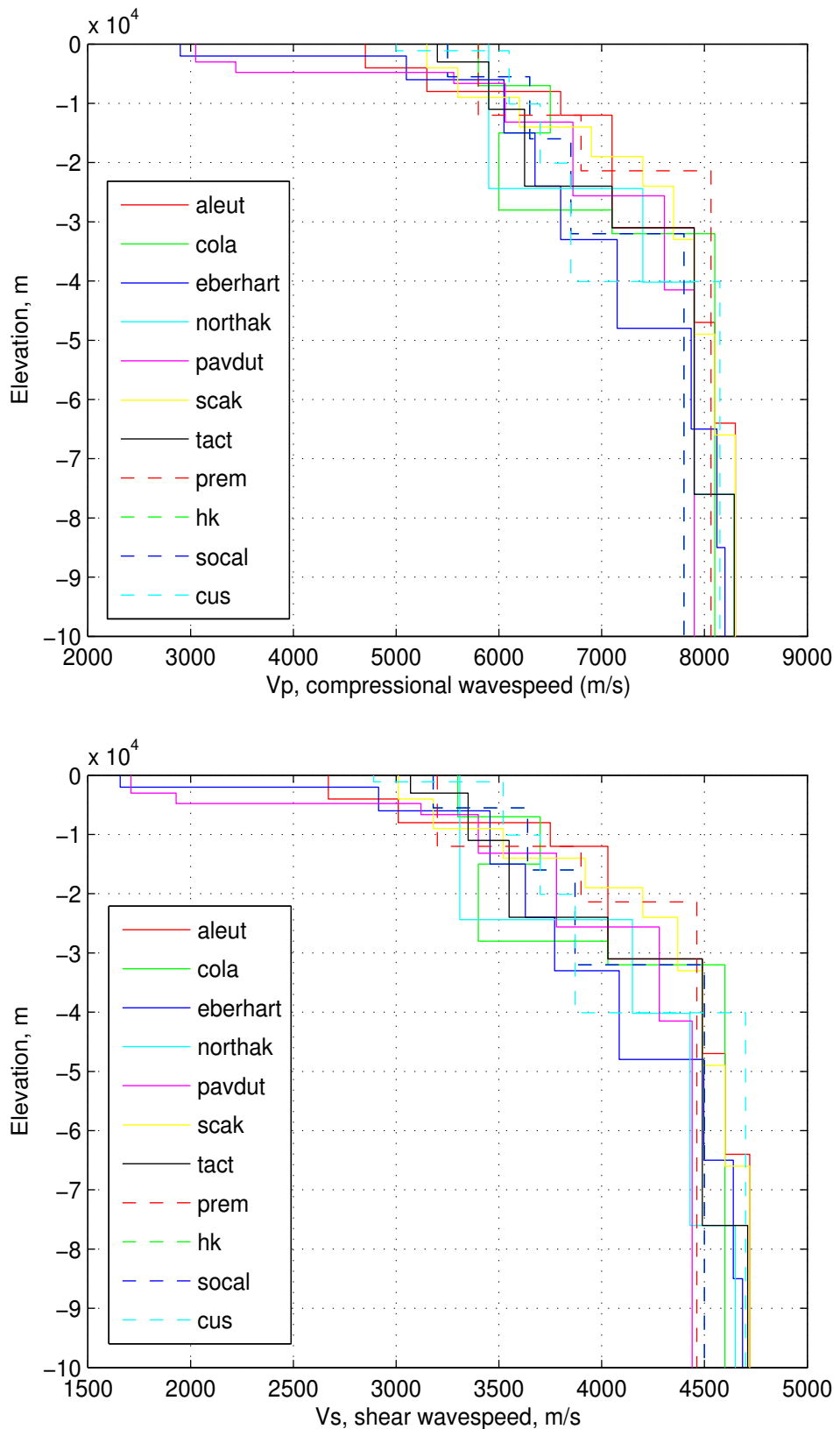


Figure 1.3: Comparative plot of different P and S wave velocity models used for Alaska.

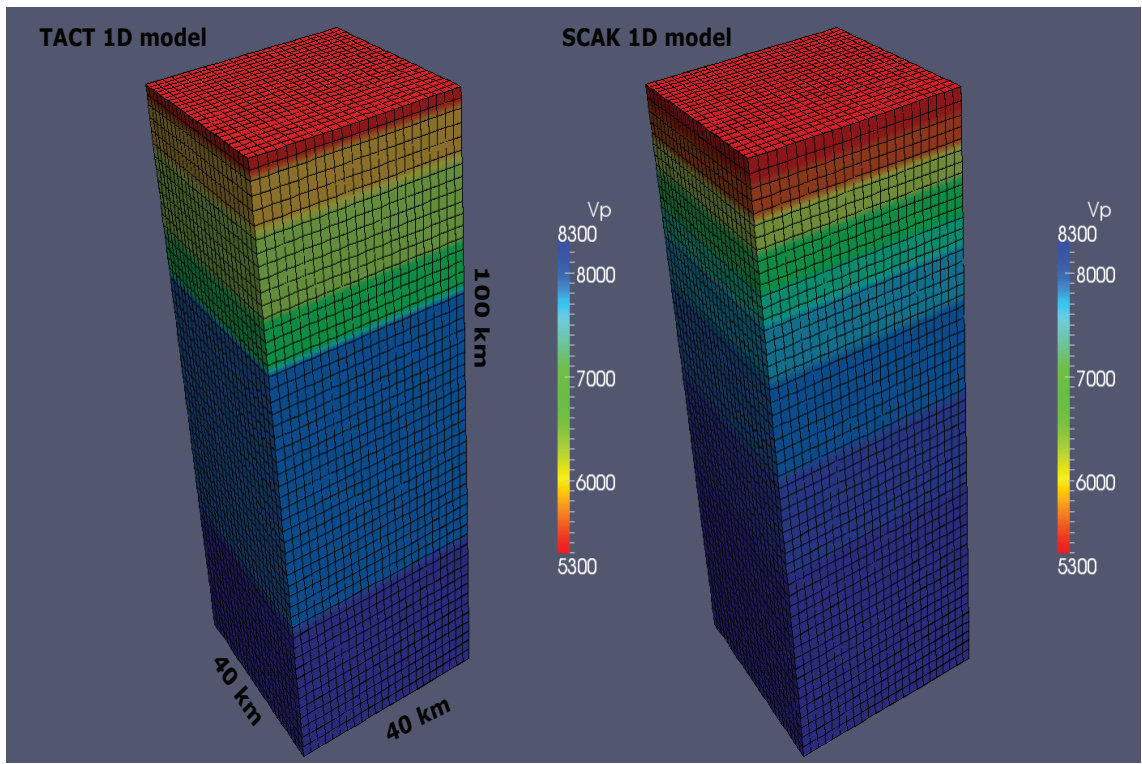


Figure 1.4: Comparison of two different structural model: TACT and SCAK (courtesy : Carl Tape)

Chapter 2

Seismic Moment Tensor

Earthquakes generally occur on fault plane and have a characteristic strike, dip and rake that defines it. Though it must be remembered that it is only a logical approximation of what actually happens during the rupture inside the 'black box'. The elastic rebound theory hypothesizes that shearing motions on fault occur when the elastic strain accumulation in the vicinity of the fault overcomes the static frictional stress that resists it. Sliding motion initiates at a point (the earthquake hypocenter), and a slip front expands outwards over the fault, separating regions that are slipping from regions that have not yet slipped. The radiation pattern generated due to the motion on the fault plane is similar to what would occur for a pair of force couples. If one couple is oriented in slip direction along the fault, the other would be oriented in the corresponding direction on opposite sides of the auxiliary plane (*Stein and Wysession, 2005*). Thus the radiation resulting from faulting can be also be described as if generated by this *double couple sources* and *equivalent body forces*. However, this combination is just one combination of forces; likewise others can be described as *single force and single couple*.

2.1 Moment Tensor

Seismic waves are generated by many processes apart from earthquakes. Typically this happens when the stress changes in very brief interval of time. For prolonged period of applied stress, earth behaves as a plastic body and shows creep mechanism. Such changes can be studied by geodetic methods.

2.1.1 Single forces

There are many geophysical phenomena which can be well explained by considering a single force acting in a certain direction. Examples:

1. Volcanic Eruption: A typical example would be 1980's explosive volcanic eruption of Mt. St. Helens. The radiation pattern generated by its eruption could be better explained by considering single force rather than double couple.
2. Landslides: They are usually modelled by considering a single force in the direction opposite that of the rock flow.
3. Meteor impacts: It is generally thought that such events should be modelled by a single vertical force. But the impact's energy is so large that it would vaporize rock and cause a spherically symmetric explosion similar to an underground explosion.

2.1.2 Force couples

Force couple M_{xy} consist of pair of forces f acting in opposite direction along x -axis, separated by a distance d apart along the y -axis. No geophysical process have been well modeled as single couple, probably because of the large unbalanced torque.

2.1.3 Double couple

Earthquakes are best represented by considering a force double couple. The total moment tensor is then represented as $\mathbf{M} = M_0(M_{xy} + M_{yx})$ if the fault is in $y - z$ plane ($x - z$ plane being the auxiliary plane. The Harvard centroid moment tensor (CMT)(up-south-east) representation of the seismic source is given as

$$\mathbf{M} = \begin{bmatrix} M_{rr} & M_{r\theta} & M_{r\phi} \\ M_{r\theta} & M_{\theta\theta} & M_{\theta\phi} \\ M_{r\phi} & M_{\theta\phi} & M_{\phi\phi} \end{bmatrix} \quad (2.1)$$

The corresponding Aki (north-east-down) representation :

$$\mathbf{M} = \begin{bmatrix} M_{zz} & M_{zx} & -M_{zy} \\ M_{xz} & M_{xx} & -M_{xy} \\ -M_{yz} & -M_{yx} & M_{yy} \end{bmatrix} \quad (2.2)$$

The conversion to Aki representation of moment tensor was required in order to be supplied as input to FK-synthetics code (by Zhu) for calculation of synthetic seismogram.

Calculation of seismic moment (M_0)

$$M_0 \equiv \frac{1}{\sqrt{2}} \|\mathbf{M}\|_F \quad (2.3)$$

$$= \frac{1}{\sqrt{2}} (\mathbf{M} : \mathbf{M})^{1/2} \quad (2.4)$$

$$= \frac{1}{\sqrt{2}} [M_{rr}^2 + M_{\theta\theta}^2 + M_{\phi\phi}^2 + 2(M_{r\theta}^2 + M_{r\phi}^2 + M_{\theta\phi}^2)]^{1/2}, \quad (2.5)$$

Finding the moment magnitude (M_w) from scalar seismic moment (M_0)

We can find moment magnitude, M_w , from scalar seismic moment by means of empirical relationship given by (Kanamori, 1977)

$$M_w = \frac{2}{3} \log_{10} M'_0 + k', \quad (2.6)$$

Finding moment tensor from fault parameters

Moment tensor (aki and richards) can be calculated from fault parameters in following manner:

$$\begin{aligned} M_{xx} &= -M_0 (\sin\delta \cos\lambda \sin 2\phi + \sin 2\delta \sin\lambda \sin^2\phi) \\ M_{yy} &= M_0 (\sin\delta \cos\lambda \sin 2\phi - \sin 2\delta \sin\lambda \cos^2\phi) \\ M_{zz} &= M_0 (\sin 2\delta \sin\lambda) \\ M_{xy} &= M_0 (\sin\delta \cos\lambda \cos 2\phi + 0.5 \sin 2\delta \sin\lambda \sin 2\phi) \\ M_{xz} &= -M_0 (\cos\delta \cos\lambda \cos 2\phi + \cos 2\delta \sin\lambda \sin\phi) \\ M_{yz} &= -M_0 (\cos\delta \cos\lambda \cos 2\phi - \cos 2\delta \sin\lambda \cos\phi) \end{aligned} \quad (2.7)$$

Here it can be seen that M_{zz} can be represented as $-(M_{xx} + M_{yy})$. Hence for a pure double couple number of independent parameters reduce to 5. Therefore, the trace of moment tensor matrix is 0. A nonzero trace implies a volume change (explosion or implosion).The properties of moment tensor matrix are very much similar to those of stress tensor matrix but they both represent different quantities. Stress tensor matrix relates normal and traction vectors, whereas moment tensor matrix represents normal and slip vectors.

Using the definition of the normal and slip vectors in terms of fault strike, dip and slip direction, we can write the moment tensor for any fault. The reverse process of finding the fault geometry corresponding to a moment tensor is more complicated. This is because it is possible that moment tensor may represent something more than just a double couple (no volume change). It is important because we primarily do

inversion for moment tensor, so that we can also get quantify the amount of non-double couple moment. It can be shown that eigenvectors of the moment tensor are parallel to the T, P and null axis.

$$\begin{aligned}\mathbf{t} &= \mathbf{n} + \mathbf{d} \\ \mathbf{p} &= \mathbf{n} - \mathbf{d} \\ \mathbf{b} &= \mathbf{n} \times \mathbf{d}\end{aligned}\tag{2.8}$$

Using general description of moment tensor elements $M_{ij} = M_0(n_i d_j + n_j d_i)$, it can be shown that \mathbf{t} is an eigenvector which has an eigenvalue of M_0 . Similary, $-M_0$ is the eigenvalue associated with \mathbf{p} , which is also an eigenvector. Null axis have 0 eigenvalue associated with it. The fact that P, T and null axes are the eigenvectors of the moment tensor lets us simplify it by transforming it into a natural coordinate system whose basis vectors are the eigenvectors. This process is commonly known as a diagonalizing and can be done by $U^{-1}\mathbf{M}U$, where U is the eigenvector matrix. Such orthogonal transformation changes on the components of moment tensor matrix, not its physical meaning.

2.1.4 Isotropic and CLVD moment tensors

Isotropic component is due to a *triple vector dipole* which has three equal and orthogonal force couple. It represents an implosive or explosive source and have a net volume change (nonzero trace).

Compensated linea vector dipoles (CLVD) have one dipole -2 times the magnitude of the others:

$$\mathbf{M} = \begin{bmatrix} M_0 & 0 & 0 \\ 0 & M_0 & 0 \\ 0 & 0 & -2M_0 \end{bmatrix}\tag{2.9}$$

There are two explanations of CLVD component in any seismic moment tensor:

1. Earthquakes occurring near the volcanoes usually have significant CLVD component. The moment tensor for such a crack opening under tension (inflating magma dyke), can be represented as a sum of isotropic and CLVD part.
2. A CLVD moment tensor can be decomposed into two double couples differing in seismic moment by a multiple of 2. Thus nearby earthquakes can sometimes be

misinterpreted as a single CLVD.

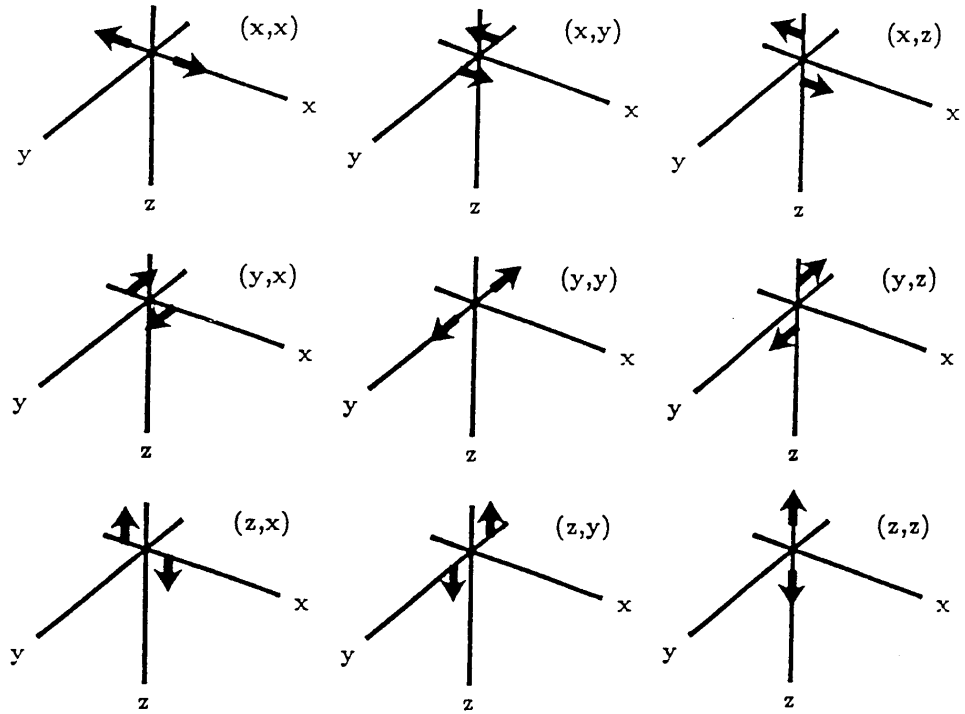


Figure 2.1: Nine force couples which are the components of the seismic moment tensor. (Stein and Wysession, 2005)

Chapter 3

Forward Modeling

Seismic waves starts from a source and propagate outwards through the media, and are then recorded at far stations. These waves are solutions of certain differential equations under certain boundary conditions (dynamic and kinematic). Under normal consideration, these equations gets so complicated that it becomes almost impossible to solve them analytically. Therefore, we incorporate different numerical techniques for solving these equations in a faster and efficient manner. Before dealing with different types of numerical techniques and choosing the best one (based on problem at hand and availability of machinery), let us first look at the theory underlying the representation of seismic waves through the body forces acting at distance.

3.1 Equation of motion

Working on the lines of Newton's second law of motion (conservation of momentum) one can easily derive equation of motion for seismic wavefields. Before considering the analogy of Newton's law of motion we must be aware that particle and continuum mechanics are two distinct theories and by suitable weakening continuum mechanics we can obtain particle mechanics (*Slawinski*, 2010)

$$\int_V \mathbf{f} dV + \int_S \boldsymbol{\tau} \cdot \hat{\mathbf{n}} dS = \int_V \rho \frac{\partial^2 \mathbf{u}}{\partial t^2} \quad (3.1)$$

where the 3×3 tensor $\boldsymbol{\tau}$ denotes stress, $\hat{\mathbf{n}}$ is the unit vector everywhere normal to S , \mathbf{u} denotes displacement and t time. We can change the second term on left hand side to volume integral by applying the divergence theorem. Rewriting after taking divergence and dropping the dV (since it is always present and now on both sides of equation),

$$\rho \frac{\partial^2 \mathbf{u}}{\partial t^2} - \mathbf{f} - \nabla \cdot \boldsymbol{\tau} = 0 \quad (3.2)$$

3.2 Betti's, Green's and Representation

Enrico Betti, an Italian mathematician, proved that, for a displacement field \mathbf{u} associated with stress $\boldsymbol{\tau}$ and force-per-unit-volume \mathbf{f} satisfying equation 3.2, and a displacement field \mathbf{v} likewise associated with stress $\boldsymbol{\sigma}$ and force-per-unit-volume \mathbf{g} , both applied on a body of volume V and bounded by a surface S , the following scalar equality holds:

$$\int_V (\mathbf{f} - \rho \ddot{\mathbf{u}}) \cdot \mathbf{v} dV + \int_S \mathbf{v} \cdot \boldsymbol{\tau} \cdot \hat{\mathbf{n}} dS = \int_V (\mathbf{g} - \rho \ddot{\mathbf{v}}) \cdot \mathbf{u} dV + \int_S \mathbf{u} \cdot \boldsymbol{\sigma} \cdot \hat{\mathbf{n}} dS \quad (3.3)$$

Betti's theorem may seems like an abstract mathematical formulation, but it has laid the foundation of theoretical seismology by relating the said rapture and observed seismic recording at a distance.

George Green, introduced the concept of “Green’s problem” or the problem of finding the response of a system to an excitation impulsive in both space and time. If the unit impulse is applied at $x = \boldsymbol{\xi}$ and $t = T$ and in n-direction, then we can denote the i-th component of displacement at general (\mathbf{x}, t) by $G = G_{in}(\mathbf{x}, t; \boldsymbol{\xi}, T)$. In our case, this amounts to solving after substituting $f_i = \delta_{im}\delta(\mathbf{x} - \boldsymbol{\xi})\delta(t - T)$ in index form of equation 3.2, and repeating the exercise for $m = 1, 2, 3$. It amounts to finding the responses of the medium to three ($m = 1, 2, 3$) different forces, all of same amplitude but directed in different reference axis. Combining these different expression resulting from f_i , we can obtain a compact tensorial equation in the “Green’s function” $\mathbf{G} = \mathbf{G}(\mathbf{x}, t; \boldsymbol{\xi}, T)$,

$$\rho \frac{\partial^2}{\partial t^2} \mathbf{G} - \delta(\mathbf{x} - \boldsymbol{\xi})\delta(t - T)\mathbf{I} - \nabla \cdot (\mathbf{c} : \nabla \mathbf{G}) = 0 \quad (3.4)$$

Once the Green’s function for a particular Earth model is known, we combine it with Betti’s theorem. In equation 3.3, replace $\mathbf{g}(\mathbf{x}, t)$ with the second order tensor $\delta(\mathbf{x} - \boldsymbol{\xi})\delta(t - T)$. Notice also that $\delta(\mathbf{x} - \boldsymbol{\xi})\delta(t - T)$ coincides with the forcing term in equation 3.4: it follows, by definition of Green’s problem, that $\mathbf{v}(\mathbf{x}, t) = \mathbf{G}(\mathbf{x}, t; \boldsymbol{\xi}, T_0)$ and $\boldsymbol{\sigma}(\mathbf{x}, t) = \mathbf{c} : \mathbf{G}(\mathbf{x}, t; \boldsymbol{\xi}, T_0)$. Solving mathematically, one can see that $\mathbf{u}(\mathbf{x}, t)$ can be calculated for any forcing term \mathbf{f} once the Green’s function of the medium has been found, and if $\mathbf{u}(\mathbf{x}, t)$ is known on S . When calculating the displacement field following an earthquake, S must equal the combination of the outer surface of the Earth with a surface \sum formed by the combination of two adjacent surfaces coinciding with the opposite faces of the earthquake fault. \mathbf{u} (not $\boldsymbol{\tau}$) will generally be discontinuous across \sum so it is necessary to treat \sum as a portion of S , i.e. of the boundary of the medium.

By further mathematical simplification we obtain,

$$u_n(\boldsymbol{\xi}, T + T_0) = \int_{-\infty}^{+\infty} dt \int_S u_i(\mathbf{x}, t) \hat{n}_j c_{ijkl} \frac{\partial}{\partial x_k} G_{ln}(\mathbf{x}, T - t; \boldsymbol{\xi}, T_0) dS \quad (3.5)$$

Σ

Equation 3.5 states that knowing the displacement on the fault (values of $\mathbf{u}(\mathbf{x}, t)$ to be integrated at the right-hand side) is enough to determine displacement everywhere.

3.2.1 Synthetic Seismogram

We can interchange $\boldsymbol{\xi}$ and \mathbf{x} and renaming of variable, and write this equation in a simplified form (after applying gauss divergence theorem):

$$u_n(\mathbf{x}, t) = \int_{-\infty}^{\infty} \int_S [u_i] n_j c_{ijkl} * \frac{\partial}{\partial x_k} G_{ln} dS(\boldsymbol{\xi}) dt \quad (3.6)$$

Using $m_{kl} = [u_i] n_j c_{ijkl}$ (moment density tensor) we finally get:

$$u_n(\mathbf{x}, t) = \int_{-\infty}^{\infty} \int_S m_{pq} * \frac{\partial}{\partial x_k} G_{ln} dt dS(\boldsymbol{\xi}) \quad (3.7)$$

Integrating moment density tensor within a volume we get moment tensor M_{kl} , finally leading us to:

$$u_n(\mathbf{x}, t) = M_{kl} * G_{ln,k} \quad (3.8)$$

We will now make a point source approximation and use only the first term of time dependent moment tensor. All terms of moment tensor will have same time dependence (source time response). After also including the instrument response, we get

$$u_n(\mathbf{x}, t) = M_{kl} \cdot [G_{ln,k} * s(t) * I(t)] \quad (3.9)$$

3.3 Numerical Modeling

Modelling with numerical methods involves the solution of wave equations to simulate wave propagation in different media. Numerical seismic modelling began as early as the 1950s (*Thomson (1950); Haskell (1953)*). Typically, numerical modelling algorithms are intended to solve sets of partial differential equations under certain boundary and initial conditions.

Numerical seismic modelling methods may be divided into three main categories:

1. **Direct methods** In the direct methods, also called full-wave equation meth-

ods, seismic waves propagate through a numerical mesh and are recorded at grid points. The reflectivity seismic modelling method, one of the oldest numerical modelling techniques invented in the 1950's (Thomson, 1950), falls into the category of the direct methods. The most commonly used direct methods are the finite difference (FD) method, finite element (FE) method, the pseudo-spectral (PS) method and the Spectral Element (SEM).

2. **Integral-equation method** The calculation of wavefields at different locations along a wavefront is based on Huygens' principle, in which the wavefield at a specific location is computed by superimposing the wavefields propagating from points along an earlier wavefront. Wavefields at points along a later wavefront can be built up in a similar way, so that wavefields propagating from points along the current wavefront will contribute to every point along the later wavefront. Two integral methods can be employed for the calculation: the domain integral-equation method and the boundary integral-equation method.
3. **Ray-tracing method** This method utilizes the eikonal and transport equations to calculate ray paths and amplitudes of seismic waves travelling through media. Since ray-tracing modelling is an asymptotic method (high-frequency estimation), it, in general, runs faster than full-wave equation (direct) methods and shows a high efficiency when modelling in 3D media. These are not as complete as direct methods and integral methods.

Out of these, the frequency domain reflectivity modelling method was chosen since it generates the most complete waveforms, and the attenuation effects for realistic 1D media can be easily generated. The reflectivity code was provided L Zhu (*Zhu and Rivera, 2002*).

The original algorithms for reflectivity modelling were proposed for solving elastic wave propagation problems in the solid earth with horizontal layers (*Thomson, 1950*). Those algorithms were originally used to calculate the responses of plane waves propagating in layered earth models. *Haskell* (1953) picked out some minor errors, and applied the corrected matrix formulas to modelling surface waves, such as Rayleigh, Love waves and Stoneley waves occurring at different interfaces. For this reason, this method is also known as the "Thomson-Haskell" method.

3.4 Basic working of reflectivity code

The green's function are generated by double numerical integration in frequency and wavenumber domain. For a general double couple 9 files are generated (grn.0 - grn8), and 3 extra (grn.a - grn.c) for including isotropic component.

Different green's files and their Herrmann equivalent		
grn.a	ZEP	Z-component of displacement due to explosive source
grn.b	REP	R-component of displacement due to explosive source
grn.c	TEP	T-component of displacement due to explosive source (empty)
grn.0	ZDD	Z-component of displacement of a 45 dip-slip type source
grn.1	RDD	Radial component of displacement of a 45 dip-slip source
grn.2	TDD	Transverse component of displacement of a 45 dip-slip source(empty)
grn.3	ZDS	Z-component of displacement of a dip-slip type source
grn.4	RDS	Radial component of displacement of a dip-slip source
grn.5	TDS	Transverse component of displacement of a dip-slip source
grn.6	ZSS	Z-component of displacement of a strike-slip type source
grn.7	RSS	Radial component of displacement of a strike-slip source
grn.8	TSS	Transverse component of displacement of a strike-slip source

1. If there is only one input moment argument, then it is considered to be a explosive source. It needs to be given in seismic moment M_0 , ex: -M1.26e23, and unit should be in dyne-cm. It requires that *.grn.[a-c] must be present. The code itself multiplies M_0 with a factor of 10^{-20} .
2. If there are three input arguments, then it is considered to be single-force. These three arguments are magnitude in dyne, strike and slip of force. The code will look for *.grn.[0-5]. In this case the force is multiplied with a factor of 10^{-15} .
3. If four input arguments are given, then it is considered to be a double couple source. All the green's function files *.grn.[0-8] must be present. The input should be in following order; moment magnitude in M_w , strike, dip and rake of fault. ex: -M4.8/31/84/73. The moment magnitude is converted into seismic moment using the relation: $M_w = \frac{1}{15} \log M_0 - \frac{16.1}{15}$. Once computed it is then multiplied by the factor of 10^{-20} .
4. If there are seven input arguments then it is considered to be a general case and general synthetic seismogram is computed. The seven input arguments are; seismic_moment/Mxx/Mxy/Mxz/Myy/Myz/Mzz. All the grn's function files *.grn.[a-c,0-8] must be present. Seismic moment in this case also is multiplied by the factor 10^{-20} .

Calculating synthetic seismogram from green's function

$$\mathbf{u}_z(r, z = 0, \omega) = ZSS A_1 + ZDS A_2 + ZDD A_3 \quad (3.10)$$

$$\mathbf{u}_r(r, z = 0, \omega) = RSS A_1 + RDS A_2 + RDD A_3 \quad (3.11)$$

$$\mathbf{u}_\phi(r, z = 0, \omega) = RSS A_1 + TDS A_2 \quad (3.12)$$

$$\begin{aligned} \mathbf{u}_z(r, \phi, 0, \omega) = & ZSS [(f_1 n_1 - f_2 n_2) \cos 2\phi + (f_1 n_1 - f_2 n_2) \sin 2\phi] \\ & + ZDS[(f_1 n_3 + f_3 n_1) \cos \phi + (f_2 n_3 + f_3 n_2) \sin \phi] + ZDD[f_3 n_3] \end{aligned}$$

$$\begin{aligned} \mathbf{u}_r(r, \phi, 0, \omega) = & RSS [(f_1 n_1 - f_2 n_2) \cos 2\phi + (f_1 n_1 - f_2 n_2) \sin 2\phi] \\ & + RDS[(f_1 n_3 + f_3 n_1) \cos \phi + (f_2 n_3 + f_3 n_2) \sin \phi] + RDD[f_3 n_3] \end{aligned}$$

$$\begin{aligned} \mathbf{u}_\phi(r, \phi, 0, \omega) = & TSS [(f_1 n_1 - f_2 n_2) \cos 2\phi + (f_1 n_1 - f_2 n_2) \sin 2\phi] \\ & + TDS[(f_1 n_3 + f_3 n_1) \cos \phi + (f_2 n_3 + f_3 n_2) \sin \phi] \end{aligned}$$

(Wang and Herrmann, 1980) (Jost and Herrmann, 1989)

Green's function SAC headers

NPTS	2409	number of data points
B	-9.992996e+00	begin time
E	1.408700e+01	end time
IFTYPE	TIME SERIES FILE	file type
LEVEN	TRUE	evenly sampled time series
DELTA	1.000000e-02	time increment
DEPMIN	-2.073471e+04	minimum amplitude
DEPMAX	1.584818e+04	maximum amplitude
DEPMEN	5.137106e+01	mean amplitude
OMARKER	0	event origin marker
T1MARKER	1.848	first arrival (P) marker
T2MARKER	3.192	t0 (S) marker
IZTYPE	GMT DAY	type of reference time
CMPAZ	0.000000e+00	component azimuth relative to north
CMPINC	0.000000e+00	component inclination relative to the vertical
DIST	4.994444e+00	source receiver distance in km
LOVROK	TRUE	TRUE if it is okay to overwrite this file on disk
NVHDR	6	Header version number. (6)
LPSPOL	FALSE	TRUE if station components have a positive polarity
LCALDA	TRUE	TRUE if DIST, AZ, BAZ, and GCARC are to be calculated from station and event coordinates

3.5 Preparing Synthetics

3.5.1 Model Used

SCAK:

thickness	V_s	V_p	density	Q_p	Q_s
4.0000	3.0100	5.3000	2.5200	300.0000	600.0000
5.0000	3.1800	5.6000	2.6100	300.0000	600.0000
5.0000	3.5200	6.2000	2.7800	300.0000	600.0000
5.0000	3.9200	6.9000	2.9700	300.0000	600.0000
5.0000	4.2000	7.4000	3.1200	300.0000	600.0000
9.0000	4.3700	7.7000	3.2000	300.0000	600.0000
16.0000	4.4900	7.9000	3.2600	300.0000	600.0000
17.0000	4.6000	8.1000	3.3200	300.0000	600.0000
0	4.7200	8.3000	3.3700	300.0000	600.0000

3.5.2 Azimuthal check

These following azimuthal check have been performed using the SCAK model for Alaska. A vertical strike slip fault have been taken for test, with strike along the North. The source depth have been taken to be 8 kms. The variation of synthetics has been shown at two epicentral distances of 20 km and 100 km. For test 5.4 Mw earthquake with source duration of .82 sec has been taken. Azimuthal change can be very small and should be plotted for atleast 180° . If it is an explosive source, that would cause independence on azimuth. For vertical strike-slip case we can see that it remains almost of similar kind (amplitude changes) for first 90° but then it suddenly shifts by $\frac{\pi}{2}$ phase shift. This is because moving from compressional zone to tension zone.

3.5.3 Depth check

Vertical Strike-Slip Fault First, at epicentral distance of 150 km and azimuth of 30° we computed synthetics for 5 different source depths : 8, 20, 50, 90, 150 kms.

For shallow sources (8 and 20km) the surface waves can be noted (Rayleigh in radial and vertical component; whereas love in transverse component)

3.5.4 Epicentral distance check

Keeping the depth of source constant at 20 km, and azimuth at 30° , epicentral distance was varied from 10 km to 200 kms. Some, of them have been shown here.

3.5.5 Compatibility of double couple and fault

An arbitrary fault of strike=20, dip=30, rake=40 were taken for test. Moment tensor for such an arbitrary fault was calculated: (Aki and Richard's format):

$$M = \begin{bmatrix} -0.3113 & 0.4723 & -0.7333 \\ 0.4723 & -0.2454 & 0.0751 \\ -0.7333 & 0.0751 & 0.5567 \end{bmatrix} \quad (3.13)$$

It is an example of pure double couple source ($\gamma = 0$). M_0 was taken to be 10^{27} dynes-cm and its corresponding M_w was calculated to be 7.266. In the figure it has been shown that both forms of input gives same synthetics.

When tested for an event (id-278678), which had the highest CLVD component. The result showed that synthetics of double-couple were similar to that of fault parameter (both normal and auxiliary), but the full moment tensor differed mostly in magnitude from the rest. This particular event had :

```

Mw      : 4.40
M0      : 5.05e22
M       : -.73/.21/-14/-36/-07/1.09
Plane1  : 60.8/42.2/82.2
Plane2  : 251.3/48.3/97
MDC     : -.829/.3721/-1334/-1570/-0406/.9860
Depth   : 100km
epi dis: 50km

```

3.5.6 Testing different models

For this we need different observed seismograms, so that we can compare synthetics obtained by different models. Seven different models were tested using 18 events which were recorded at 34 different stations.

Homogeneous SOCAL The whole half homogeneous have properties of lower crust (above moho) of Southern California.

Prefect test for looking at directivity pattern, seeing Rayleigh waves (no Love waves) . The source was assumed to be a vertical strike-slip fault. It was tested for different depths (8km and 80km) at different epicentral distances (20 and 150). We looked at different azimuthal points (0, 45, 90, 135, 180).

Source Depth: 80Km				Source Depth: 8Km			
Azimuth	r	t	z	Azimuth	r	t	z
0		SH		0		SH	
45	P, SV		P, SV	45	P, Rayleigh		P, Rayleigh
90		SH		90		SH	
135	P, SV		P, SV	135	P, Rayleigh		P, Rayleigh
180		SH		180		SH	

Conclusions

1. Transverse component is only composed of SH.
2. Surface waves generated only by shallow source.
3. Even for shallow source surface waves are visible only at large epicentral distances.
At near source (20km) the seismogram is dominated by short period S waves.
4. Shear component of waves is maximum along the strike plane and the auxiliary plane. (max. SH is more than max. SV because of energy distribution between SV and P)
5. At epicentral distance of 150 shallow events generate Rayleigh waves (r and z component), whereas, deep events do not do so. It is the SV that is present.
6. Polarity reversal when moved from tension to pressure axis. (azimuthal variation).
7. No love waves (which are in t-component for layered case).

Single crustal layer SOCAL

For single layer case (Layer1 and Layer3 of SOCAL as half space) were tested. Synthetic seismograms were generated at epicentral dist of 150 Km by 8 km deep source. We could see all the seismic waves clearly in this case (including the love waves). Directivity can also be tested.

Azimuthal test

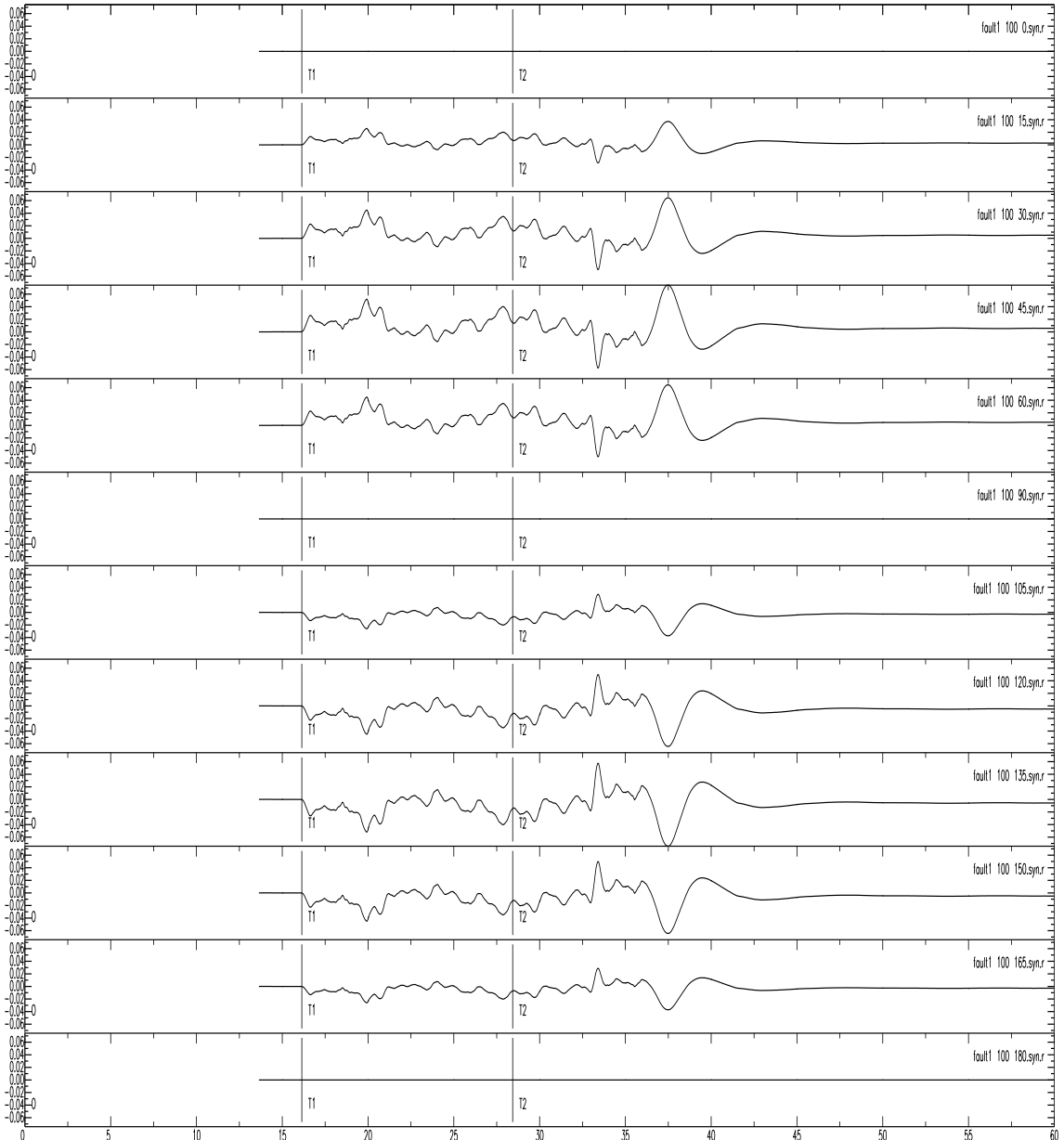


Figure 3.1: Azimuthal variation from 0 - 180 at increment of 15° for stations at 100km epicentral distance. Vertical strike-slip fault (Strike = 0, dip = 90, slip = 0). It is understood that waveforms for azimuth 180-270 will be same as that for 0-90, and opposite in other quadrants.

Source depth check

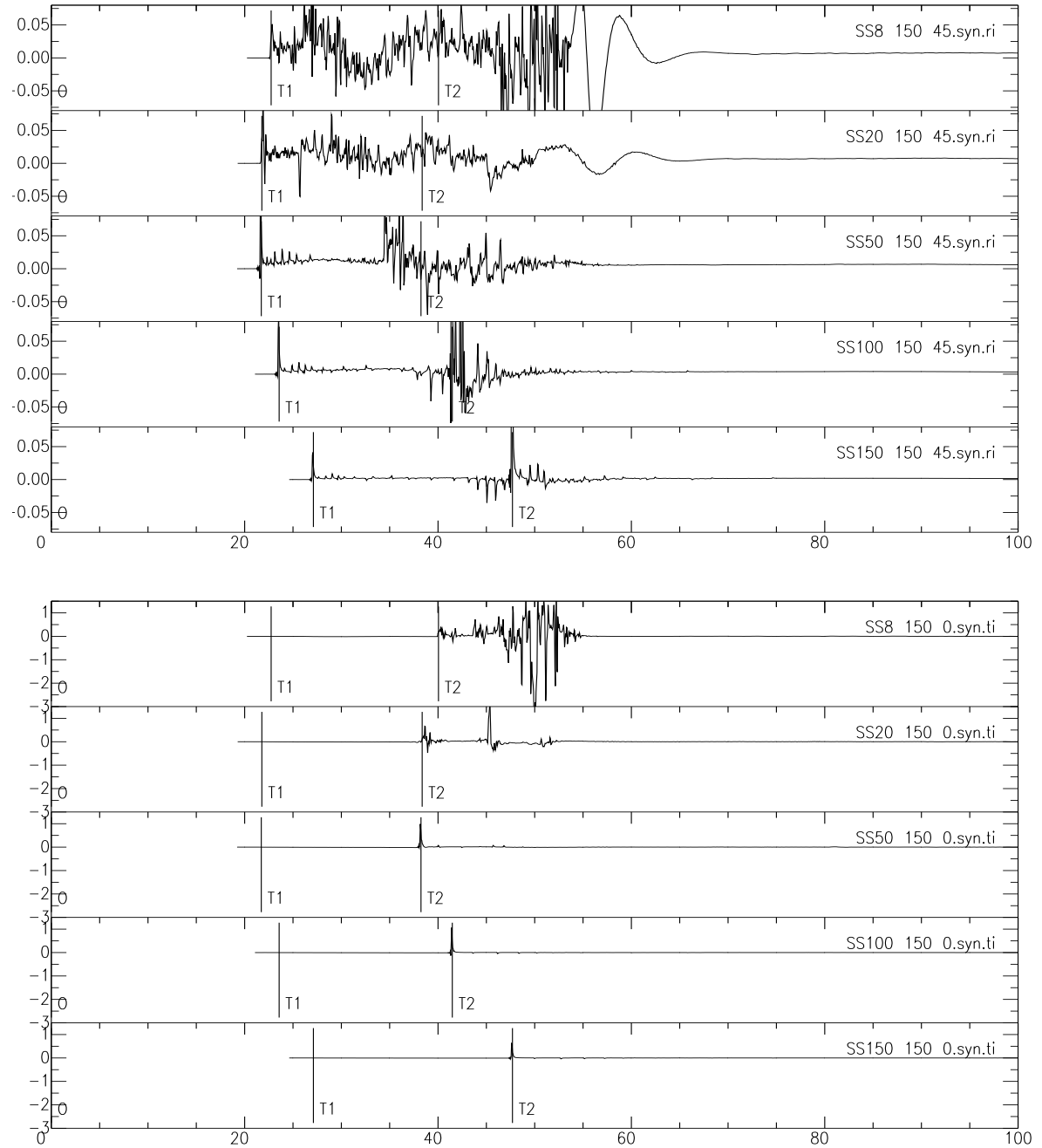


Figure 3.2: Source depth check: Radial and transeverse Component of velocity for Vertical strike-slip fault. Azimuth: 45° for radial and 0° for transeverse; Epicentral distance: 150km; Source depth: 8, 20, 50, 90, 150, 200 km.

Epicentral distance check

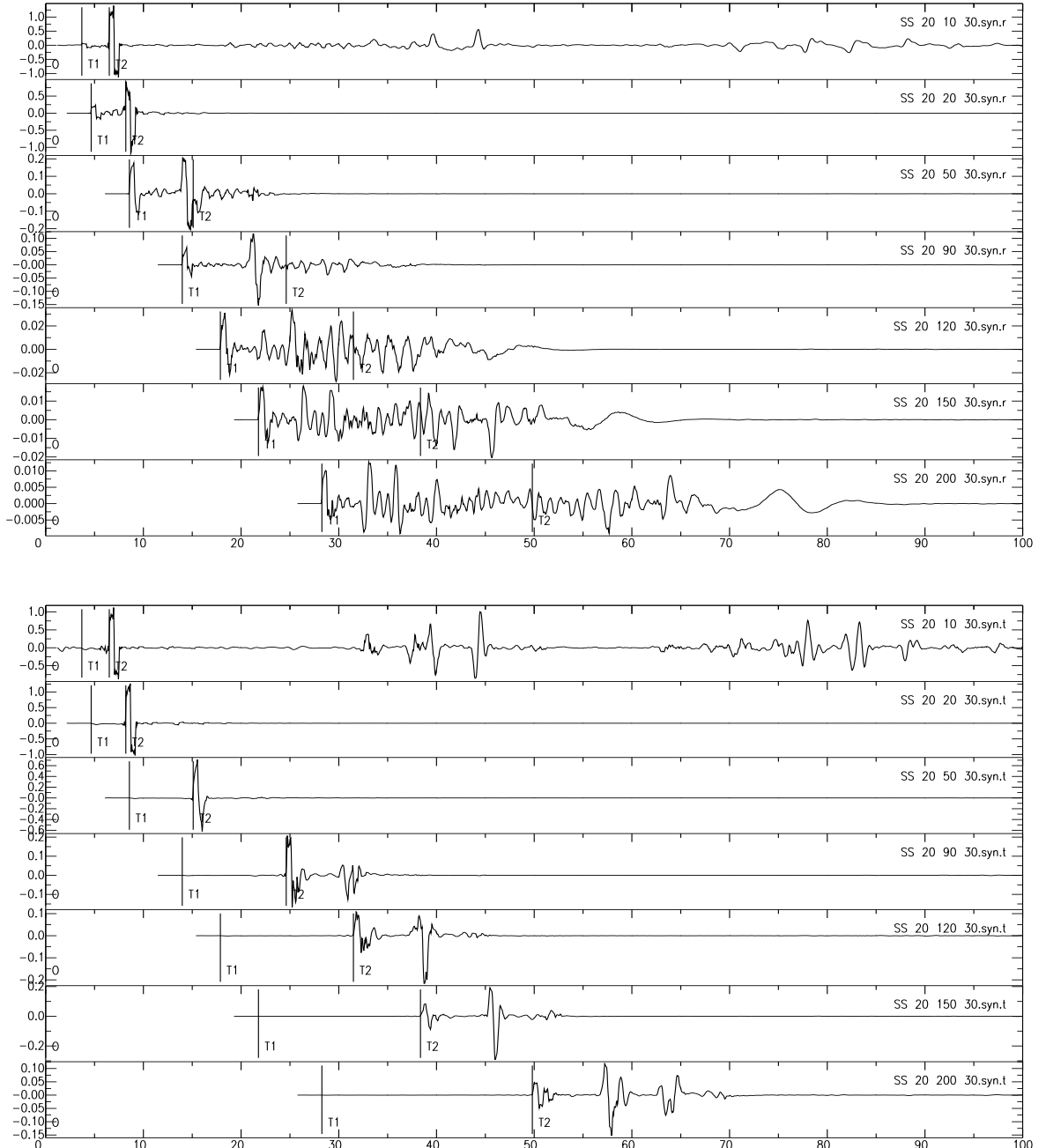


Figure 3.3: Epicentral distance check: Radial and Transeverse Component of velocity for Vertical Strike-slip fault. Azimuth: 30° ; Epicentral distance: 10, 20, 50, 90, 120, 150, 200km; Source depth: 20 km.

Homogeneous SOCAL

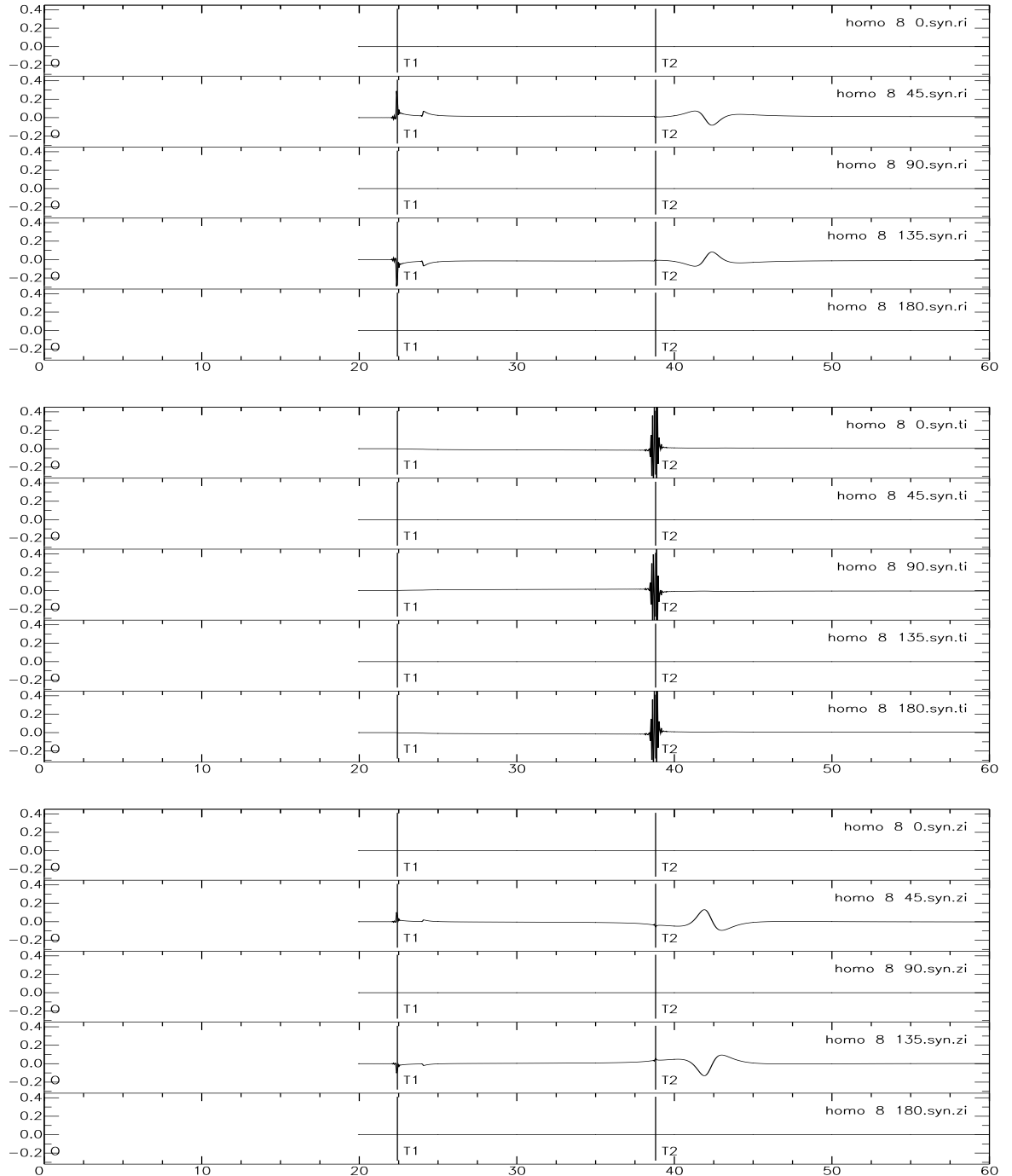


Figure 3.4: Homogeneous SOCAL model: Shows directivity for r, t and z component for a Strike-slip fault. Depth: 8km; epicentral dist: 150 km; Azimuth: 0, 45, 90, 135, 180

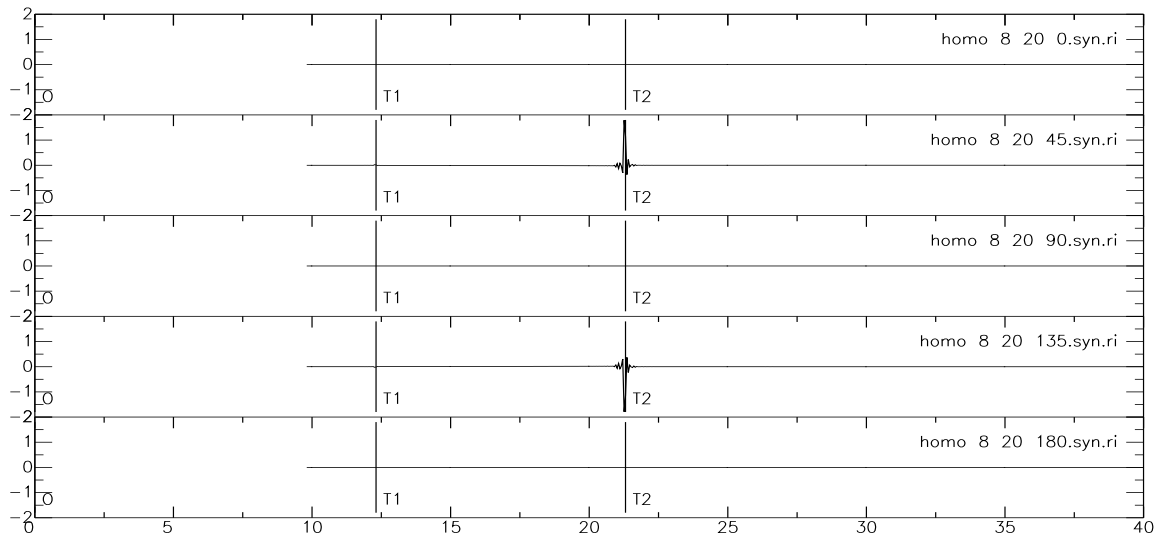


Figure 3.5: Radiation directivity: Shows directivity for r component, Strike-slip fault. But surface waves can't be seen; dominance of short-period S waves at small epicentral distance. depth: 8km; epicentral dist: 20 km; Azimuth: 0, 45, 90, 135, 180

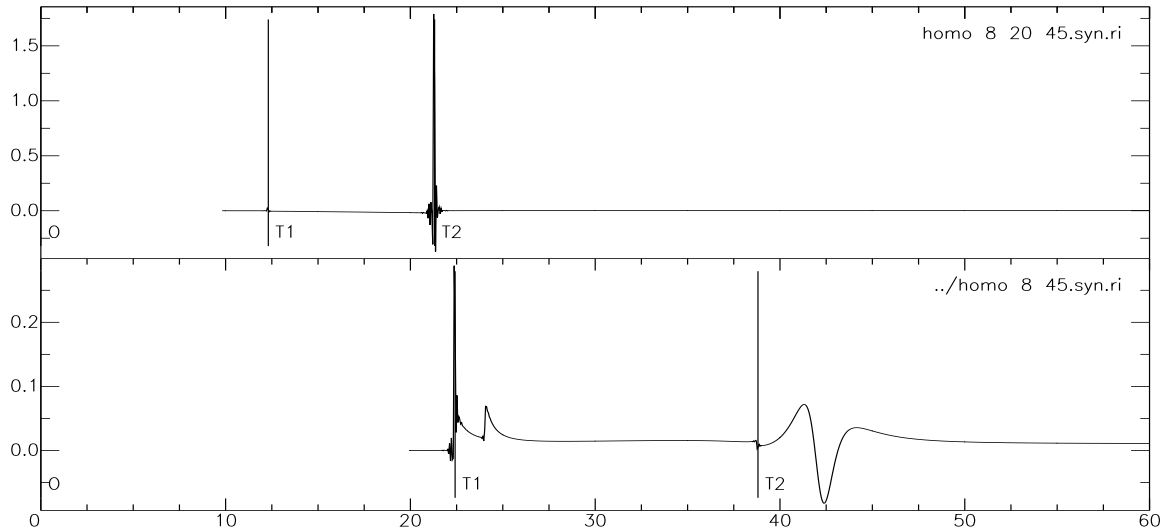


Figure 3.6: Energy dominance of different phases: Shows surface dominance at large distance and short-period S wave dominance at small epi dist. Source depth: 8Km; epi dist: 20, 150; azimuth: 45

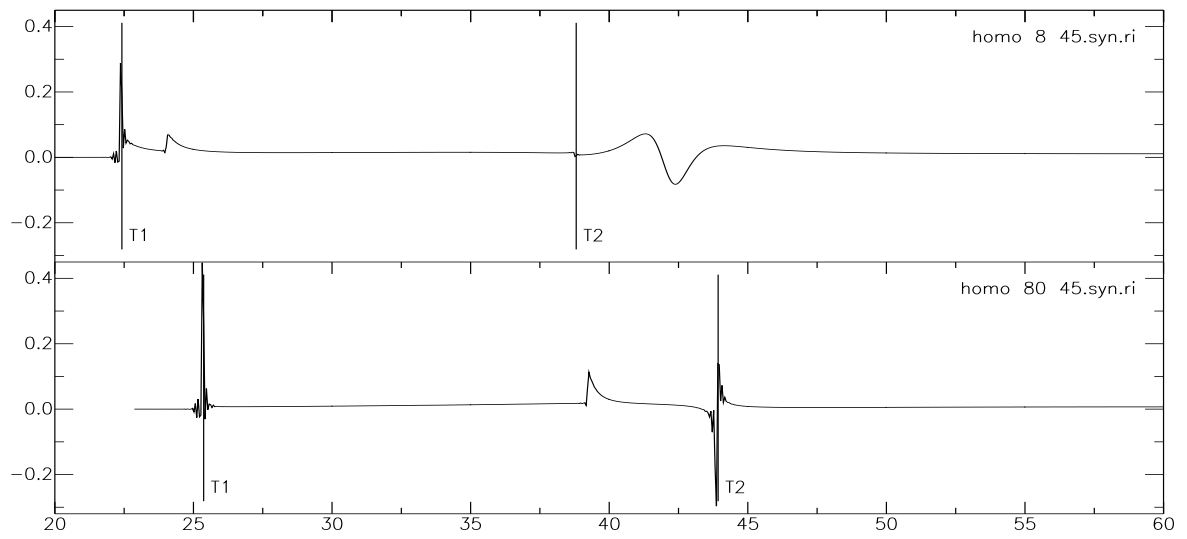


Figure 3.7: Depth test: Surface waves not generated by deep events; Vertical strike slip fault Different depths: 8, 80km; epicentral distance: 150km; Azimuth: 45

Single crustal layer: SOCAL

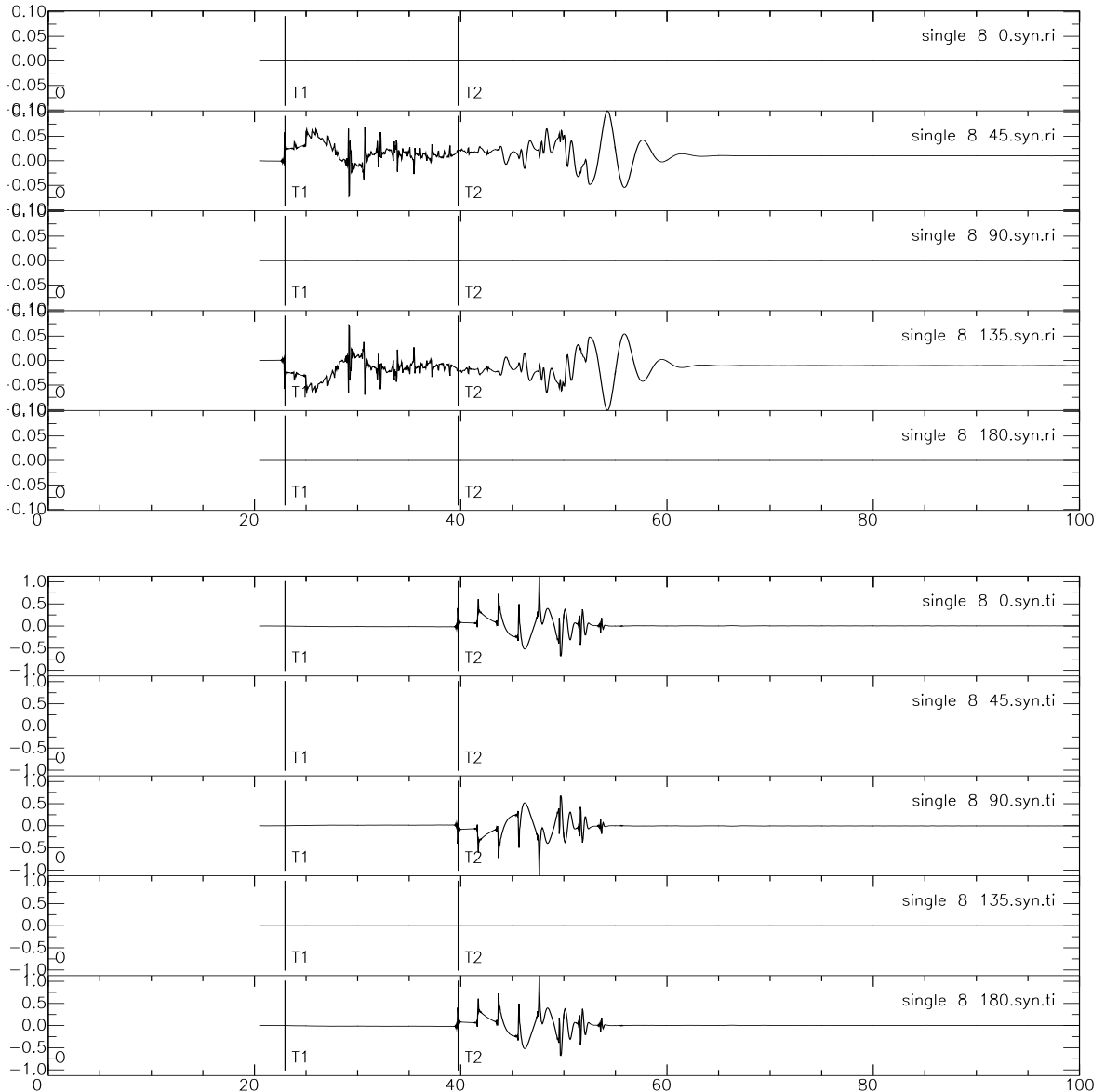


Figure 3.8: Single crustal layer SOCAL: Love waves generated in this single layer case (in transverse component). We can also see the Rayleigh waves. The arrivals between P and S are combinedly called PnL. epicentral distance: 150km. Source depth: 8km. Here we can also check the directivity of seismic arrivals. Azimuth: 0, 45, 90, 135, 180

3.6 Synthetics for various Alaska models

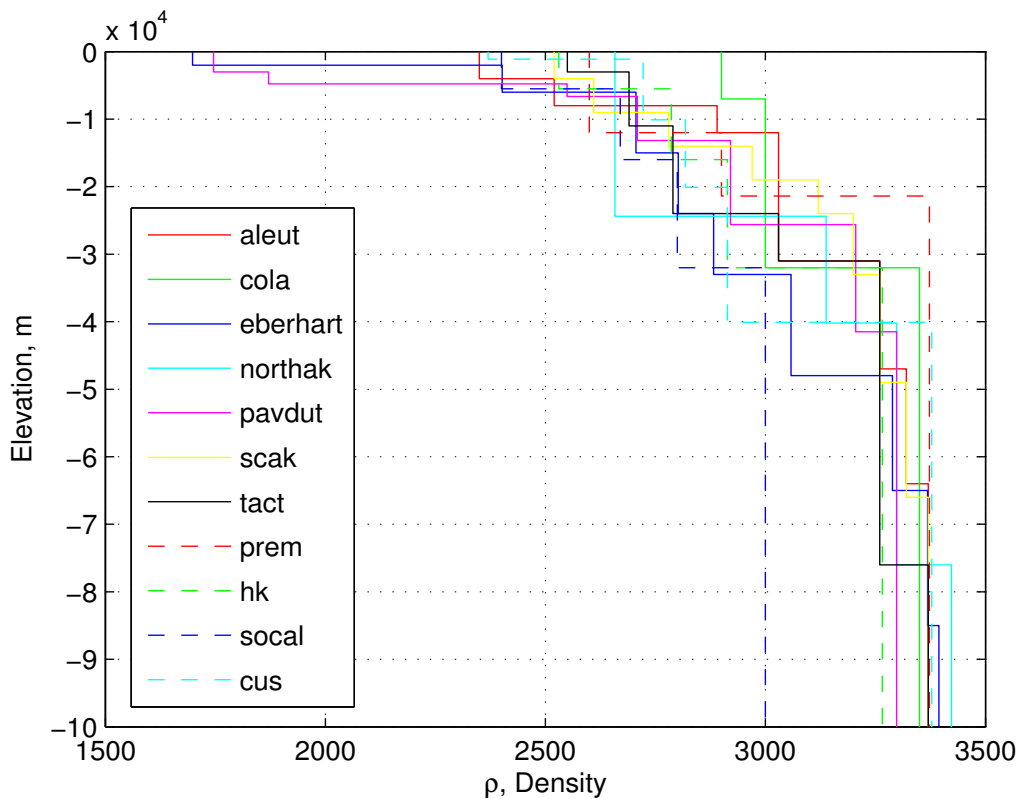


Figure 3.9: Density variation with depth for different models models.

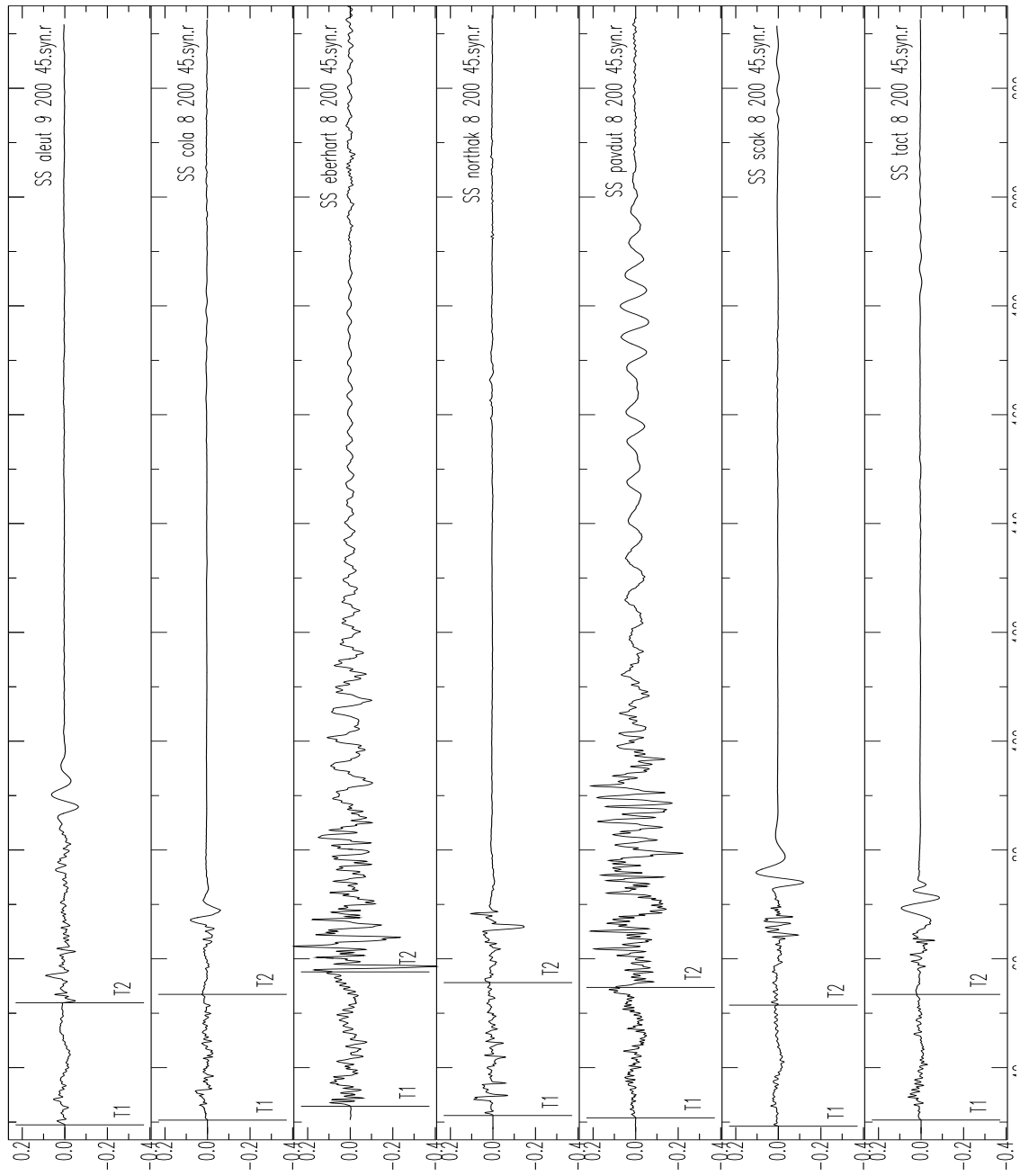


Figure 3.10: Radial component at a particular station using different Alaska Models. Depth : 8km, epicentral distance : 200Km, Azimuth: 0 for Transverse and 45 fro radial. Eberhart and Pavdut have shallow low velocity layers.

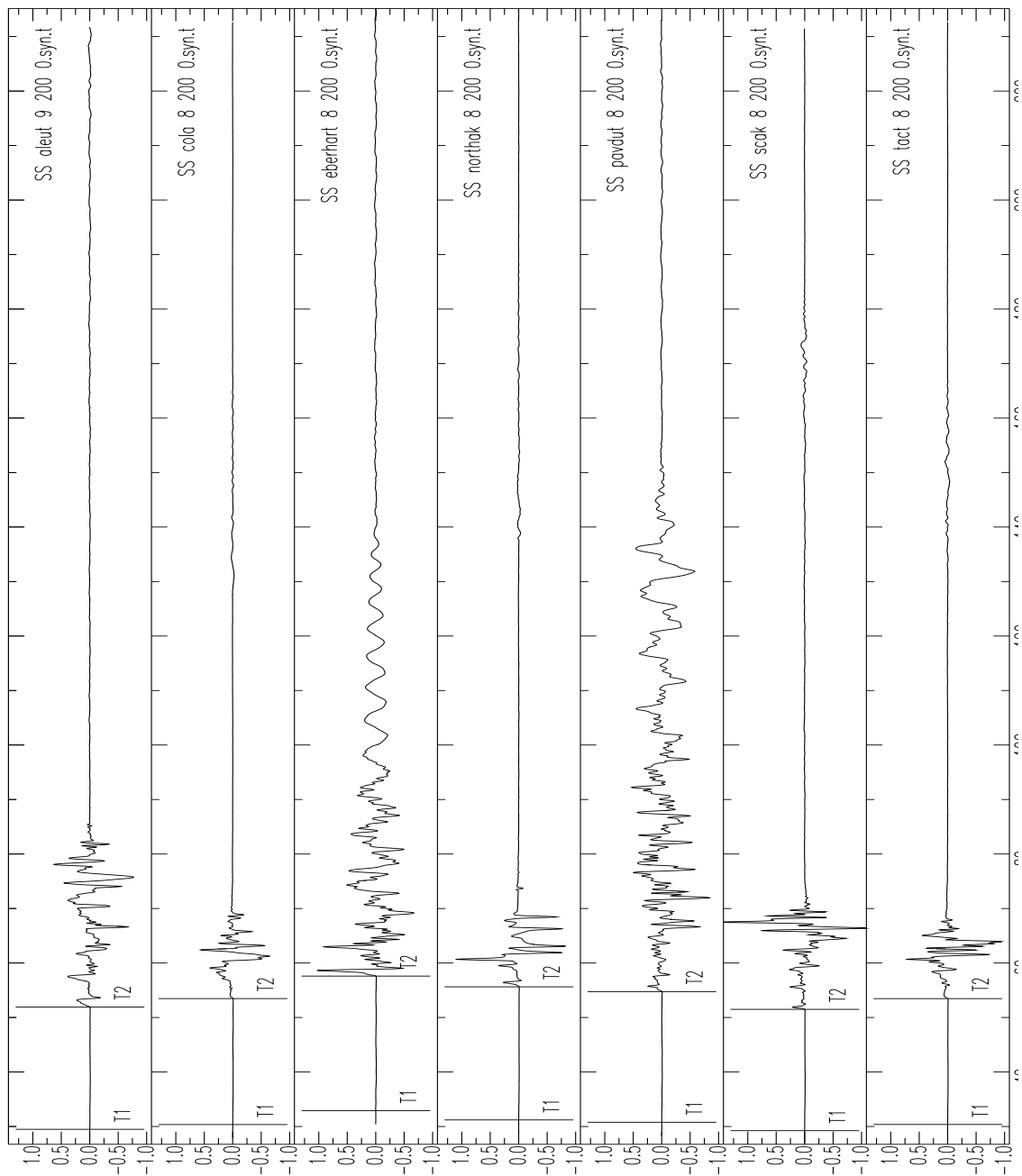


Figure 3.11: Transverse component at a particular station using different Alaska Models. Depth : 8km, epicentral distance : 200Km, Azimuth: 0 for Transverse and 45 fro radial. Eberhart and Pavdut have shallow low velocity layers.

3.7 Comparision between 1D synthetics from SPECFEM3D and FK

The synthetic seismograms were made using Numerical Integration approach (SPECFEM) and compared with those made from Discrete wavenumber summation (FK-synthetics). Numerical Integration takes a much longer time to compute the synthetics and is considered to difficult in implementing in real time. In our case we had considered a one dimensional velocity model and hence the difference due to Numerical integration approach and discrete wavenumber wont be much but in later case we could save huge amount of computation.

The synthetics from fk-synthetics were obtained at different angles and then rotated to NEZ using SAC. Synthetics from SPECFEM were also decimated so that we have same sample interval in both of them. Now both the synthetics were filtered by applying fourth-order butterworth bandpass filter using corner frequencies 0.02 and .2 Hz. The results match to a great extent in P-wave window (approx. 25sec). Later to that there were some dissimilarities. The reason being applying different filters for P-wave and surface waves. Surface waves need to be filtered at corner frequencies of 0.02 and 0.1 Hz. By this both the methods would lead to similar results.

It needs to be kept in mind that FK-*syn* outputs displacement in cm, whereas SPECFEM does in m. So, there will be difference in results by order of 2.

Observations

1. Spurious later arrivals in case of *syn* (Wavenumber Frequency). This doesn't seem to be implicitly generated during double fourier summation as they are not at same time for different epicentral distances.
2. In case of 45 azimuth, we see spurious arrivals in case of SPECFEM. This is because of failure of absorbing boundary condition when the rays are incident to boundary at an angle.

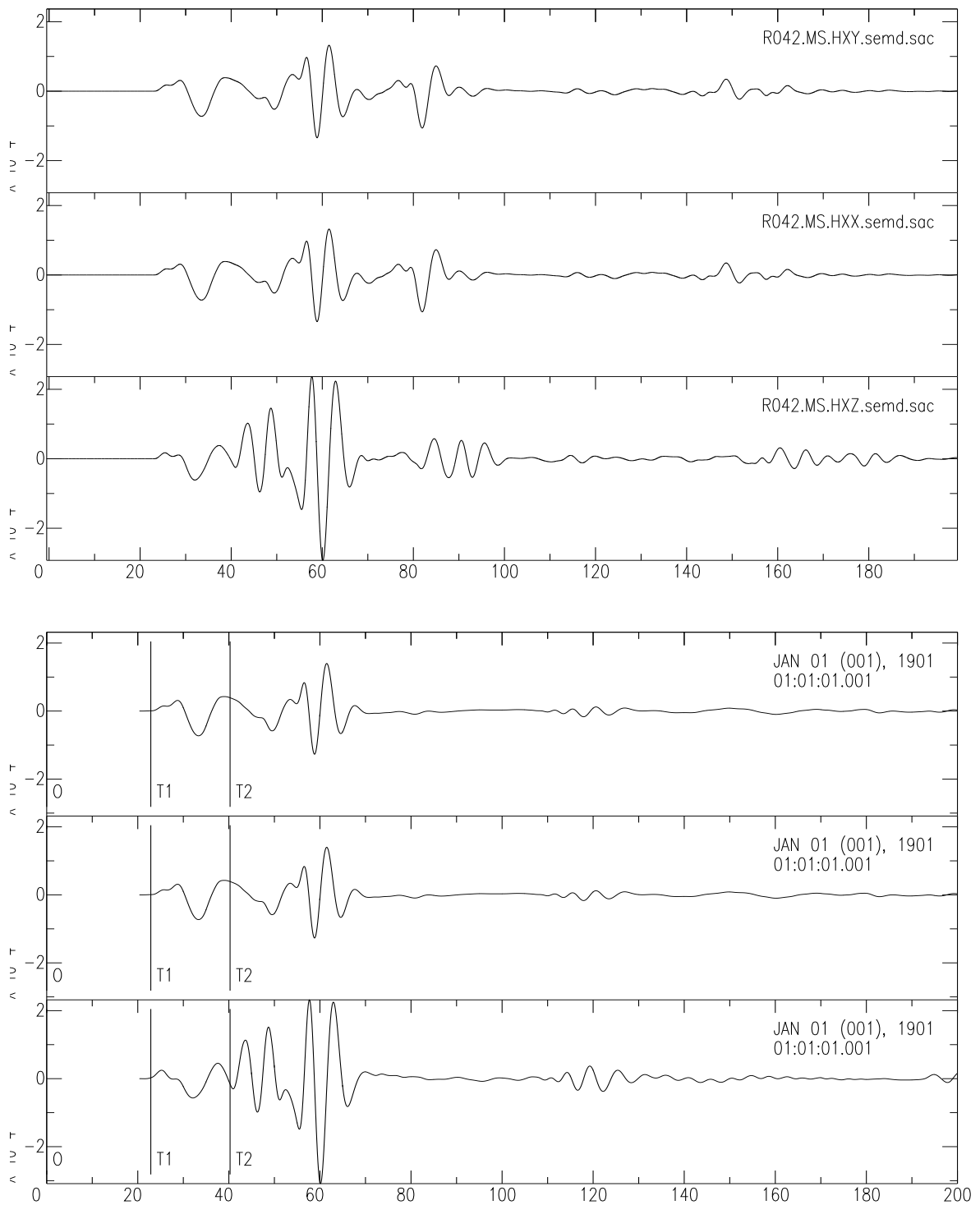


Figure 3.12: Comparison between synthetics from SPECFEM3D and FK (for shallow depth source). Compared for a vertical strike-slip fault. Mw: 4, epi dist: 150km, source depth: 7km, Azimuth: 45. Matches well till 55 sec after first arrival. Filter: fourth-order butterworth bandpass filter using corner frequencies 0.02 and 0.2 Hz.

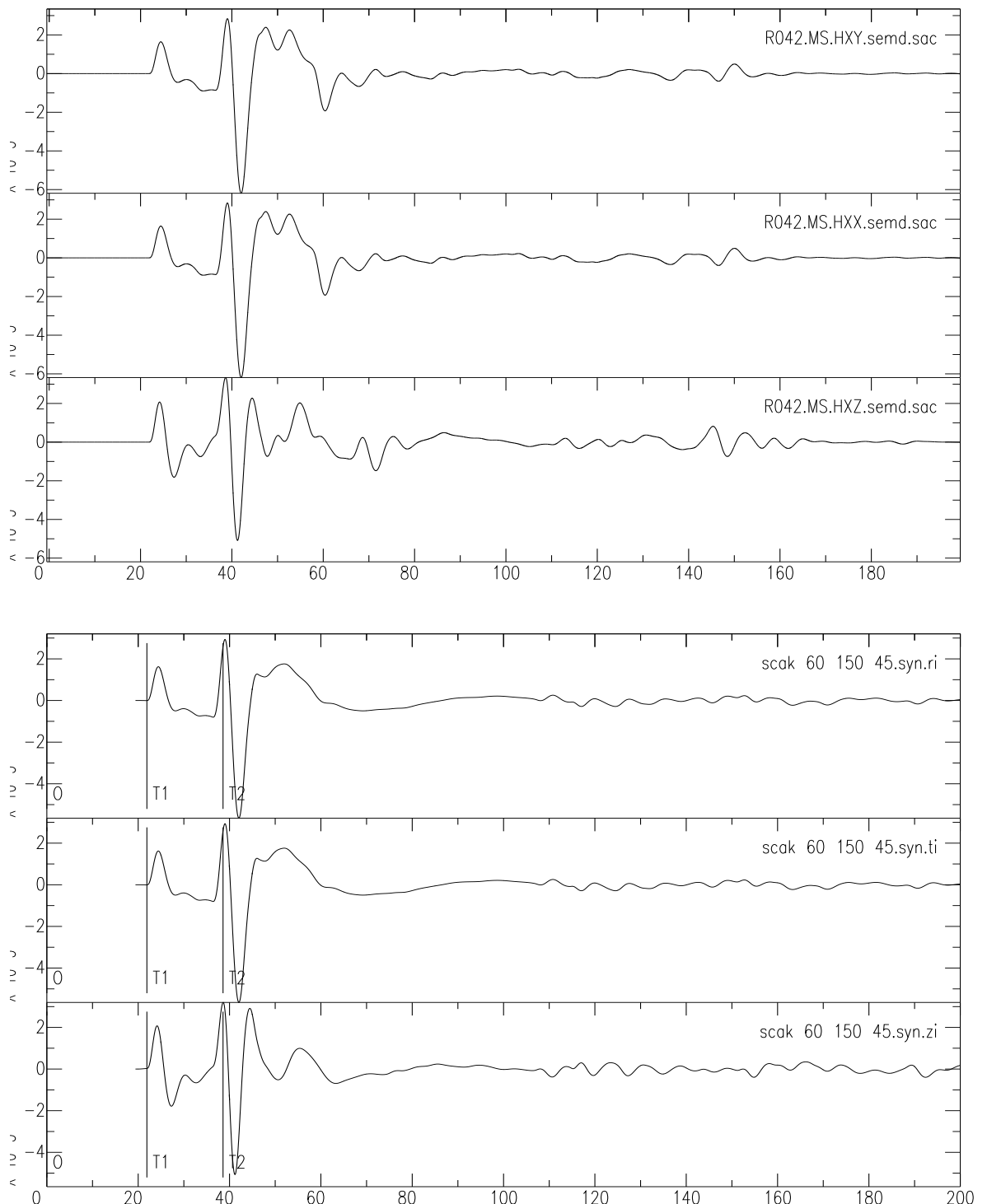


Figure 3.13: Comparison between synthetics from SPECFEM3D and FK (for deep depth source). Compared for a vertical strike-slip fault. Mw: 4, epi dist: 150km, source depth: 60km, Azimuth: 45. Filter: fourth-order butterworth bandpass filter using corner frequencies 0.02 and 0.2 Hz.

Chapter 4

Moment Tensor Inversion using “Cut-and-Paste” approach

4.1 Basic Idea

Due to our inability to map the extreme heterogeneity of earth, there will always be inherent errors in any earth model that we assume. Using these erroneous earth model we will never be able to achieve accurate green’s function and hence the synthetics. We can compensate for the error in green’s functions by allowing differential time shifts between the principal crustal arrivals (*Zhao and Helmberger (1994)*). Two kinds of waveforms are used for source estimation: body waves and surface waves. Generally, the body waves are less affected by shallow heterogeneities and are more stable than surface waves (*Zhu and Helmberger (1996)*). Inversion is usually more stable at longer period. While carrying out inversion at long period using full waveforms, it is the surface wave which dominates. Long period inversion provide us with more stability. The higher frequency surface waves (5-10 sec) are more stronger than 50-sec waves but are more difficult to invert due to instability cause by lateral variation. Also, even the small amount of time shift at such a high frequency would cause spurious results.

CAP inversion utilizes both, the body waves (Pnl) and the surface waves for the estimation of the focal mechanism. During inversion, the seismogram is broken into 5 parts (Body- P V, P R; and Surface- Surf V, Surf R and Surf Z) and are tried to fit independently by allowing a certain tshift between the synthetics and the data. The focal mechanism is obtained by applying a grid search algorithm over complete strike, dip and rake range. The depth estimation is done by cycling through green’s function obtained from different source depth, and using them to find the minimum misfit solution.

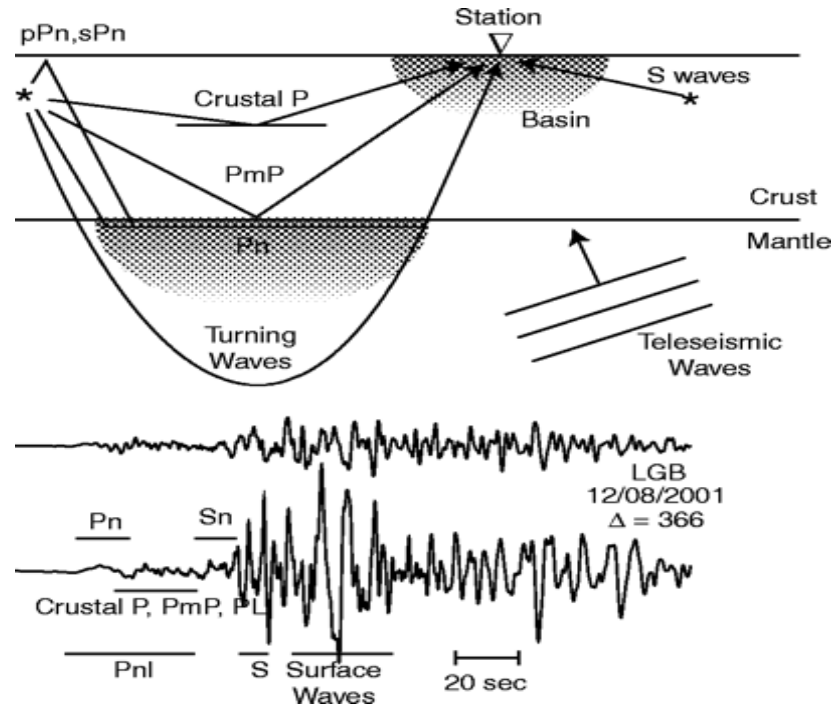


Figure 4.1: Pnl phase includes all the P-crustal phases, predominantly, direct P (crustal or Pg), PmP(P reflected by moho) and Pn (head waves grazing though upper mantel). (*Savage and Helmberger, 2004*)

Pnl

Pnl phase includes all the P-crustal phases, predominantly, direct P (crustal or Pg), PmP(P reflected by moho) and Pn (head waves grazing though upper mantel).

4.2 Test events

21 significant earthquakes that I have planned to test for CAP Moment tensor inversion

A	B	otime	lon	lat	MT_dep	AEIC_dep	Mw	eid	AEIC_id
1	4	2007-10-10 (2007283)	18:03:26	-147.41	59.96	15.00 (11.80)	4.05	280436	(280253)
2	2	2007-09-19 (2007262)	11:22:26	-146.11	61.38	35.00 (30.82)	4.45	279084	(278884)
3	15	2009-04-07 (2009097)	20:12:55	-149.74	61.45	45.00 (33.03)	4.59	319798	(319605)
4	12	2009-02-15 (2009046)	19:35:00	-146.33	61.60	35.00 (37.24)	4.49	316444	(316248)
5	8	2008-08-28 (2008241)	23:14:18	-149.60	62.12	50.00 (42.95)	4.11	305302	(305104)
6	21	2009-07-30 (2009211)	22:39:10	-151.09	59.93	30.00 (44.08)	4.38	326766	(326568)
7	3	2007-10-03 (2007276)	14:06:12	-151.29	58.28	40.00 (45.46)	5.17	279857	(279709)
8	17	2009-04-30 (2009120)	04:54:57	-151.31	58.99	40.00 (52.73)	4.88	321298	(321087)
9	20	2009-06-26 (2009177)	16:48:20	-150.64	61.91	60.00 (59.48)	4.25	324973	(324781)
10	19	2009-06-22 (2009173)	19:28:05	-150.70	61.94	80.00 (64.59)	5.51	324684	(324487)
11	7	2008-03-27 (2008087)	23:07:45	-152.17	59.01	75.00 (68.53)	5.26	290389	(290230)
12	5	2007-11-28 (2007332)	23:57:03	-151.13	61.91	75.00 (69.61)	4.82	283325	(283131)
13	13	2009-02-23 (2009054)	00:04:27	-153.63	58.92	85.00 (87.75)	4.86	316902	(316685)
14	10	2008-12-28 (2008363)	07:13:10	-151.05	62.35	80.00 (89.31)	4.42	313450	(313240)
15	14	2009-03-17 (2009076)	01:13:33	-152.15	60.24	90.00 (90.14)	4.22	318329	(318113)
16	9	2008-09-18 (2008262)	19:43:53	-152.79	59.50	85.00 (90.15)	4.53	306659	(306480)
17	11	2009-01-24 (2009024)	18:09:50	-152.89	59.43	95.00 (97.87)	5.72	314984	(314787)
18	1	2007-09-11 (2007254)	23:46:34	-151.53	61.53	100.00 (100.88)	4.40	278678	(278485)
19	16	2009-04-14 (2009104)	17:14:27	-153.06	60.16	105.00 (117.78)	4.27	320317	(320117)
20	18	2009-05-24 (2009144)	09:40:04	-153.25	59.78	125.00 (125.48)	4.60	322995	(322785)
21	6	2008-03-14 (2008074)	09:38:21	-152.64	61.07	165.00 (143.65)	4.97	289517	(289317)

A- Sorted by Depth (Mw)

B- Sorted by occurrence (otime)

4.2.1 Depth Estimate

The hypocentral depth is one of the crucial parameters to be estimated. Primarily, it is estimated by pP - P arrival time difference and have been used in the AEIC catalog. On the other hand, it can also be estimated by cycling moment tensor inversion for different depth source and finding the minimum misfit solution. Both of these methods, quite often lead to slightly different results. This is reason why AEIC catalog depth differs from AEIC_MT result.

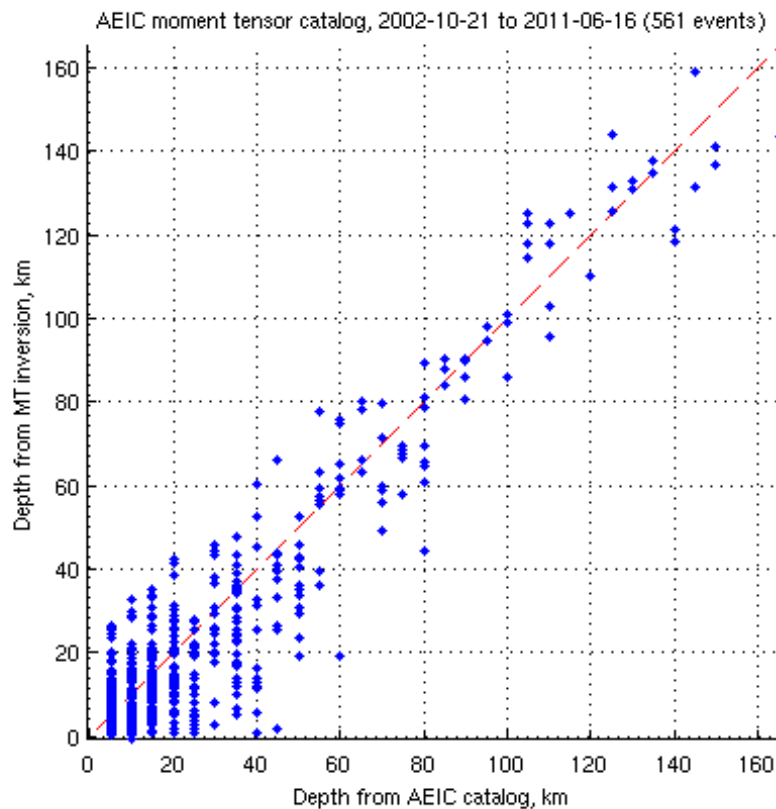


Figure 4.2: Relation between depth in AEIC catalog and those estimated by AEIC using Moment Tensor inversion

4.3 AEIC Moment Tensor Inversion

I have also compared AEIC Moment Tensor solution (AEIC_MT) with CAP Moment tensor solution. Both these methods differ not just in their basic technique but also in their input and output parameters.

AEIC Moment tensor	CAP Moment tensor
Decomposes waveform into 3 part (RTZ)	Decomposes waveform into 5 part (PV, PR, SurfV, Surf R, SH)
Frequency filter is usually set to allow long period waveform. At such long period, mostly surface waves dominate	Differential filter for Pnl wave part allowed us to increase their weight
Least-square inversion	Grid-search inversion
Isotropic part included	Only double-couple

4.4 EXAMPLE EVENT (eid 319605)

otime	lon	lat	MT_dep	AEIC_dep	Mw	AEIC_id
2009-04-07 (2009097) 20:12:55	-149.74	61.45	45.00	(33.03)	4.59	319605

The moment tensor solution had already been estimated by the Alaska Earthquake Information Center (AEIC). It was estimated by only matching the surface waves of recorded data at the AEIC stations with synthetic ones. CAP on the other hand also matches the long period body waves Pnl, in addition to the surface waves. Cut and Paste approach also allows for time shift between data and synthetics in order to compensate for error in the complex green's function.

The reason we chose this event at the initial stage of testing was it being a medium order magnitude event ($M_w = 4.6$, as reported by AEIC) and also being a shallow event (depth = 45km). Surface wave fits can be easily done and tested for magnitude > 3.5 , whereas below this, other approach is required, like matching short period P-waves. Shallow events allows for surface wave generation, whereas in case of deep earthquakes most of the energy is transmitted to the surface in form of body waves only (as seen on notes on **fk synthetics**).

4.4.1 Stations: MOOS and AEIC

Two seismic array have been set up in Alaska under two different experiment, i) BEAAR (Broadband Experiment Across the Alaska Range) ii) Multidisciplinary Observations of Onshore Subduction (MOOS). Most of the stations in South Central Alaska (SCAK) comes under dense cluster of MOOS array (34 stations). Stations from other network were also used in the study. For this event we had seismograms from these stations:

ALPI	PERI	EYAK	PS10
AVAL	RUSS	GOAT	PS11
BIGB	SOLD	KABU	PS12
BLAK	TUPA	KAKN	RAG
DEVL	AUL	KDAK	RC01
HEAD	BMR	MCK	RDWB
HOPE	BRLK	MID	RND
KASH	CAST	OHAK	SAW
LSKI	CHUM	PAX	SPBG
LSUM	DHY	PMR	SWD
MPEN	DIV	PPLA	TRF
NSKI	DOT	PS09	VMT

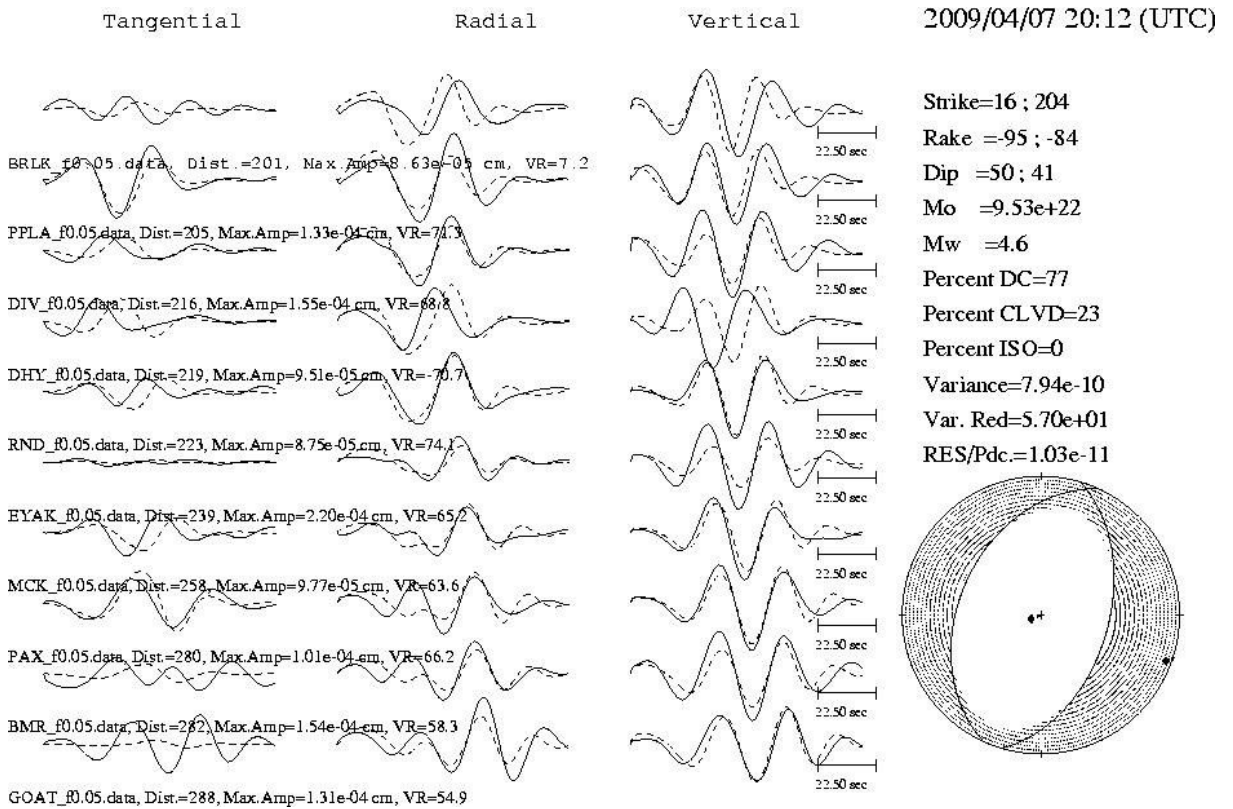


Figure 4.3: Moment Solution and the match between recorded and synthetics as generated by AEIC (Alaska Earthquake Information Center)

4.4.2 AEIC inversion

AEIC follow a good rule of thumb while picking frequency filter for doing waveform inversion

0.02 - 0.10 hz for $M \leq 3.9$

0.02 - 0.05 hz for $M = 4.0 - 4.9$

0.01 - 0.05 hz for $M \geq 5.0$

4.4.3 Commands used

1. Green's Function

```
fk.pl -Mscak/45 -N8192/0.02 dist1 dist2 dist3 . . .
```

2. CAP inversion

```
cap.pl -H0.02 -P0.8e+0.8/40 -S3/5/0 -T35/70 -D2/1/0.5 -C0.05/0.15/0.02/0.06
-W1 -Mscak_45/5.0 -Zweight_surf.dat 319605
```

4.4.4 CAP output details

1. text below the station label: distance_km/dt_data_syn (and azimuth)

- (a) dt_data_syn is the waveform shift that is applied to the entire waveform; this is the “reference alignment” prior to making the phase-specific measurements. This number will appear non-zero only if the first P arrivals were picked from the data and entered into the weight file. This P arrival is then matched with the green’s function. [dt_data_syn = (P arrival time of data, supplied in weight file) - (P arrival time for the synthetics, always present as T1 and T2 marker in green’s function header)].
- 2. below each waveform: time shift / cross-correlation coefficient
 - (a) time shift convention is such that a positive time shift means that the synthetic is earlier and need to be shifted in positive direction to match with the data. This means the model used is faster than the actual structural model. Total time shift = shift of complete waveform (“waveform shift” - see above) + shift of specific phase. The time window for each phase is estimated depending on the station’s epicentral distance and structural model (cause of incomplete at small distances).
 - (b) NOTE: The same time shift for SH and SV can be enforced using -S option. But if anisotropy is possible, this may not be desirable.
- 3. Black record - Data, Red - Synthetic.
- 4. Stations are sorted by epicentral distance (row 1 = closest stations)
- 5. There are three marks on the beachballs (see cap_plt.pl). These are modifications from the original plotting script.
 - (a) The solid circle (.) marks the station azimuth. It is always plotted just outside the beachball.
 - (b) The (x) is the lower hemisphere piercing point of the ray path from the source to the station. So when looking from above, the rays take off DOWN to pierce the lower hemisphere of the beachball. The correspondence between the x and the color of the beachball should be consistent with the observed first-motion polarity of P waves.
 - (c) The (o) is the upper hemisphere piercing point of the ray path. So when looking from above, the rays take off UP to pierce the upper hemisphere of the beachball. This is a supplemental mark; the corresponding lower hemisphere piercing point still appears as an x.

4.4.5 Structural Model

AEIC used two different structural models depending on the location of events. They used TACTmod about 62.5 latitude and SCAK below 62.5 latitude. We have used

southern Alaska (SCAK) model in our preliminary tests.

thickness	V_s	V_p	density	Q_p	Q_s
4.0000	3.0100	5.3000	2.5200	300.0000	600.0000
5.0000	3.1800	5.6000	2.6100	300.0000	600.0000
5.0000	3.5200	6.2000	2.7800	300.0000	600.0000
5.0000	3.9200	6.9000	2.9700	300.0000	600.0000
5.0000	4.2000	7.4000	3.1200	300.0000	600.0000
9.0000	4.3700	7.7000	3.2000	300.0000	600.0000
16.0000	4.4900	7.9000	3.2600	300.0000	600.0000
17.0000	4.6000	8.1000	3.3200	300.0000	600.0000
0	4.7200	8.3000	3.3700	300.0000	600.0000

4.4.6 Surface wave Inversion

We start with the AEIC_MT stations and then keep adding surface waves from other stations one by one. Starting with AEIC is an easy priori since we are pretty much sure that AEIC_MT inversion gives an approximate focal mechanism. We used surface waves between 16 - 50 sec period.

COMMANDS used:

```
----- For CAP inversion-----
cap.pl -H0.02 -P0.6e+0.8/60 -S3/5/0 -T35/120 -D2/1/0 -C0.05/0.15/0.02/0.06
      -W1 -Mscak_45/5.0 -Zweight_surf.dat 319605
      -H sample interval
      -P scaling
      -S maximum shift
      -T maxmimum time window for body/surf
      -C filter .05 - .15 (body wave)
                  .02 - .06 (surface wave)
      -W1 velocity record
----- For Green's Function using FK-synthetics-----
fk.pl -Mscak/48 -N8192/0.02 282 201 219 216 239 288 258 280 205 223 122
      104 101 65 49 115 88 89 109 78 162 121 127 132 25 16 250 300 381 293
      512 36 343 301 236 245 300 40 199 85 150 225 185
```

4.4.7 Observational Conclusion:

1. Most of the Surf V. and Surf R. have a positive time shift. AND SH have a negative time shift (usually).

- (a) Our source is well resolved, so could be due to bad structural model. Love wave looks at the shallow structure and -ve shift means synthetic is being pulled back. So, actual shallow structure might be a bit fast. Rayleigh is more sensitive for a little less shallow (more depth) structure. So positive shift implies that actual deeper structure might be slightly faster.
 - (b) Or could be due to anisotropy. Shear wave splitting and travelling with different velocity.
2. Energy following main Love wave waveform (SH) in case of RDWB, SAW, PS09, PS10.

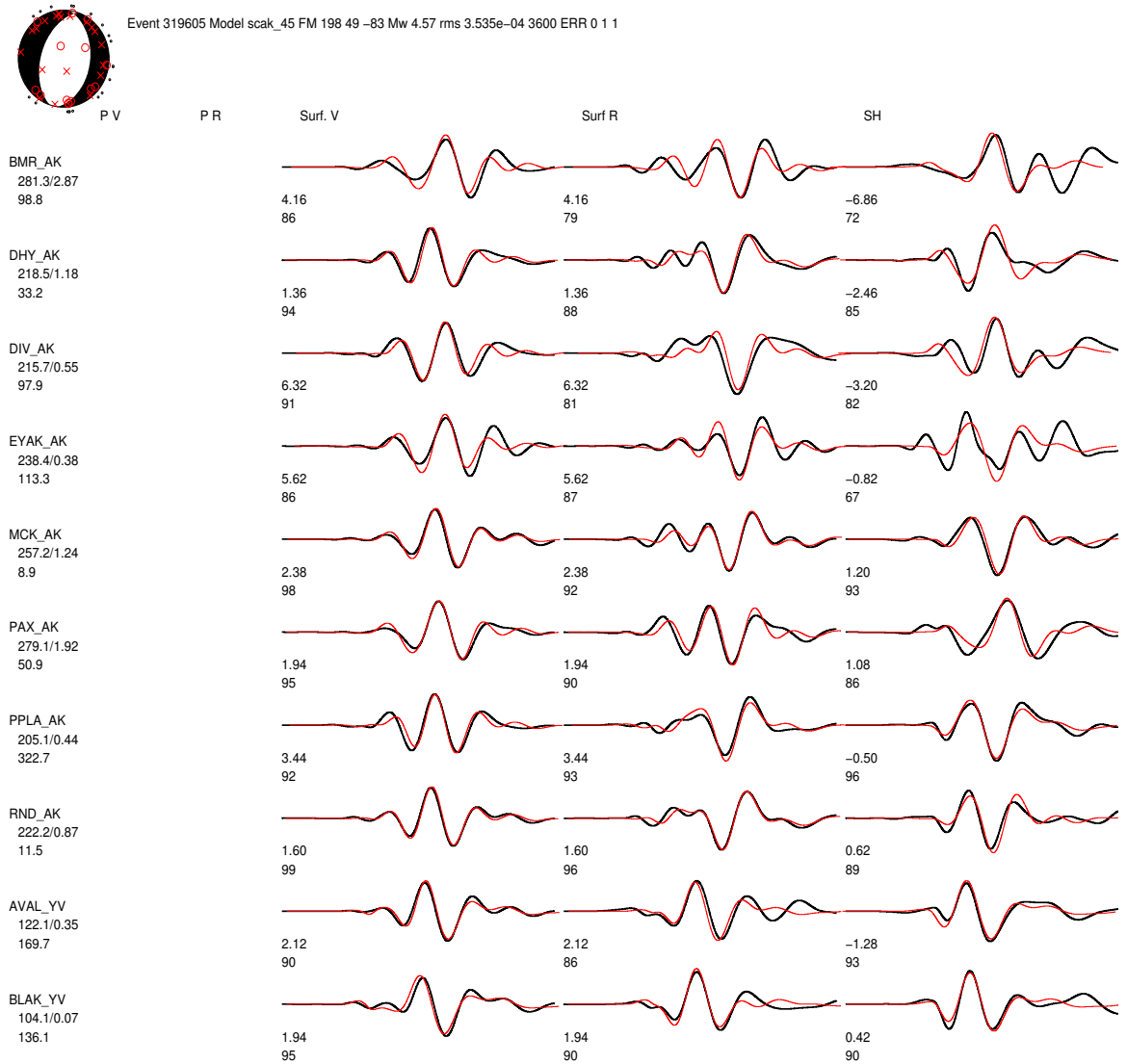
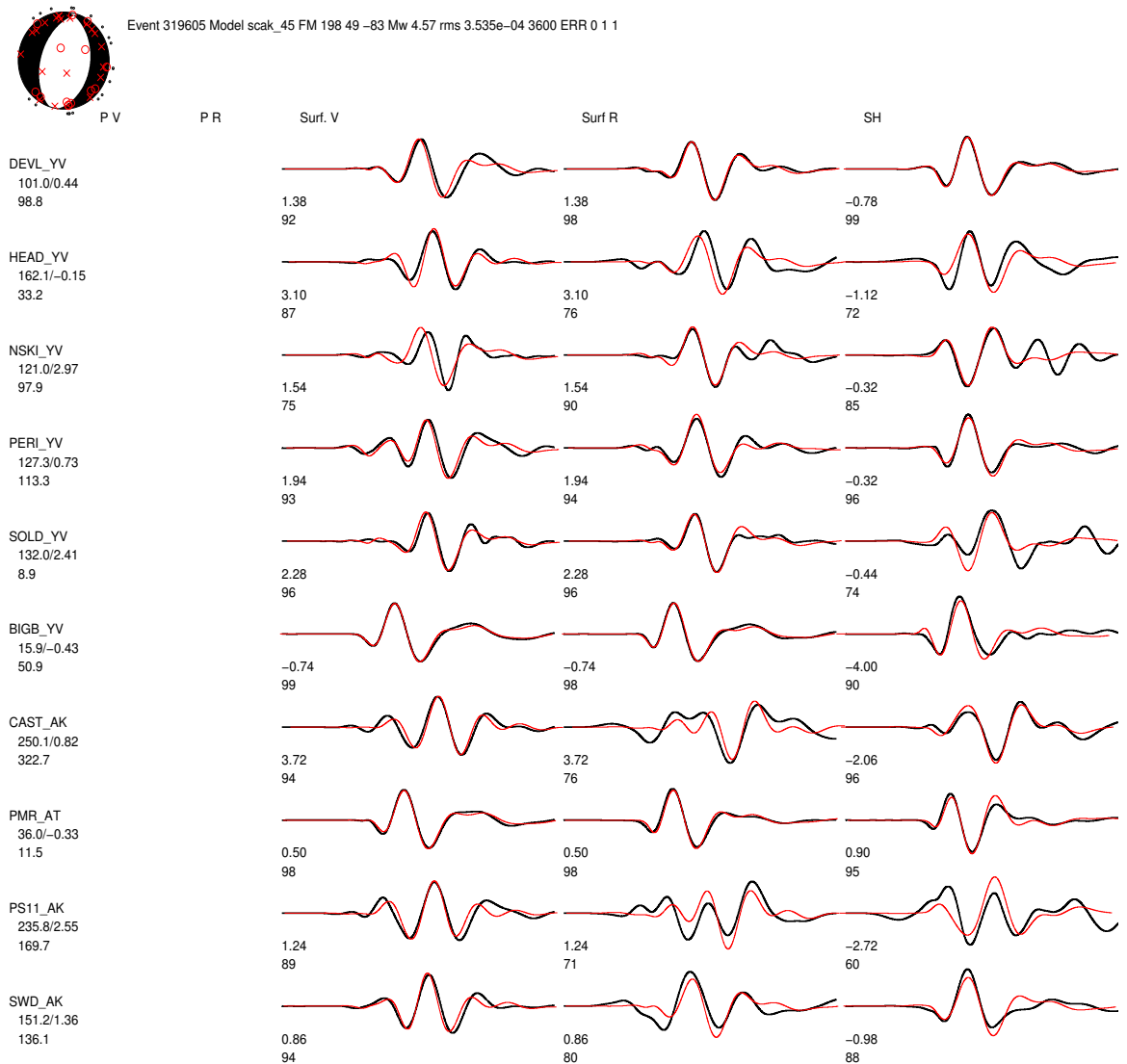


Figure 4.4: Inversion of event 319605 by only using the surface waves. A total of 20 good stations were chosen (Rest 10 in next page)



Depth estimation using only surface waves

The best 20 stations for which surface wave inversion was most stable were chosen for depth estimation.

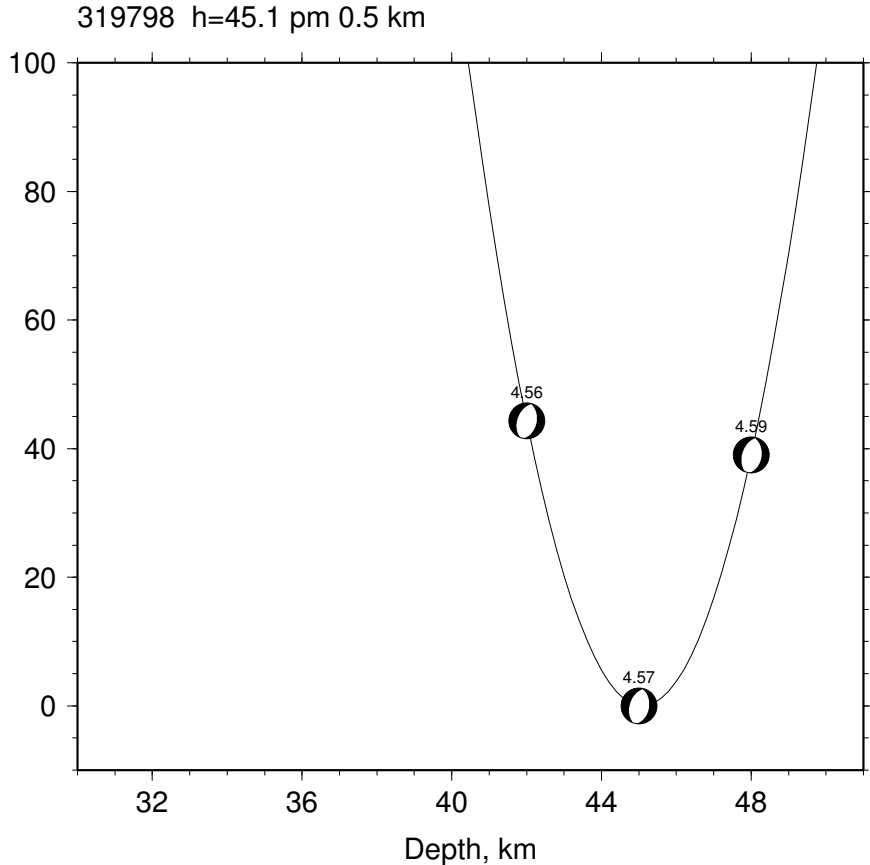


Figure 4.5: Depth estimation of eid 319605 using CAP surface waves

4.4.8 Body wave Inversion

Body waves are relatively more difficult to invert because they are of smaller period. Therefore we employed two different approaches to narrow down our search for good stations. We used .05 - .15 Hz waves. Out of 47 stations finally 19 good body wave stations were chosen.

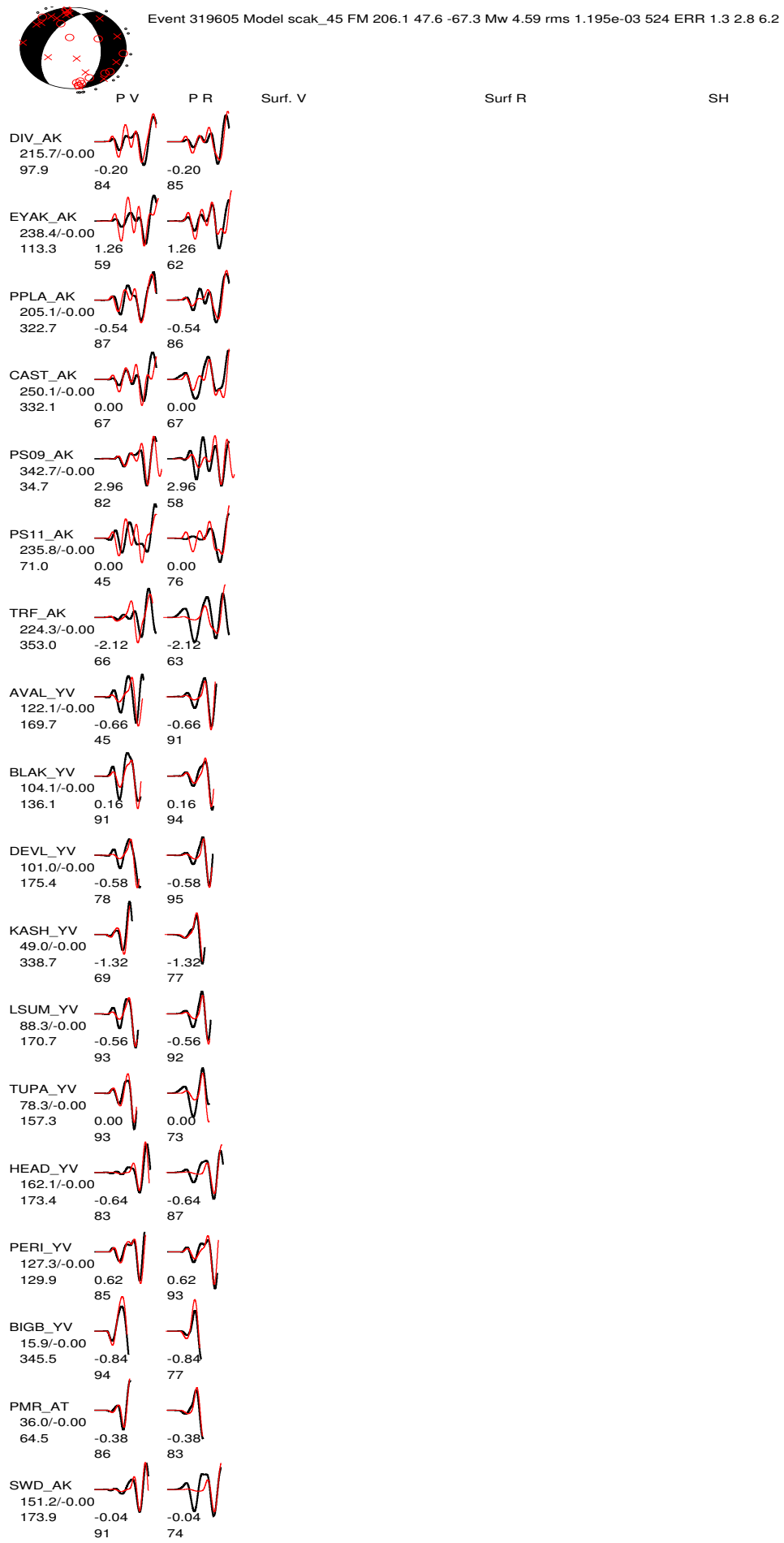
Approach 1

In this we divided the search into two parts, one with near stations and other with far stations. Near stations are relatively more helpful in inverting body waves (PnL) since they are directly coming from source and also have higher energy (not lost in surface waves). This is a very powerful step. We know that the body wave inversion is very unstable at small period. So we can start with this and see how huge the error is when all are used. Then we increase the period. Only the certainly bad won't fit. After removing them, and gradually decreasing the period we again come to the smaller

period and notice a huge decrease in error. In this way we can utilize the instability of body to eliminate the bad stations

Approach 2

This is a simple and strong approach. We know that surface are easy to invert. Once we have obtained a good solution by using only the surface waves, we can add one body wave at a time to check whether it is in parity with the result. If it fits, it means that its inversion might get us to correct answer. Since long period surface waves give almost gives a true mechanism, a non fitting body waves (hence not stable) can be marked suspicious. We will see that for near stations the both these approaches gives almost same stations. For far stations Approach 2 can be used and then rechecked by Approach 1.



Depth estimation using only body waves

As said, body wave inversion becomes a little unstable when using distant station, only near station (mainly MOOS) were used for depth inversion.

AVAL	BLAK	DEVL	HOPE
KASH	LSKI	LSUM	TUPA
HEAD	PERI	BIGB	PMR
RC01	SAW	SWD	

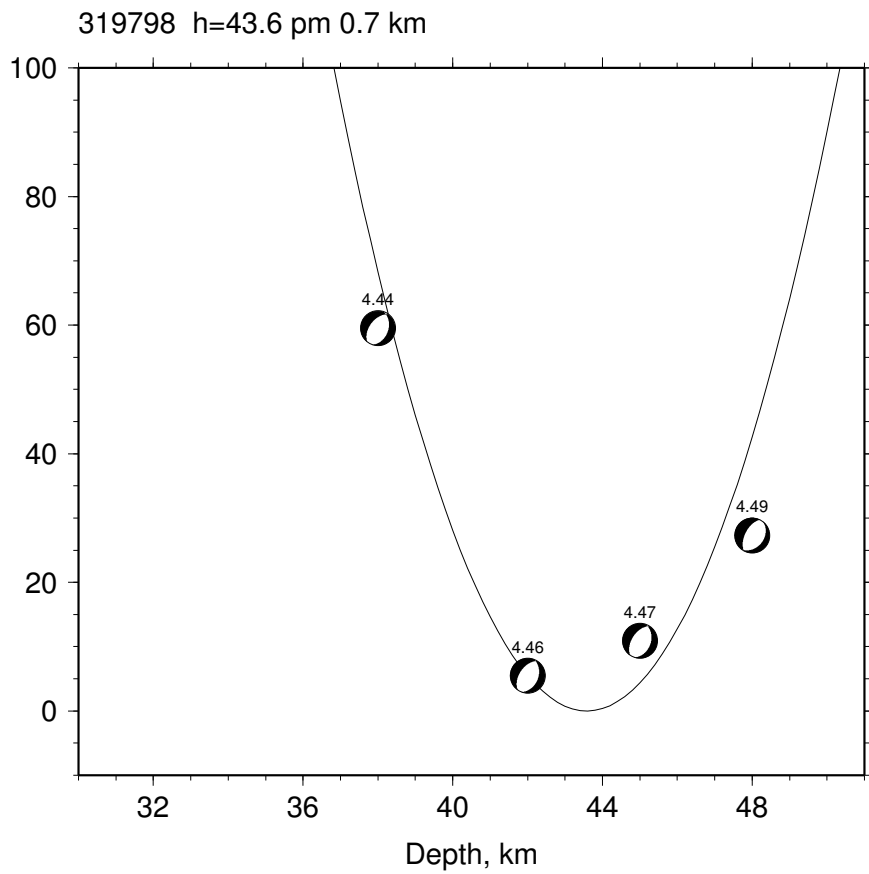


Figure 4.7: Depth estimation by taking only the body waves from nearby station since they are more stable

4.4.9 Inversion with Body and Surface waves

This event was record at 49 stations. Finally we used 20 surface waves and 19 body waves (not necessarily same).

319605					
STNM	NETWK	Dist	Body	Surf	Remark
BIGB	YV	15.850182	✓	✓	Closest- surface waves not that strong suspicious for body wave
ALPI	YV	25.741318			
PMR	AT	36.015823	✓	✓	
FIB	AK	39.70838			only Z component was present; SURE BAD
RC01	AK	40.696068			Body wave couldn't get full pulse
KASH	YV	49.029663	✓		
HOPE	YV	65.144897			Body wave couldn't get full pulse
TUPA	YV	78.342773	✓		
SAW	AK	84.534767			OK match for surface wave; Body wave couldn't get full pulse
LSUM	YV	88.33255	✓		
MPEN	YV	89.499893			
DEVL	YV	100.985985	✓	✓	
BLAK	YV	104.126137	✓	✓	
RUSS	YV	108.781143			suspicious for body wave
LSKI	YV	114.987999			suspicious for body wave
NSKI	YV	121.048615		✓	SURE BAD body wave
AVAL	YV	122.101341	✓	✓	
PERI	YV	127.296181	✓	✓	
SOLD	YV	132.023468		✓	SURE BAD body wave
SPBG	AV	142.332275			SURE BAD
SWD	AK	151.240311	✓	✓	
HEAD	YV	162.120361	✓	✓	
VMT	AK	185.634979			
RDWB	AV	199.513229			suspicious match for both, but not great
BRLK	AK	200.284714			BAD
PPLA	AK	205.088913	✓	✓	
DIV	AK	215.74704	✓	✓	
DHY	AK	218.491241			
RND	AK	222.21373	✓	✓	
TRF	AK	224.274338	✓		OK match for surface wave; NODAL
PS11	AK	235.779816	✓	✓	
EYAK	AK	238.37468	✓	✓	
PS12	AK	245.046127			surface wave were in top 27. Energy following main love wave due to basin
CAST	AK	250.100449	✓	✓	
MCK	AK	257.195923		✓	NODAL
PAX	AK	279.138214		✓	
BMR	AK	281.335052		✓	
GOAT	AK	287.985809			
MID	AT	293.34906			
RAG	AK	299.331299			
PS10	AK	300.26709			surface wave were in top 27. Energy following main love wave due to basin
CHUM	AK	301.005585			suspicious
AUL	AV	307.7595			only E component was present (bad signal in NE when tested earlier; SURE BAD)
PS09	AK	342.736786	✓		surface wave were in top 27. Energy following main love wave due to basin
DOT	AK	380.533936			suspicious
KDAK	II	438.8422			N-E not orthogonal; SURE BAD
KAKN	AV	460.769958			SURE BAD
KABU	AV	471.106232			SURE BAD
OHAK	AT	512.582153			SURE BAD body wave

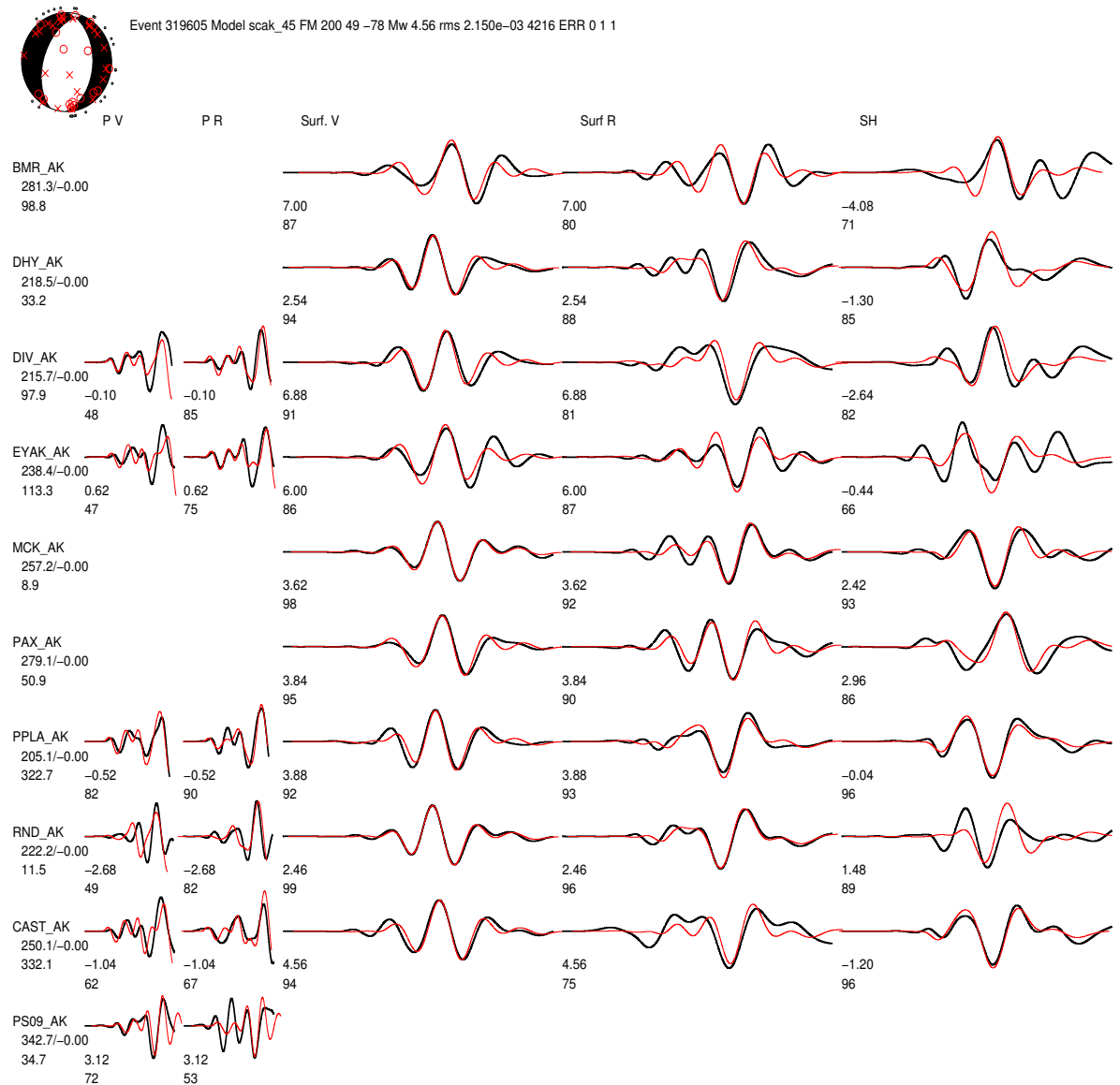
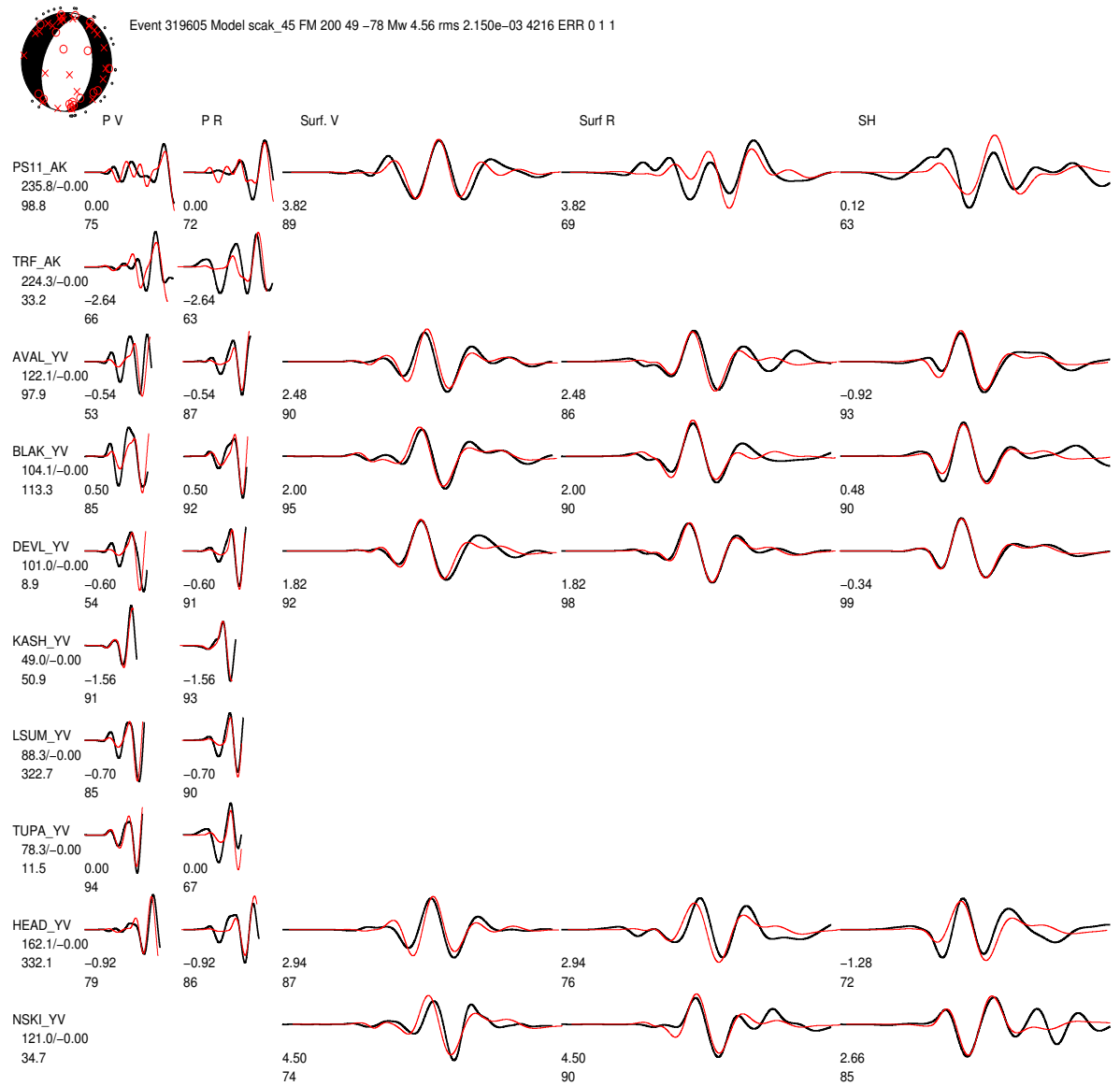
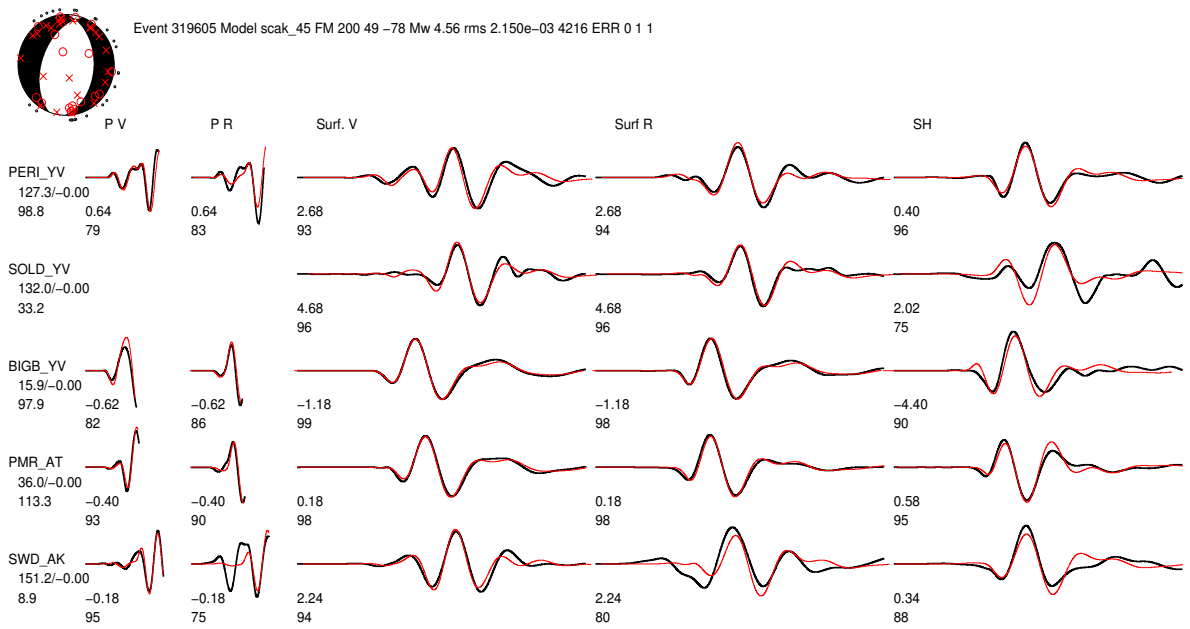


Figure 4.8: CAP moment tensor inversion of 319605 using both body and surface waves





Depth Estimation

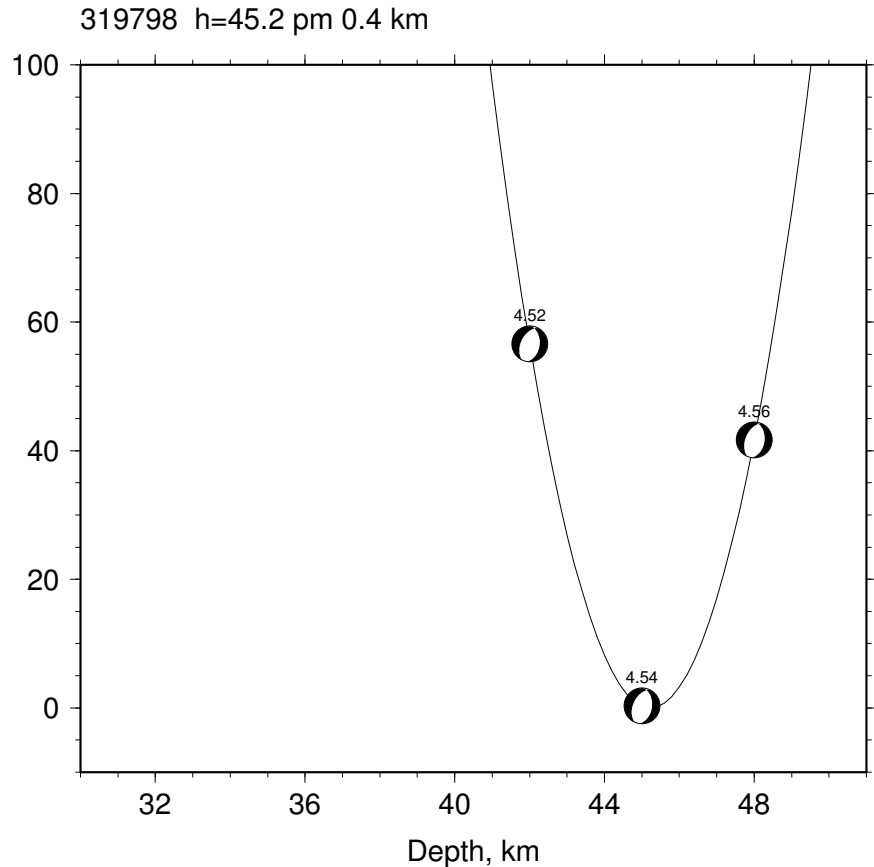


Figure 4.9: Depth estimation of 319605 using both the surface and the body waves

4.4.10 Results

319605									
	strike	dip	rake	Mw	depth	lat	lon	otime	
AEIC	204	41	-84	4.6	45	61.45	-149.74	2009-04-07 20:12:55	
CAP (surf)	198	49	-83	4.57	45				
CAP (body)	206	47	-67	4.59	43				
CAP (both)	200	49	-78	4.56	45				

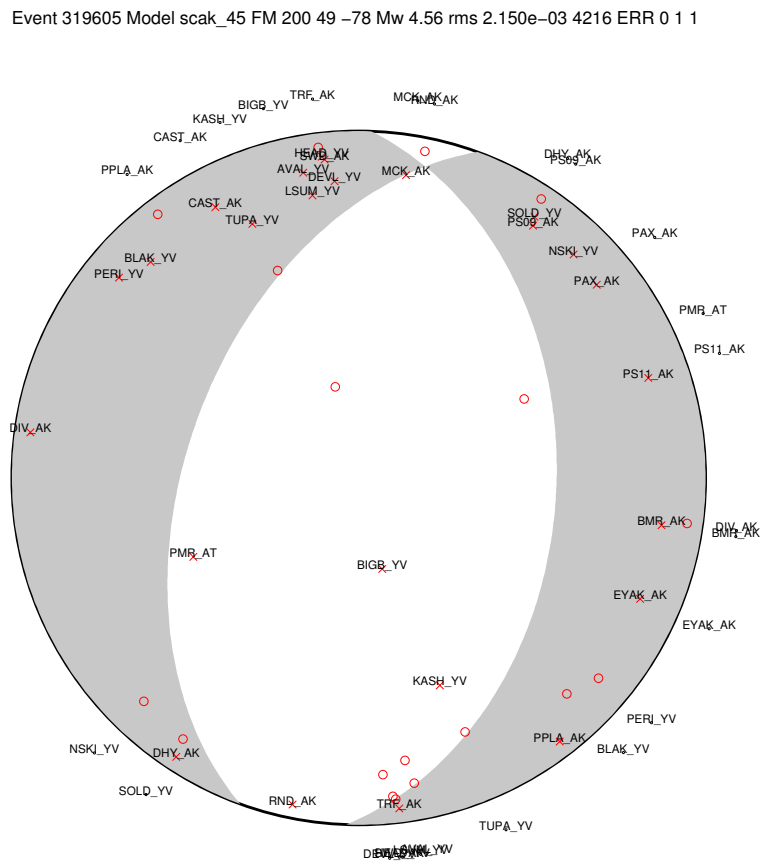


Figure 4.10: Beachball representation of this event along with the different station used. 0 - shows where the rays paths cut the hemisphere. x- shows where it cuts in the lower hemisphere (if it actually cuts upper hemisphere, as for nearby stations, and lies in the tension quadrant, then it must be project in lower hemisphere such that it still in same place of tension quadrant. outside the ball shows actual azimuth of the stations.

4.5 EXAMPLE EVENT 2 (eid 289317)

otime	lon	lat	MT_dep	AEIC_dep	Mw	AEIC_id
2008-03-14 (2008074) 09:38:21	-152.64	61.07	165.00	(143.65)	4.97	289317

Next we chose this event for moment tensor inversion test since this is a deep slab event. We expect this event not to produce large surface waves and most of the energy will be concentrated in body wave phase. Hence, good for testing inversion using body wave (Pnl).

4.5.1 Comparison: AEIC moment tensor solution with CAP

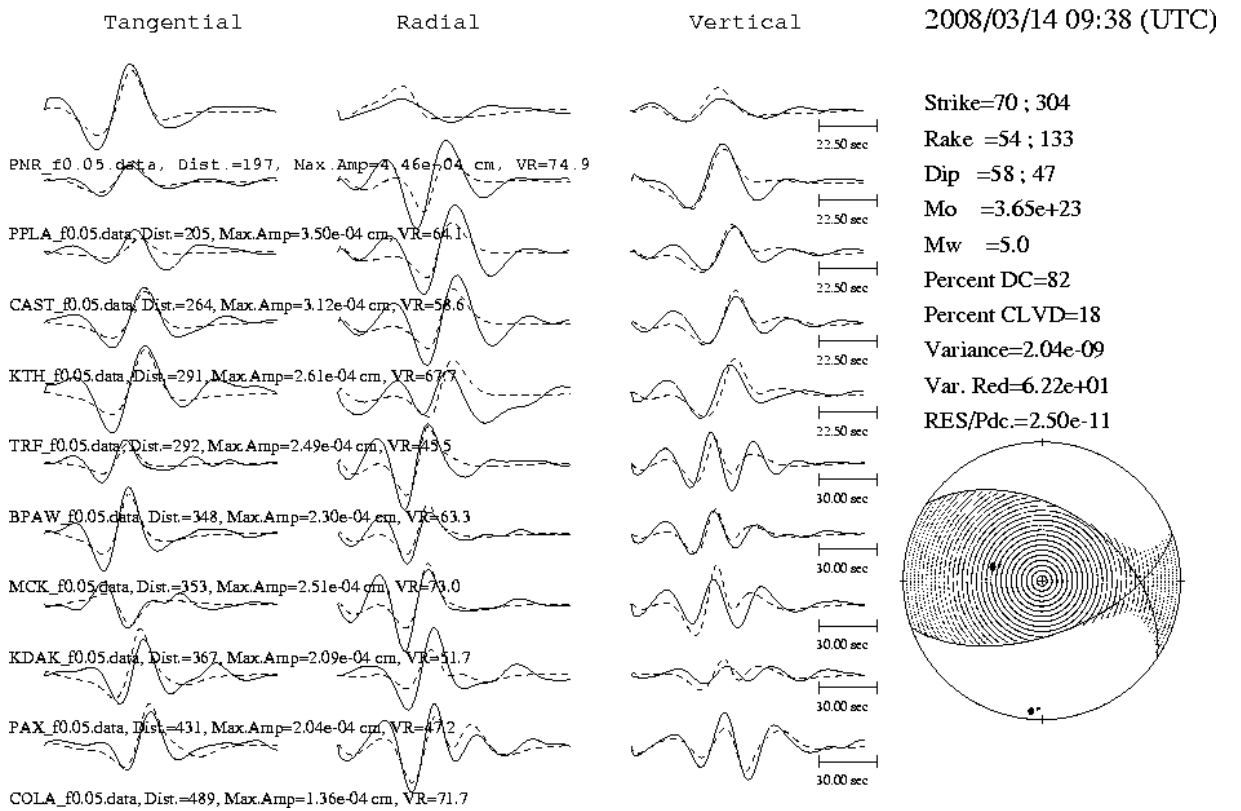


Figure 4.11: AEIC moment tensor solution for 289317.

Record Section

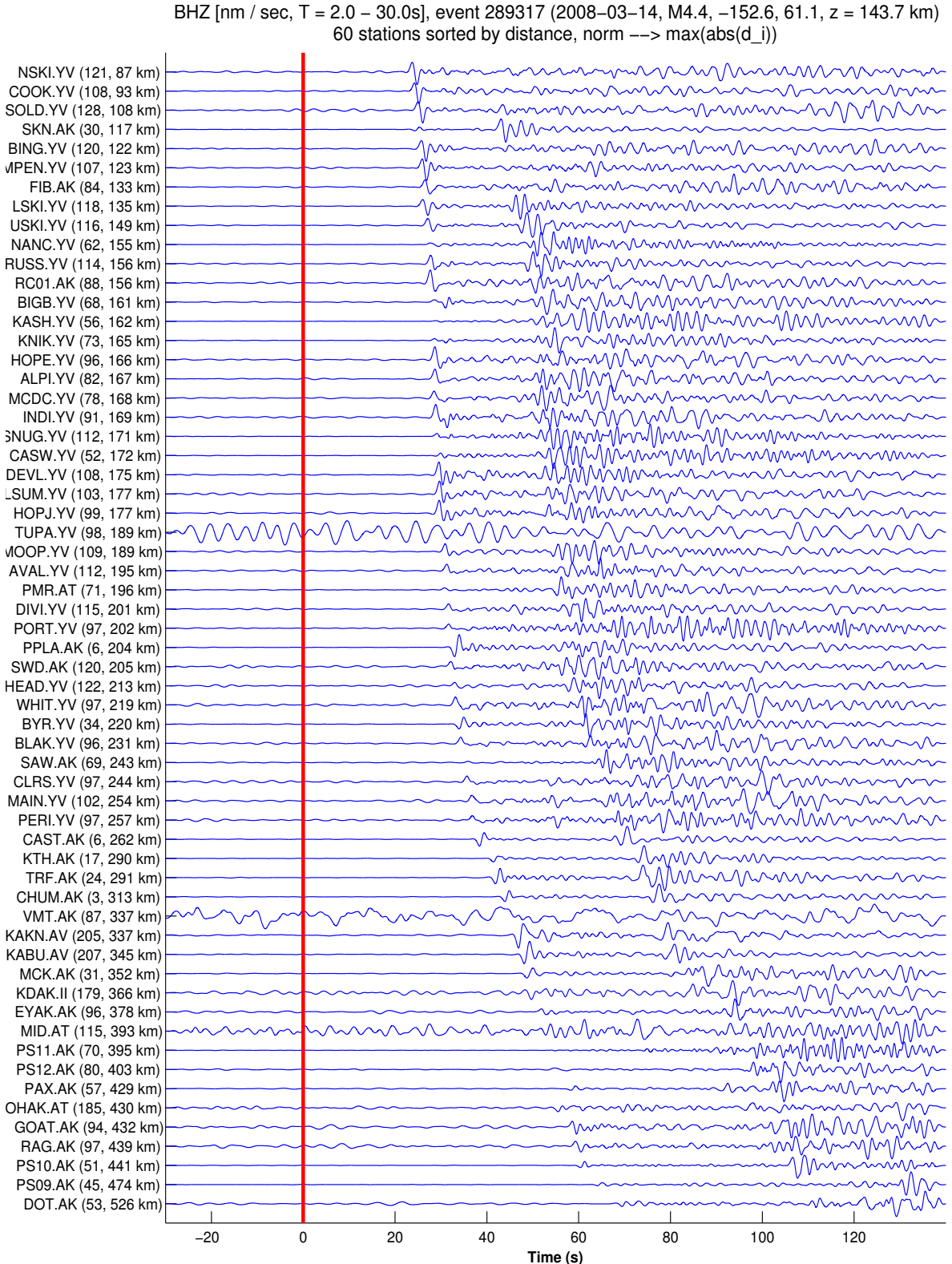


Figure 4.12: Record section of 60 station where this event was recorded and have been used for CAP moment tension solution. This plot can be used to readily eliminate the bad stations. courtesy: Carl Tape

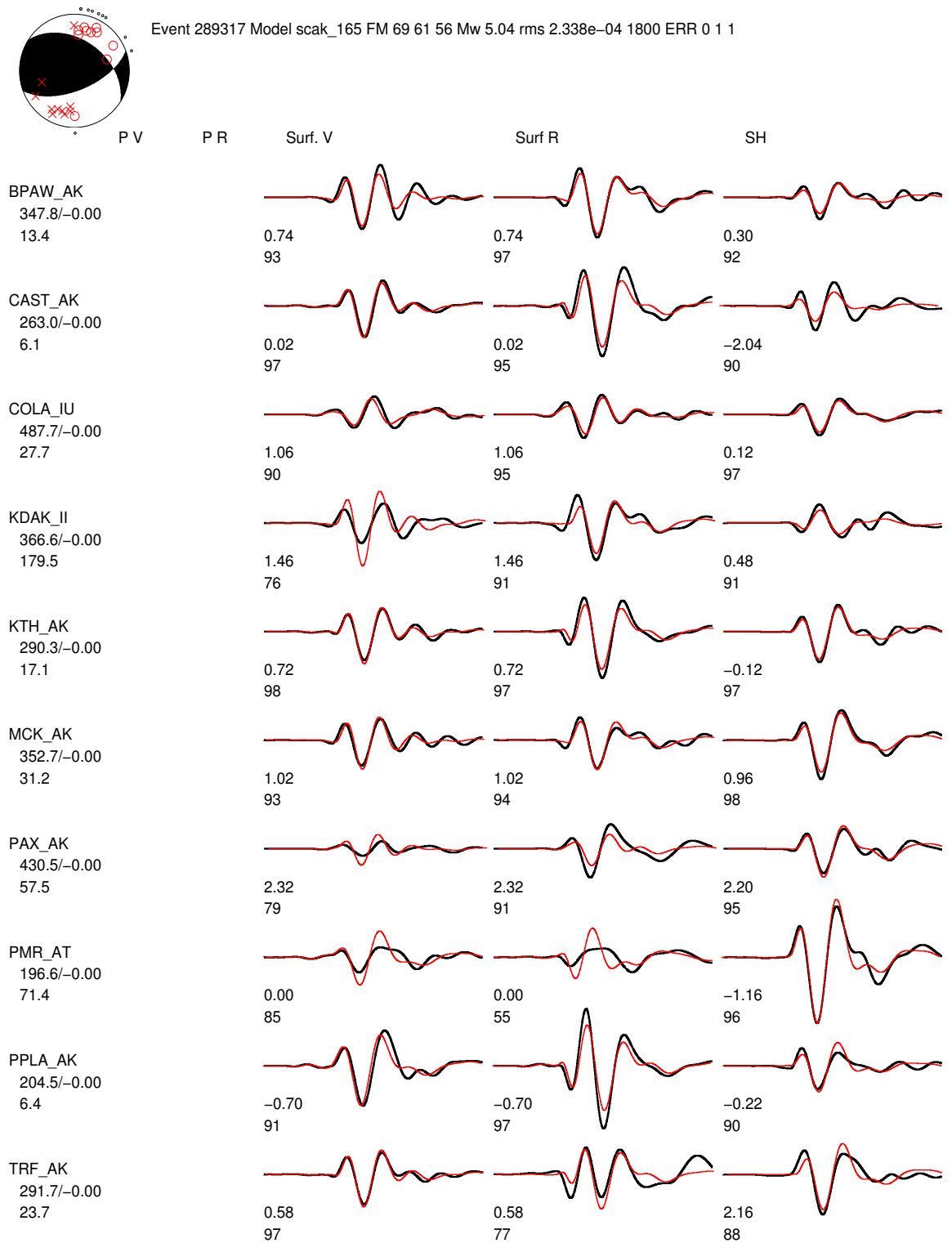


Figure 4.13: CAP moment tensor solution for 289317 (Using same stations used by AEIC).

4.5.2 Results

289317								
	strike	dip	rake	Mw	depth	lat	lon	otime
AEIC	70	58	54	5	165	61.07	-152.64	2008-03-14 09:38:21
CAP (surf)	60	60	23	5.06	143			
CAP (body)	64	67	33	4.96	141			
CAP (both)	60	67	31	4.98	145			

4.5.3 ‘tshift’ plot

‘tshift’ plot can be utilized for checking the overall azimuth and epicentral variation of ‘tshift’ and ‘cross-correlation value’. Physically speaking, tshift describes the error between our structural model and the true model. We can utilize tshift plot for two following purposes:

1. Structural model variation is generally smooth. Even if we enter wrong structural model, the variation of tshift-value and cc-value with azimuth must be smooth. This way we can remove anomalous (bad) stations.
2. By using the physical definition of tshift, we can utilize it to improve our structural model and hence prepare tomographic model.

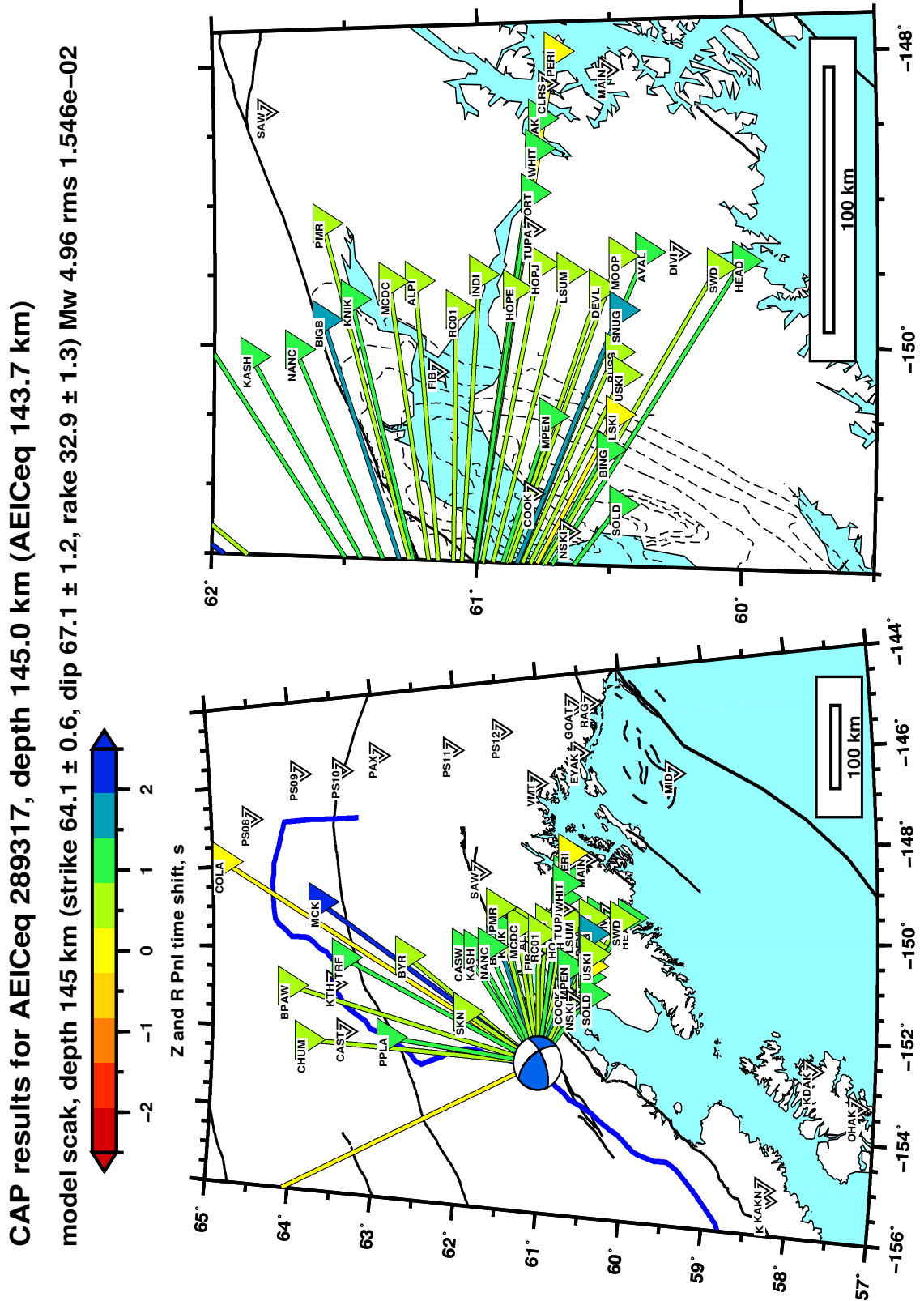
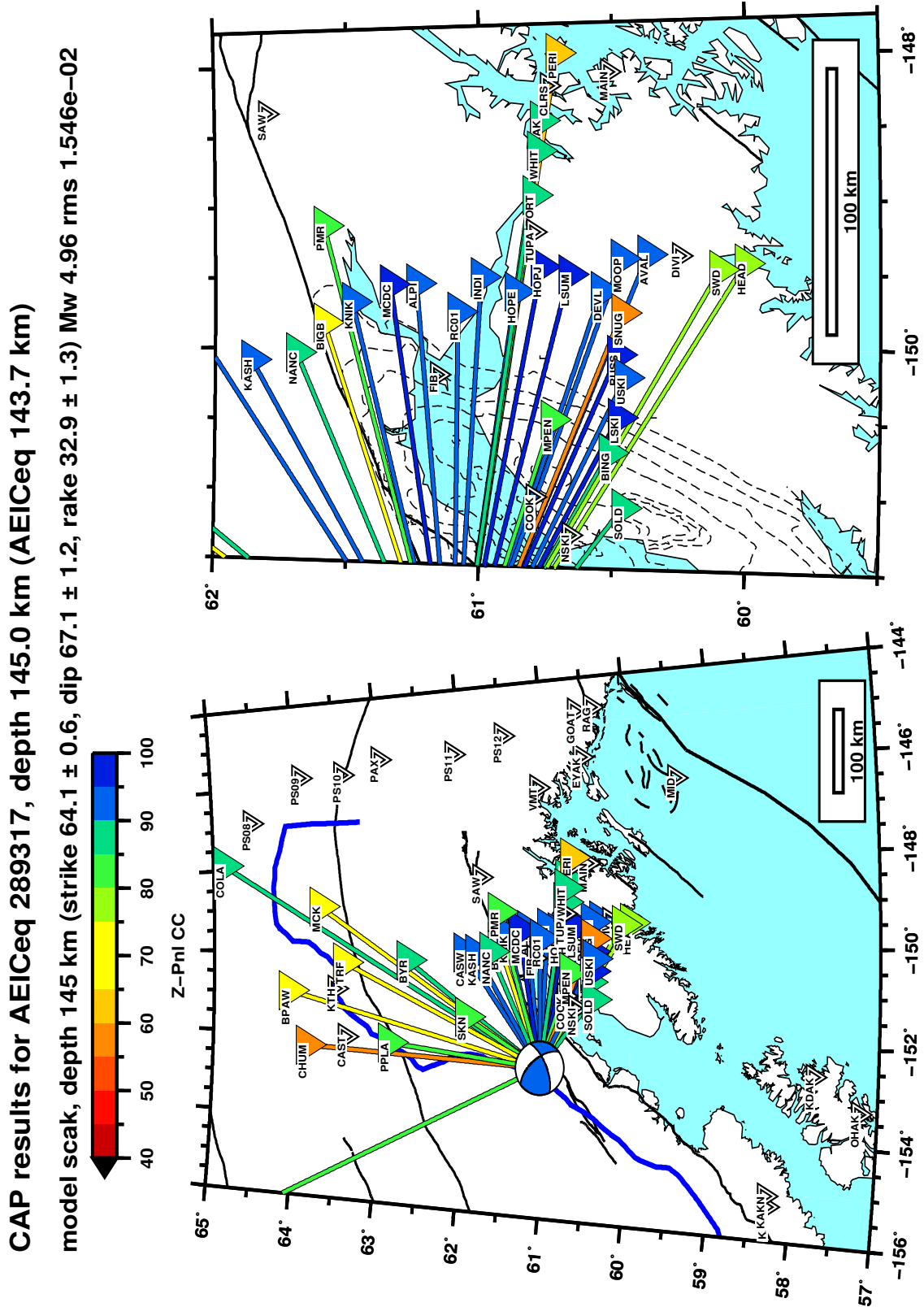
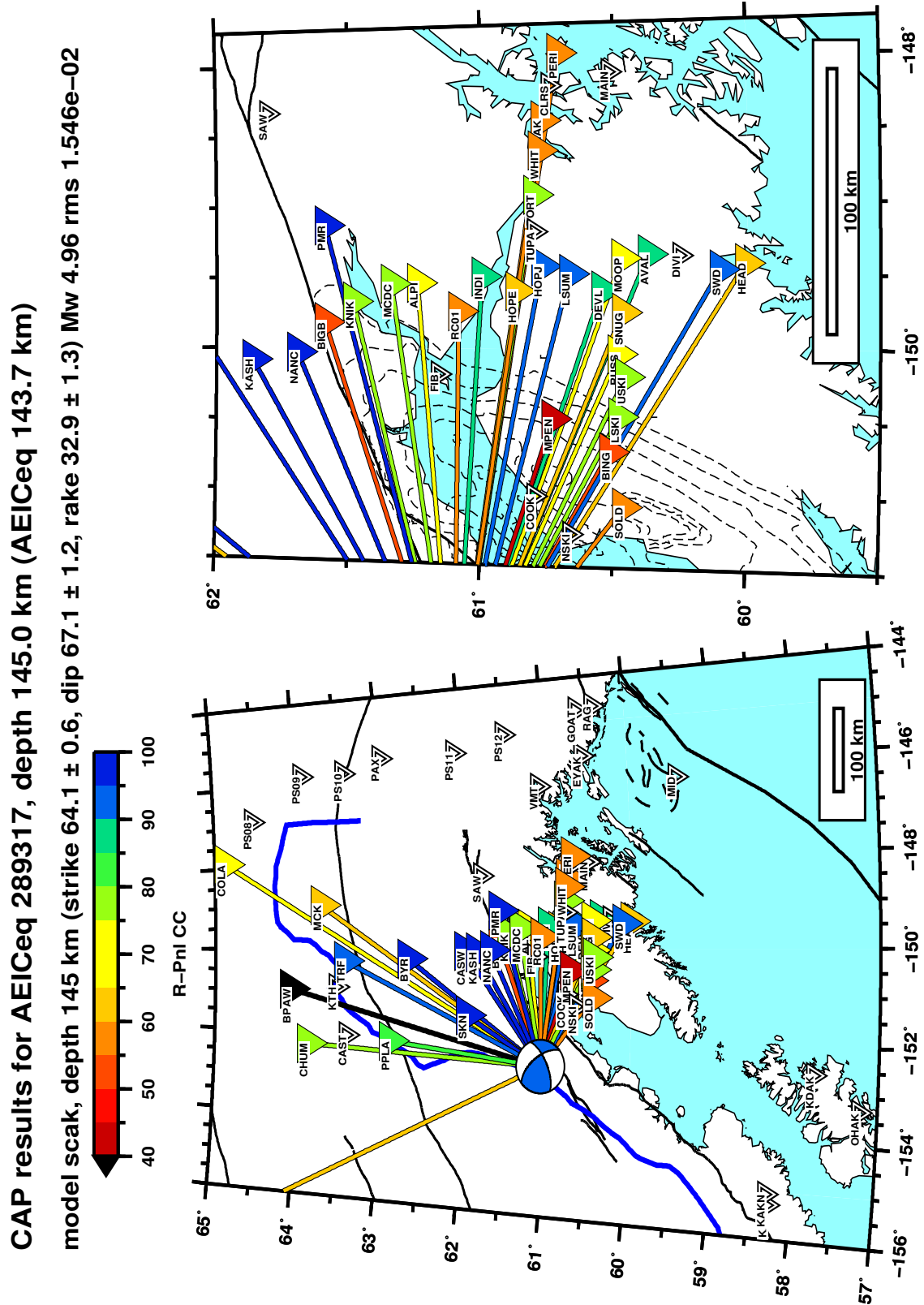
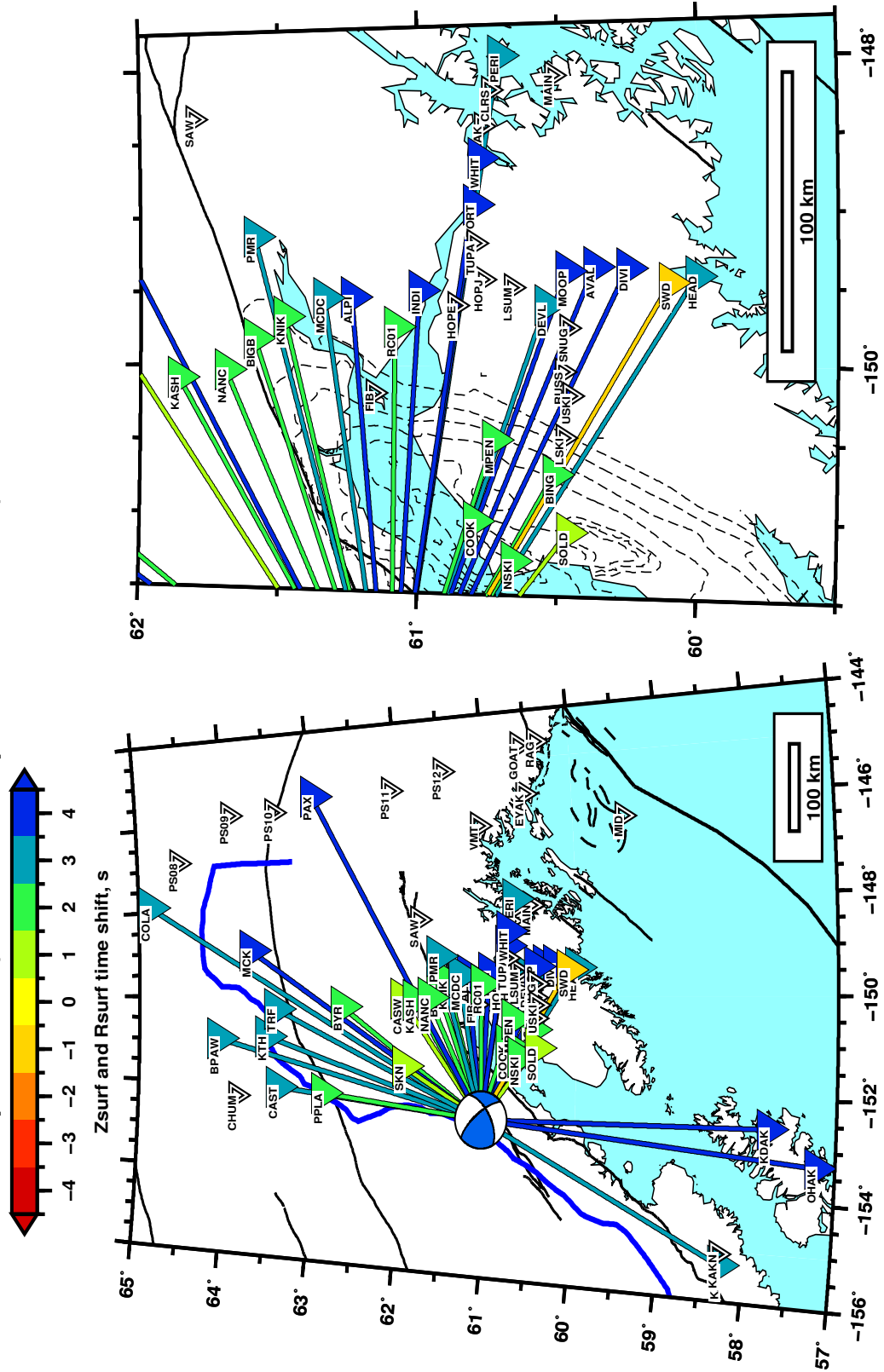


Figure 4.14: 'tshift' plot for 289317.

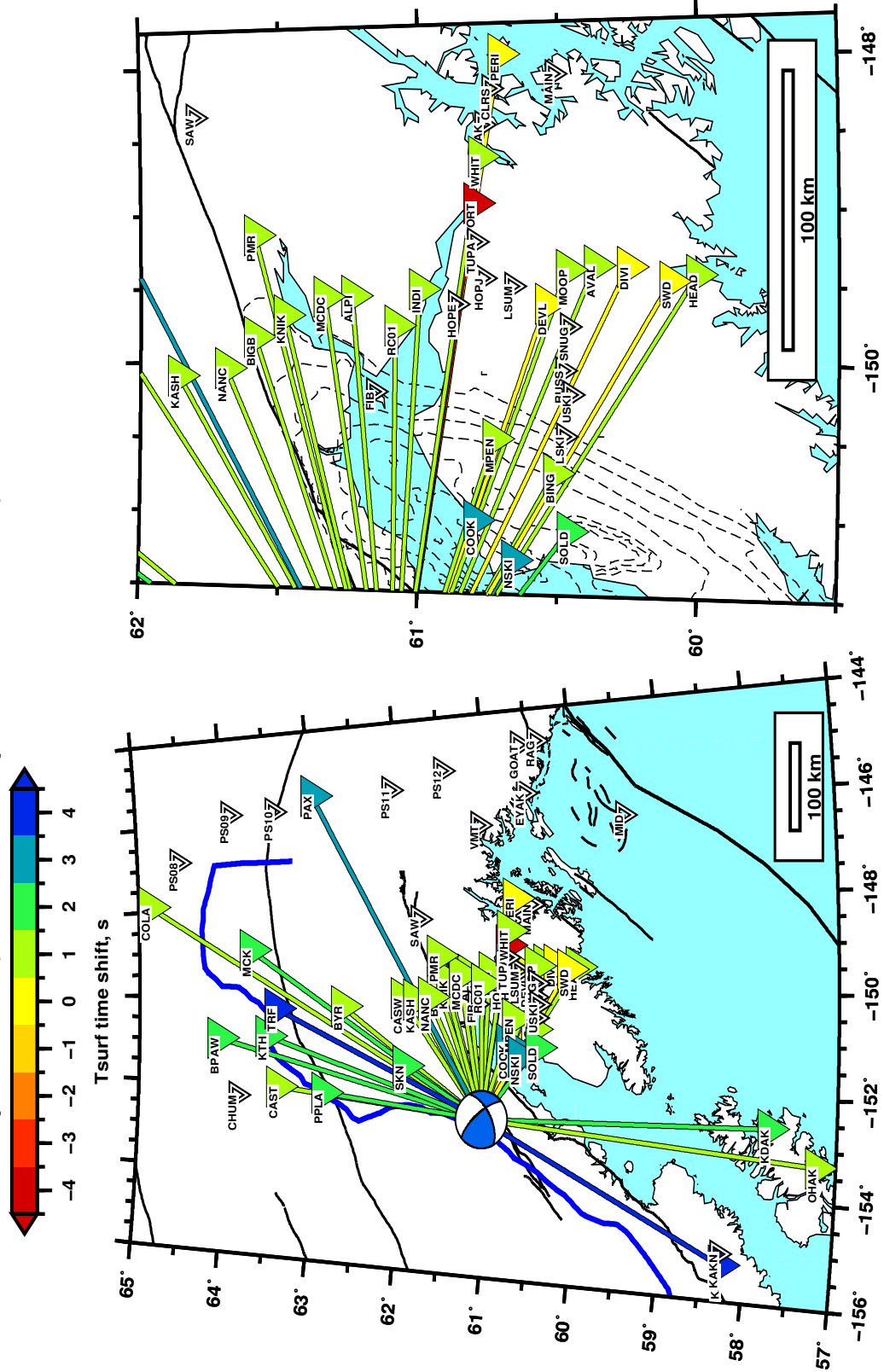




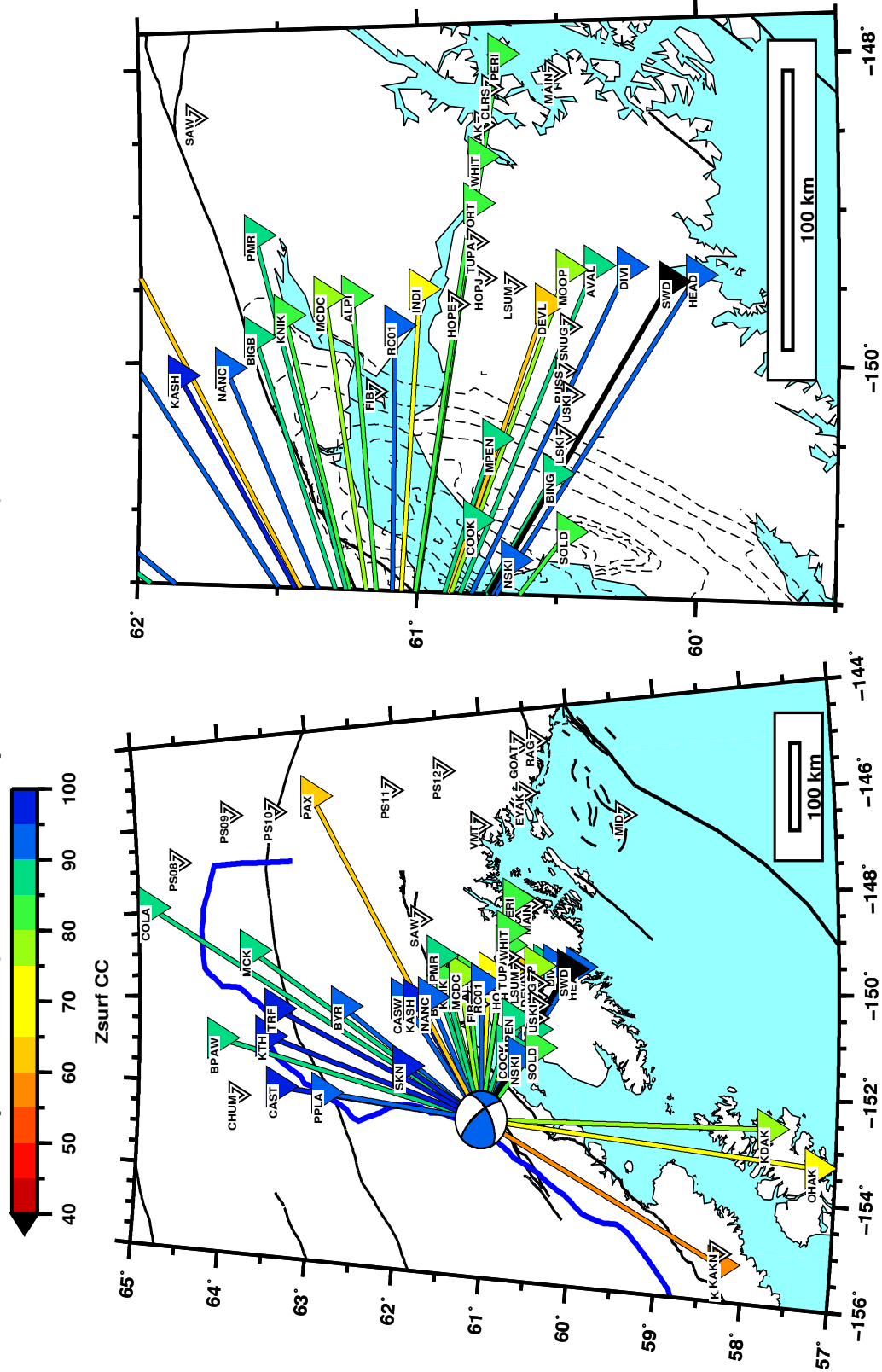
CAP results for AEICeq 289317, depth 145.0 km (AEICeq 143.7 km)
 model scak, depth 145 km (strike 60 ± 0 , dip 60 ± 0 , rake 23 ± 0) Mw 5.06 rms 4.887e-03



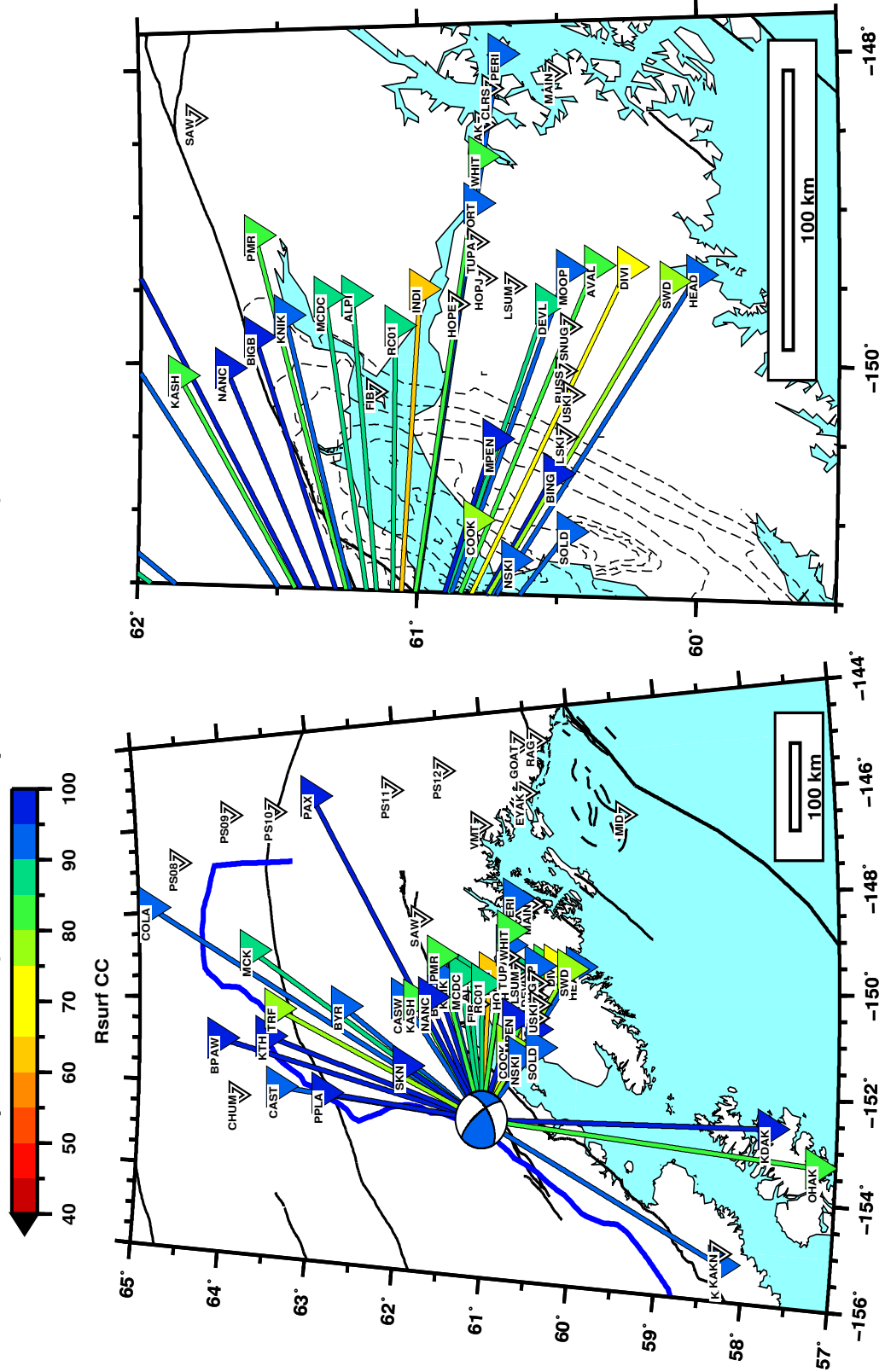
CAP results for AEICeq 289317, depth 145.0 km (AEICeq 143.7 km)
 model scak, depth 145 km (strike 60 ± 0 , dip 60 ± 0 , rake 23 ± 0) Mw 5.06 rms 4.887e-03



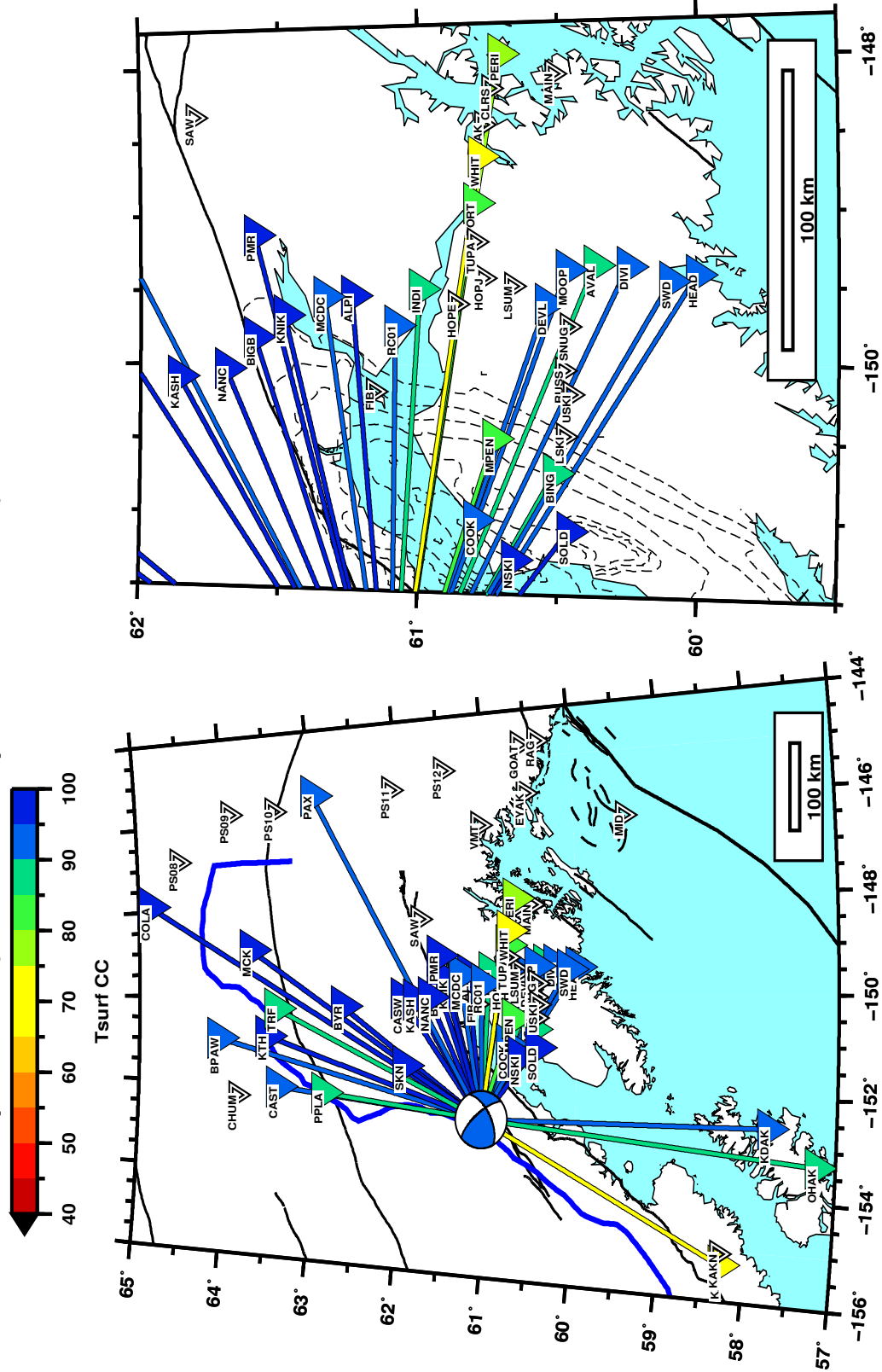
CAP results for AEICeq 289317, depth 145.0 km (AEICeq 143.7 km)
 model scaik, depth 145 km (strike 60 ± 0 , dip 60 ± 0 , rake 23 ± 0) Mw 5.06 rms 4.887e-03



CAP results for AEICeq 289317, depth 145.0 km (AEICeq 143.7 km)
 model scaik, depth 145 km (strike 60 ± 0 , dip 60 ± 0 , rake 23 ± 0) Mw 5.06 rms 4.887e-03



CAP results for AEICeq 289317, depth 145.0 km (AEICeq 143.7 km)
 model scaik, depth 145 km (strike 60 ± 0 , dip 60 ± 0 , rake 23 ± 0) Mw 5.06 rms 4.887e-03



4.6 Special event: Nenana earthquake

This event occurred in Nenana Basin (central Alaska) around half an hour after the 8.6 Sumatra earthquake (April 11, 2012). Sumatra earthquake occurred at 0848 UTC, whereas the Nenana earthquake at 0922 UTC. This occurred when the love waves generated by Sumatra earthquake were passed over Alaska and were near its peak (around 4cm). This appear to be a classic case of dynamic triggering of an earthquake. I did the focal mechanism inversion of Nenana earthquake, and it was found that it was quite similar to that of the 1995 Nenana earthquake. The focal mechanism of the Nenana earthquake indicates a fault plane that is similar to the direction of maximal Love wave motion in central Alaska (to the northeast).

4.6.1 Sumatra earthquake

The Sumatra earthquake occurred due to strike slip faulting near the Tundra trench in Indian Ocean. It was a magnitude Mw 8.6, followed by Mw 8.2 aftershock.

otime	lat	lon	depth	Mw	strike	dip	rake
2012-04-11 08:39:29.8	2.24N	92.18E	40	8.6	289	89	154

4.6.2 CAP inversion

This event occurred in Internal Alaska and we had to use different structural model for it. For this region, TACTMOD model have been proposed, and even AEIC utilizes the same. The green's function were computed using this structural model.

thickness	V_s	V_p	density	Q_p	Q_s
3.0000	3.0700	5.4000	2.5500	300.0000	600.0000
8.0000	3.3500	5.9000	2.6900	300.0000	600.0000
13.0000	3.5500	6.2500	2.7900	300.0000	600.0000
7.0000	4.0300	7.1000	3.0300	300.0000	600.0000
45.0000	4.4900	7.9000	3.2600	300.0000	600.0000
0.0000	4.7100	8.2900	3.3700	300.0000	600.0000

Importance and complications

This event is quite special from many perspectives.

1. This event seems to be triggered by the high amplitude love waves originated from the Sumatra earthquake.
2. The earthquake occurred in the same fault zone in which Nenana 1995 (Mw 6) happened.

3. This is a shallow event, and hence, high amplitude phases makes it possible to use both body and surface waves for inversion.
4. Since this is a small magnitude event, it would also test the robustness of CAP. We would be requiring smaller period phases for the focal mechanism inversion.

The complications arose mainly because of two important reason. Firstly, because of it being a small magnitude and simultaneous passage of long period love waves force us to use short period phases (1-4 sec). Therefore, for the inversion of this event we used body waves (1-3 sec) and surface waves (2-4 sec). Another complication arose because of good stations being at small epicentral distance. This sometimes restricts CAP from clearly partitioning into Pnl and Surf wave phases. To get our way around this problem, I used combined Pnl and Rayleigh waves for the moment tensor inversion.

4.6.3 Results

Nenana 2012								
	strike	dip	rake	Mw	depth	lat	lon	otime
AEIC	-	-	-	-	20	64.9	-148.8	2012-04-11 09:21:57
CAP (surf)	-	-	-	-	-			
CAP (body)	200	84.6	-15.4	3.8	30			
CAP (both)	189	69.8	-38.4	3.88	19			
Nenana 1995								
	strike	dip	rake	Mw	depth	lat	lon	otime
GCMT	199	77	-1	6	15	65.28	-148.50	1995-10-06 05:23:24

The moment tensor inversion of Nenana 2012 reveals a focal mechanism similar to that Nenana 1995 event which also occurred in the same fault zone.

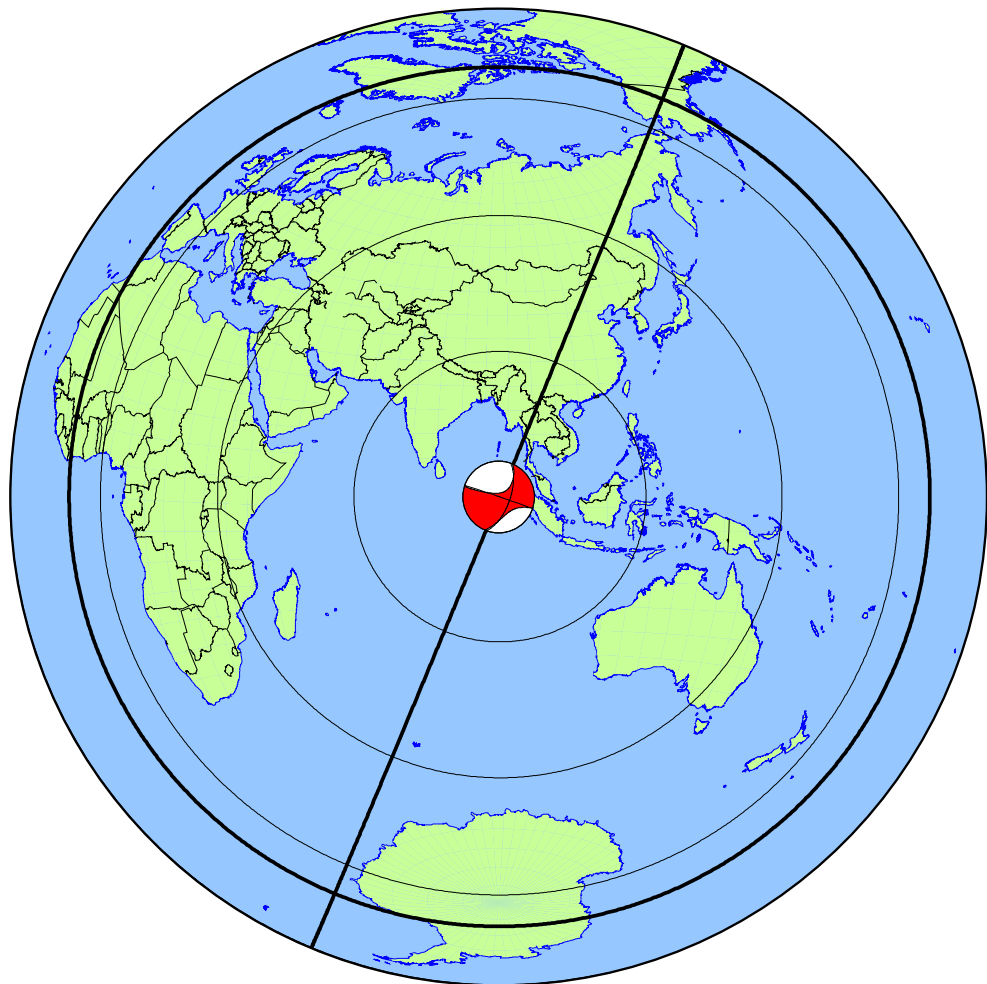


Figure 4.15: Map showing the location of magnitude 8.6 earthquake of Sumatra (which caused huge love wave in Alaska and also triggered an earthquake in Nenana fault). courtesy: Carl Tape

4.6.4 Record section

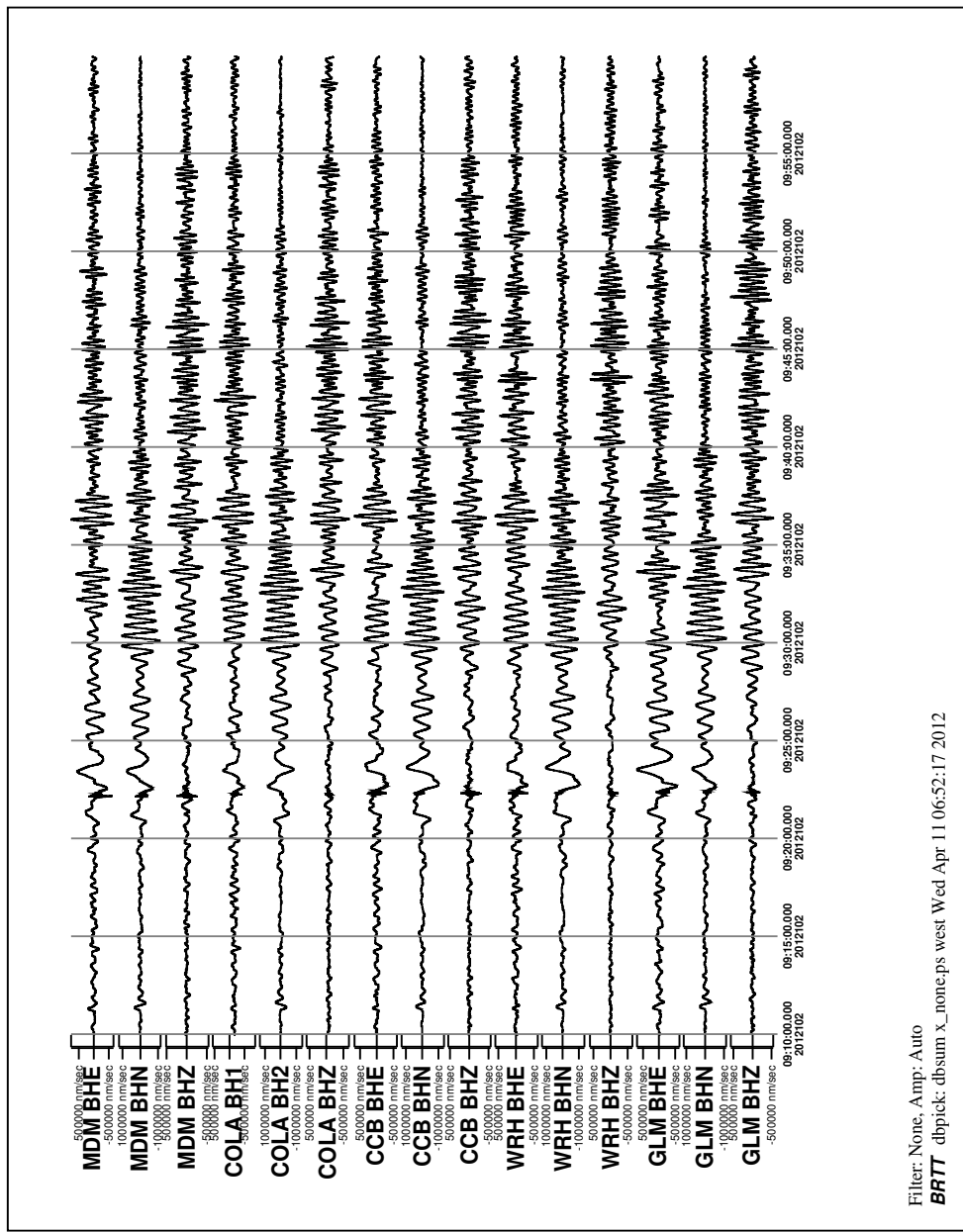


Figure 4.16: The record section showing the raw waveforms at different stations. In this no filters were applied and we can notice the long period surface waves generated by Sumatra earthquake. courtesy: Mike West

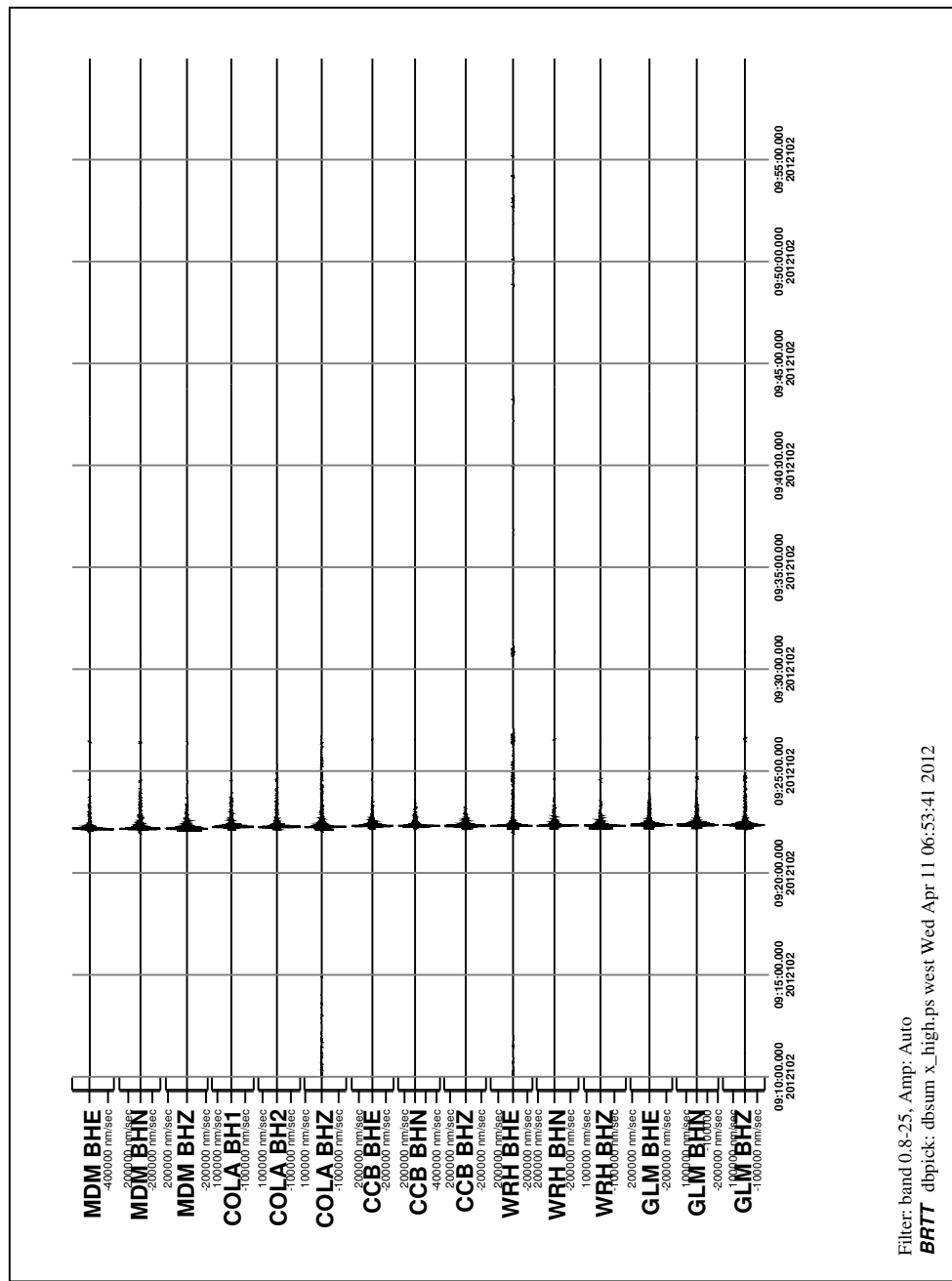


Figure 4.17: When a filter of 0.2-2.5 Hz was applied, we were able to remove the effect of sumatra earthquake at long period, and hence could clearly notice the Nenana basin event occurring at around 0922 UTC. courtesy: Mike West

4.6.5 Tectonic setting

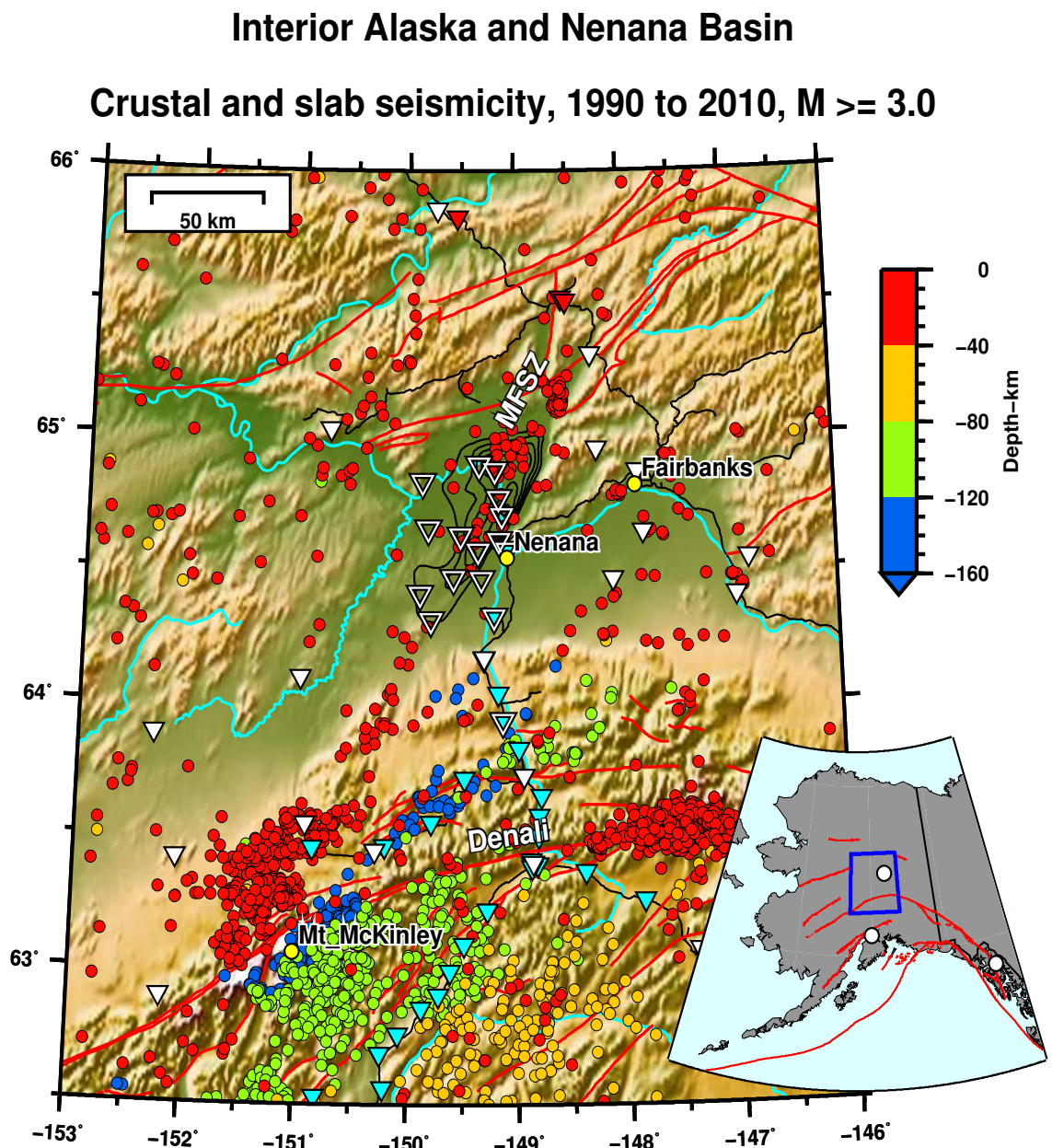


Figure 4.18: Map showing Interior Alaska (where TACTMOD structural model is used); black contour line shows Nenana Basin.

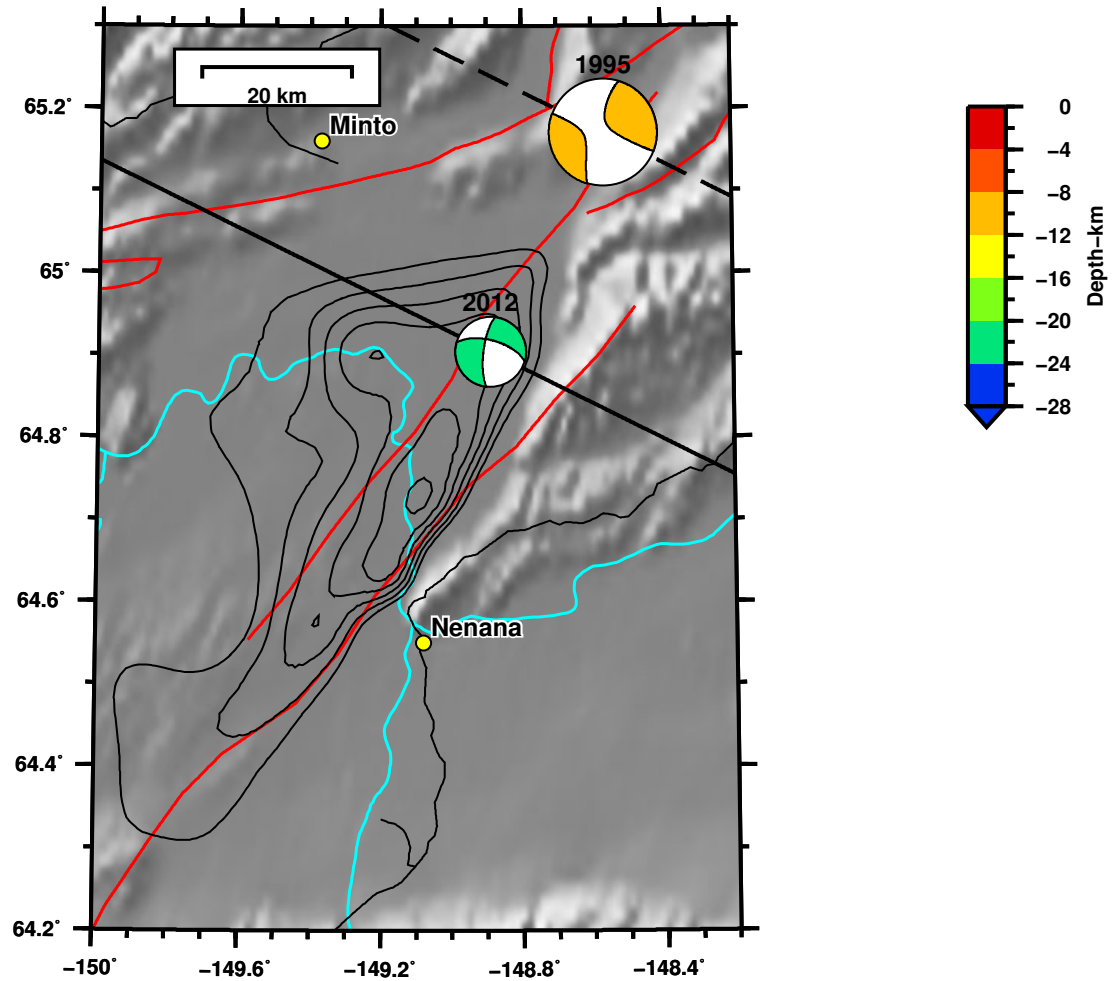


Figure 4.19: Map showing 2012 and 1995 Nenana events, both occurring on the same fault. By CAP moment tensor estimation of 2012 event we have estimated that it also had almost the same focal mechanism.

4.6.6 CAP_MT inversion

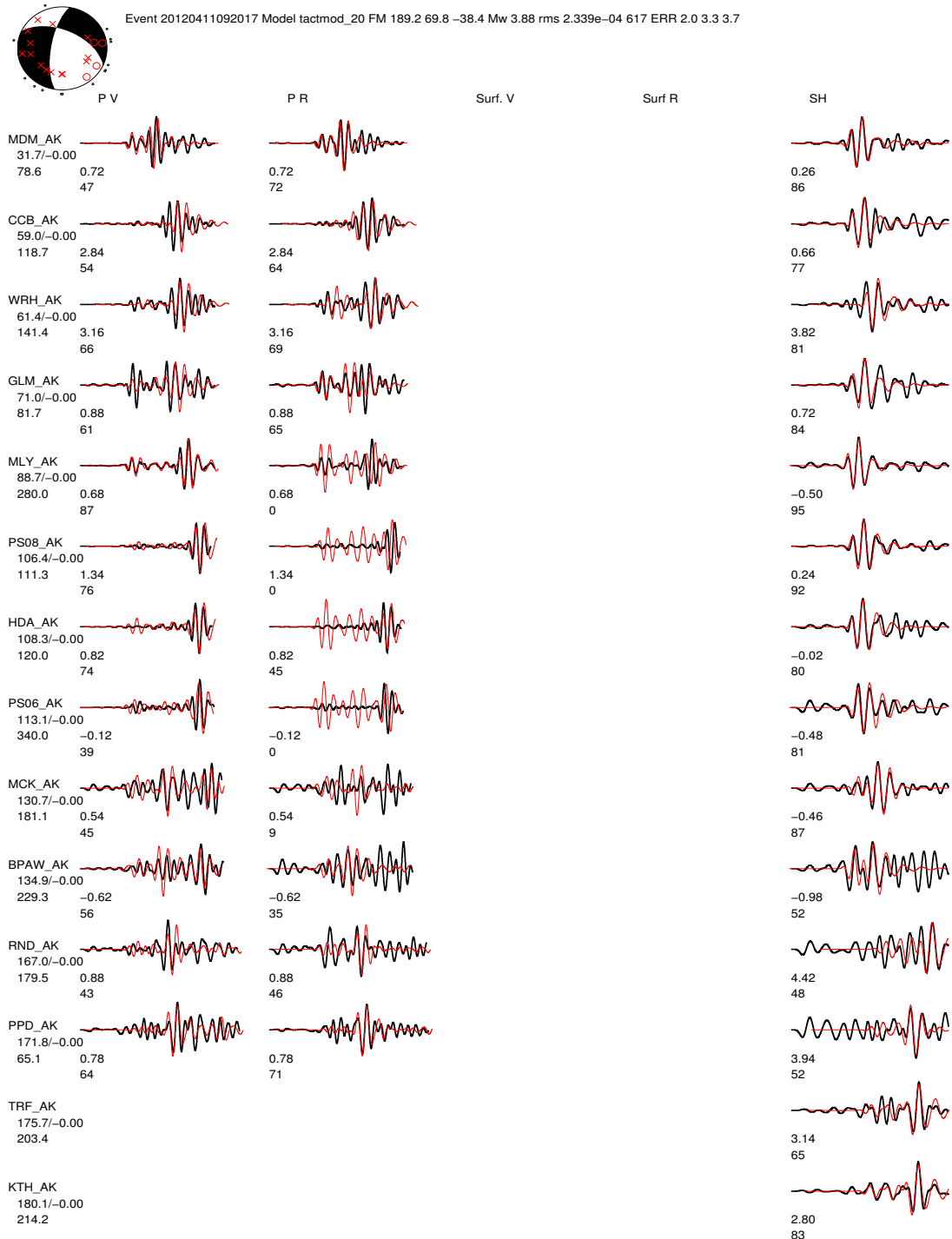


Figure 4.20: CAP inversion of 2012 Nenana event. The Pnl V and R time windows have been extended, such that they contain both Pnl and Rayleigh wave part

Depth estimation

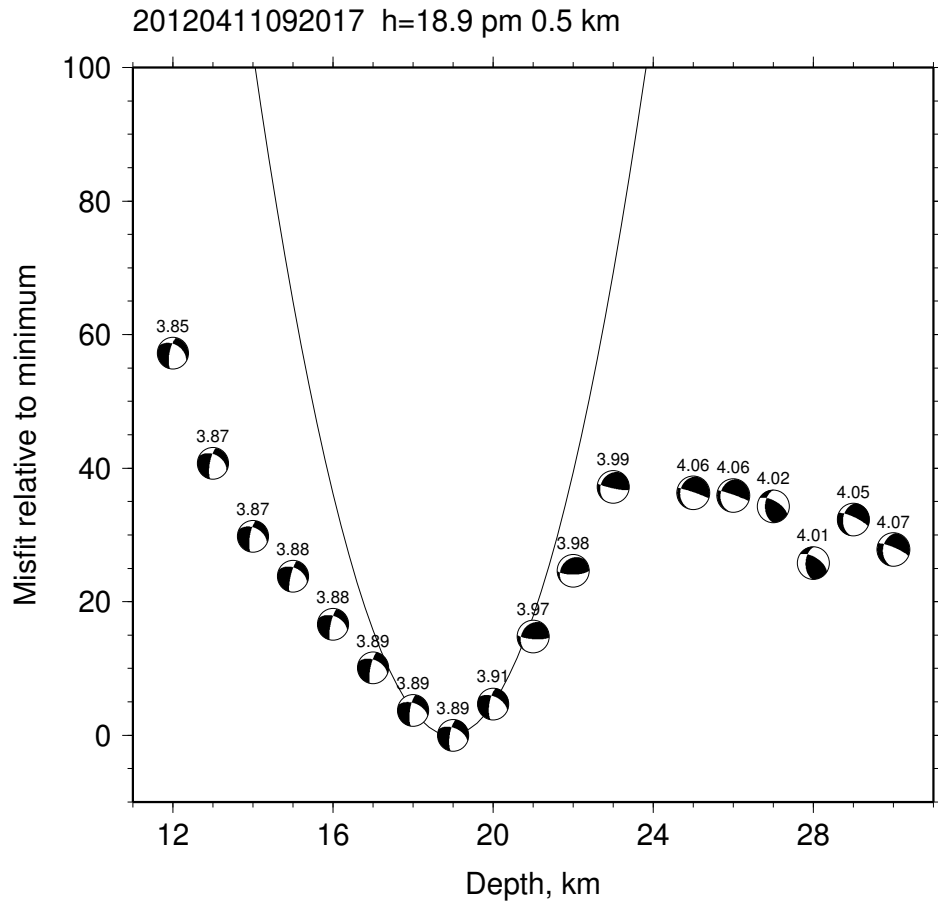


Figure 4.21: Depth estimation by finding the minimum misfit solution after running CAP at different depths. Results match well with AEIC earthquake catalog depth.

Chapter 5

Results and Conclusions

319605								
	strike	dip	rake	Mw	depth	lat	lon	otime
AEIC	204	41	-84	4.6	45	61.45	-149.74	2009-04-07 20:12:55
CAP (surf)	198	49	-83	4.57	45			
CAP (body)	206	47	-67	4.59	43			
CAP (both)	200	49	-78	4.56	45			
289317								
	strike	dip	rake	Mw	depth	lat	lon	otime
AEIC	70	58	54	5	165	61.07	-152.64	2008-03-14 09:38:21
CAP (surf)	60	60	23	5.06	143			
CAP (body)	64	67	33	4.96	141			
CAP (both)	60	67	31	4.98	145			
Nenana 2012								
	strike	dip	rake	Mw	depth	lat	lon	otime
AEIC	-	-	-	-	20	64.9	-148.8	2012-04-11 09:21:00
CAP (surf)	-	-	-	-	-			
CAP (body)	200	84.6	-15.4	3.8	30			
CAP (both)	189	69.8	-38.4	3.88	19			

We have estimated the Moment tensor solutions for three main events. These are important from the perspective of testing the robustness of Cut-and-paste approach. For eid 289317 we can clearly see that our result is much more stable than that provided by AEIC. With the additional advantage of applying different filters for body and surface waves, we are able to use more stations. For 289317, the depth estimation also presented with result similar to AEIC catalog (not AEIC_MT). Working on the similar guidelines, we are preparing an extended study of all Alaska events to develop an improved moment tensor catalog.

For a complex structural model such as that of Alaska, compensation of imperfect green's function by just time shifting the waveforms is not enough. In the next step of improvement of focal mechanism solution, it would be worthwhile to consider 3D structural model. *Liu et al.* (2004) have done a similar study for 3D structural model of Souther California, and using synthetics generated by spectral element method (instead of Fk-synthetics).

The **tshift** parameter can be utilized for improving the structural model and preparing the tomographic maps. In this study, we have not included the non-double couple component (isotropic and CLVD) of moment tensor. CAP does provide an additional option of doing this. These tests and improvements will be carried out in future studies.

Appendix A

Theory on solution of seismic waves through Propagator Matrix Method

A.1 Seismic Waves

For a source far away, the wavefronts coming at the receiver can be looked upon as plane wave. On the other hand, for seismic waves generated by a near source should be examined properly by considering a spherical wavefront. By far and near source it should be remembered that it refers to number of wavelengths between source and receiver, thus at higher frequency even at near source it could be considered as plane wave. Seismic wave are solution of second order partial differential equation. For a solving a radially outwards propagating wave (spherical wavefront) it is quite natural to use a cylindrical or spherical coordinate system.

1. Cartesian

$$\frac{\partial^2 u}{\partial x^2} + \frac{\partial^2 u}{\partial y^2} + \frac{\partial^2 u}{\partial z^2} = \frac{1}{c^2} \frac{\partial^2 u}{\partial t^2} \quad (\text{A.1})$$

2. Cylindrical Writing the Helmholtz equation:

$$\frac{\partial^2 \Phi}{\partial r^2} + \frac{1}{r} \frac{\partial \Phi}{\partial r} + \frac{1}{r^2} \frac{\partial^2 \Phi}{\partial \phi^2} + \frac{\partial^2 \Phi}{\partial z^2} + k_\alpha^2 \Phi = 0 \quad (\text{A.2})$$

Considering the case of axial symmetry the equation can be reduced to:

$$\frac{\partial^2 R}{\partial x^2} + \frac{1}{x} \frac{\partial R}{\partial x} + R = 0 \quad (\text{A.3})$$

which is a differential Bessel equation for $n = 0$, presented by J_n .

A.1.1 Surface wave dispersion (*Aki and Richards, 1980*)

Basically there are two types of seismic waves only, P and S wave. S can be decomposed into SV and SH. Given the free surface condition, P and SV together form Rayleigh wave, whereas, the Love waves results from SH (provided the medium is vertically stratified). When we will be considering these elastic waves the spatial variation of $\lambda(x)$, $\mu(x)$ and $\rho(x)$ won't be utilized for defining of wavefields. Only the their vertical gradient will be used. (1-Dimensional structural model). This a good approximation because if the these horizontal gradient are very small, then the waves traveling at local P and S wavespeeds can still exist but they are coupled to each other by gradients of $\lambda(x)\mu(x)$ and $\rho(x)$ (Kennett, 2000).

It is more sensible to represent the surface as function of wavenumber and frequency, because the dispersive nature of surface wave causes frequency dependent wavenumber. For a particular frequency there are n different wavelengths $k_0 > k_1 > k_2 \dots$ and $c_0 < c_1 < c_2 \dots$. These are called surface waves of different modes. The waves which are function of (x, t) can be converted to function of k and ω by taking double fourier transform over them. Let us consider a case of monochromatic wave. From the figures we can infer that if the depth of top layer increases, waves of higher wavelength are recorded. Similary if the there is larger difference in velocity of consecutive layers more waves of decreasing wavenumber are recorded. Here only single frequency was considered and discrete values of wavelength (k_n) are observed.

Considering the case of a single layer (ρ_1, μ_1) over a homogeneous half space (ρ_2, μ_2) . Solution of different phase-velocity eigenvalues c_n (and thus wavenumber eigenvalues k_n) can be obtained by:

$$F(c) = \tan \omega H \sqrt{\frac{1}{\beta_1^2} - \frac{1}{c^2}} - \frac{\mu_2}{\mu_1} \frac{\sqrt{\frac{1}{c^2} - \frac{1}{\beta_1^2}}}{\sqrt{\frac{1}{\beta_1^2} - \frac{1}{c^2}}} \quad (\text{A.4})$$

Figure (A.1) shows solution of of this equation for different set of values of β_1 , β_2 and H .

A.1.2 Displacement-Stress vector (*Aki and Richards, 1980*)

Let us first consider the propagation of surface waves:

$$\mathbf{u}(x, y, z, t) = \mathbf{Z}(z) \exp[i(kx - \omega t)] \quad (\text{A.5})$$

$\mathbf{Z}(z)$ represent the amplitude variation with depth, as the attenuate much faster along z -axis.

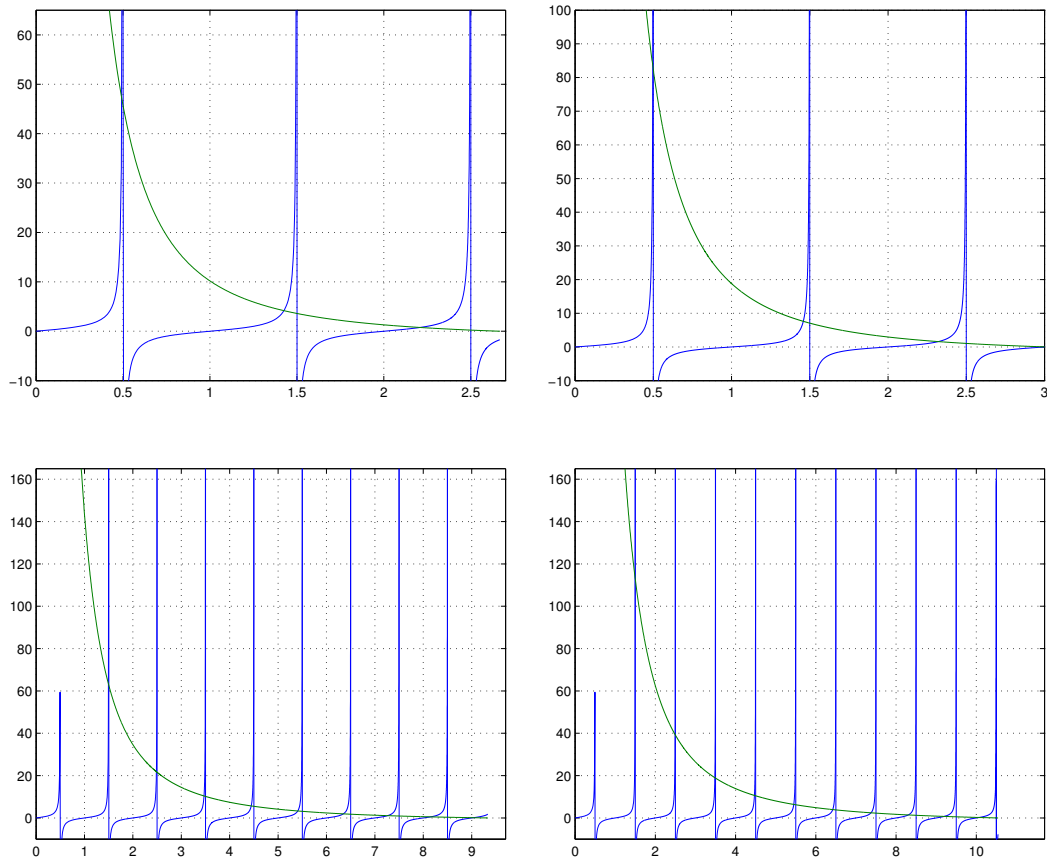


Figure A.1: Love wave dispersion in a single layer over half sapce. Solution of equation (A.4) for different values of β_1 , β_2 and H . The figure shows different k_n included for a given frequency. (Top left) $\beta_1 = 3$ and $\beta_2 = 5$ and depth $H=10$ kms. (Top right) $\beta_1 = 3$ and $\beta_2 = 7$ and depth $H=10$ kms (Bottom left) $\beta_1 = 3$ and $\beta_2 = 5$ and depth $H=35$ kms (Top right) $\beta_1 = 3$ and $\beta_2 = 7$ and depth $H=35$ kms.

Equation of motion:

$$\rho \ddot{u}_i = f_i + \tau_{ji,j} \quad (\text{A.6})$$

Equation of love wave:

$$u = 0 \quad (\text{A.7})$$

$$v = l_1(k, z, \omega) \exp[i(kx - \omega t)] \quad (\text{A.8})$$

$$w = 0 \quad (\text{A.9})$$

The associated stress components can be described as:

$$\tau_{xx} = \tau_{yy} = \tau_{zz} = \tau_{zx} = 0 \quad (\text{A.10})$$

$$\tau_{yz} = \mu \frac{dl_1}{dz} \exp[i(kx - \omega t)] \quad (\text{A.11})$$

$$\tau_{xy} = ik\mu l_1 \exp[i(kx - \omega t)] \quad (\text{A.12})$$

Equation of motion for this love wave $l_1(k, z, \omega)$ can be represented as:

$$-\omega^2 \rho(z) l_1 = \frac{d}{dz} \left[\mu(z) \frac{dl_1}{dz} \right] - k^2 \mu(z) l_1 \quad (\text{A.13})$$

As the discontinuities as assumed to be present only the horizontal plane, the stress component in (y, z) plane is also continuous and can be represented as:

$$\tau_{yz} = l_2(k, z, \omega) \exp[i(kx - \omega t)] \quad (\text{A.14})$$

Then we can write (A.12) and (A.13) as:

$$\frac{dl_1}{dz} = \frac{l_2}{\mu(z)} \quad (\text{A.15})$$

$$\frac{dl_2}{dz} = (k^2 \mu(z) - \omega^2 \rho(z)) l_1 \quad (\text{A.16})$$

In matrix form:

$$\boxed{\frac{d}{dz} \begin{pmatrix} l_1 \\ l_2 \end{pmatrix} = \begin{pmatrix} 0 & \mu(z)^{-1} \\ k^2 \mu(z) - \omega^2 \rho(z) & 0 \end{pmatrix} \begin{pmatrix} l_1 \\ l_2 \end{pmatrix}} \quad (\text{A.17})$$

This representation in (k, ω) is obtained by the double fourier transform of (x, t) and it describes general SH particle motion along y -axis.

Equation for Rayleigh wave

$$u = r_1(k, z, \omega) \exp[i(kx - \omega t)] \quad (\text{A.18})$$

$$v = 0 \quad (\text{A.19})$$

$$w = ir_2(k, z, \omega) \exp[i(kx - \omega t)] \quad (\text{A.20})$$

r_1 and r_2 have opposite sign and thus i in w creates a retrograde motion. i comes due to $\frac{\pi}{2}$ phase shift in z component of displacement.

The stress components are:

$$\tau_{yz} = \tau_{xy} = 0 \quad (\text{A.21})$$

$$\tau_{xx} = i \left[\lambda \frac{dr_2}{dz} + k(\lambda + 2\mu)r_1 \right] \exp[i(kx - \omega t)] \quad (\text{A.22})$$

$$\tau_{yy} = i \left[\lambda \frac{dr_2}{dz} + k\lambda r_1 \right] \exp[i(kx - \omega t)] \quad (\text{A.23})$$

$$\tau_{xx} = i \left[(\lambda + 2\mu) \frac{dr_2}{dz} + k\lambda r_1 \right] \exp[i(kx - \omega t)] \quad (\text{A.24})$$

$$\tau_{xx} = \mu \left[\frac{dr_1}{dz} - kr_2 \right] \exp[i(kx - \omega t)] \quad (\text{A.25})$$

$$(A.26)$$

Stress component τ_{zx} and τ_{zz} are continuous in z . Therefore:

$$\tau_{zx} = r_3(k, z, \omega) \exp[i(kx - \omega t)] \quad (\text{A.27})$$

$$\tau_{zz} = ir_4(k, z, \omega) \exp[i(kx - \omega t)] \quad (\text{A.28})$$

Like the differential equation for love wave (SH) in (A.17), the similar for Rayleigh can be obtained to be:

$$\boxed{\frac{d}{dz} \begin{pmatrix} r_1 \\ r_2 \\ r_3 \\ r_4 \end{pmatrix} = \begin{pmatrix} 0 & k & \mu^{-1}(z) & 0 \\ -k\lambda(z)[\lambda(z) + 2\mu(z)]^{-1} & 0 & 0 & [\lambda(z) + 2\mu(z)]^{-1} \\ k^2\zeta(z) - \omega^2\rho(z) & 0 & 0 & -k\lambda(z)[\lambda(z) + 2\mu(z)] \\ 0 & -\omega^2\rho(z) & -k & 0 \end{pmatrix} \begin{pmatrix} r_1 \\ r_2 \\ r_3 \\ r_4 \end{pmatrix}} \quad (\text{A.29})$$

where $\zeta(z) = 4\mu(z)[\lambda(z) + \mu(z)]/[\lambda(z) + 2\mu(z)]$.

The above equations (A.29) and (A.17) can be solved for the displacement components l_1, r_1 and r_2 but these are not the solution to the wave equation.

Boundary Conditions There are two types of boundary conditions usually considered in seismology:

1. Kinematic boundary condition : Concerning with displacement
2. Dynamic boundary condition : concerning with traction

For surface waves there won't be any stress component at free surface and at infinity depth the displacement will tend to zero.

$$r_1 \rightarrow 0, r_2 \rightarrow 0, \text{ and } l_1 \rightarrow 0 \text{ as } z \rightarrow \infty \quad (\text{A.30})$$

$$r_3 = r_4 = l_2 = 0 \text{ at the free surface } (z = z_0) \quad (\text{A.31})$$

In addition to these, the displacement and the traction must be continuous at layer boundaries where there is discontinuity in elastic parameters otherwise it would also act as another secondary seismic source (*Aki and Richards*, 1980).

A.1.3 Propagator Matrix(*Udias*, 1999)

Equations (A.17) and A.29) can be written imatrix form as:

$$\frac{d\mathbf{b}(z)}{dz} = \mathbf{A}(c, z)\mathbf{b}(z) \quad (\text{A.32})$$

In case the layers for constant elastic modulii are taken, our matrix \mathbf{A} will depend only on c and ω and not z inside the layer. Let us take a refernce depth $z = z_0$ (usually free surface). Displacement-stress vector at this plane is $\mathbf{b}(z_0)$. We can normalize the problem such that $\mathbf{b}(z_0) = \mathbf{I}$. Now we define a new matrix $\mathbf{P}(z, z_0)$ which is the solution of above equation in normalized form, such that if $\mathbf{b}(z)$ is the solution before normalization, the normalized solution for depth z will be $\mathbf{P}(z, z_0)$.

$$\mathbf{P}(z, z_0) = \mathbf{b}^{-1}(z_0)\mathbf{b}(z) \quad (\text{A.33})$$

Now if there is an intermediate level z_1, z_2, z_3, \dots upto z_n , we can write:

$$\mathbf{P}(z, z_0) = \mathbf{b}^{-1}(z_0)\mathbf{b}(z) \quad (\text{A.34})$$

$$= \mathbf{b}^{-1}(z_0)\mathbf{b}^{(z_1)}\mathbf{b}^{-1}(z_1)\mathbf{b}(z) \quad (\text{A.35})$$

$$= [\mathbf{b}^{-1}(z_0)\mathbf{b}^{(z_1)}][\mathbf{b}^{-1}(z_1)\mathbf{b}(z)] \quad (\text{A.36})$$

$$= \mathbf{P}(z_1, z_0)\mathbf{P}(z, z_1) \quad (\text{A.37})$$

Similary,

$$\mathbf{P}(z_n, z_0) = \prod_{i=1}^n \mathbf{P}(z_i, z_{i-1}) \quad (\text{A.38})$$

Now we can relate the displacement-stress vector for level n , $\mathbf{b}(z_n)$ to that of

reference level $\mathbf{b}(z_0)$:

$$\mathbf{b}(z_n) = \prod_{i=1}^n \mathbf{P}(z_i, z_{i-1}) \mathbf{b}(z_0) \quad (\text{A.39})$$

We can see that by knowing the value of $\mathbf{b}(z_0)$ at reference level we can determine the value of $\mathbf{b}(z_n)$ displacement-stress vector at n -th level by using this $\mathbf{P}(z, z_0)$ matrix. For this reason this matrix $\mathbf{P}(z, z_0)$ is known as Propagator-matrix or Thomson-Haskell Propagator matrix (*Haskell*, 1964).

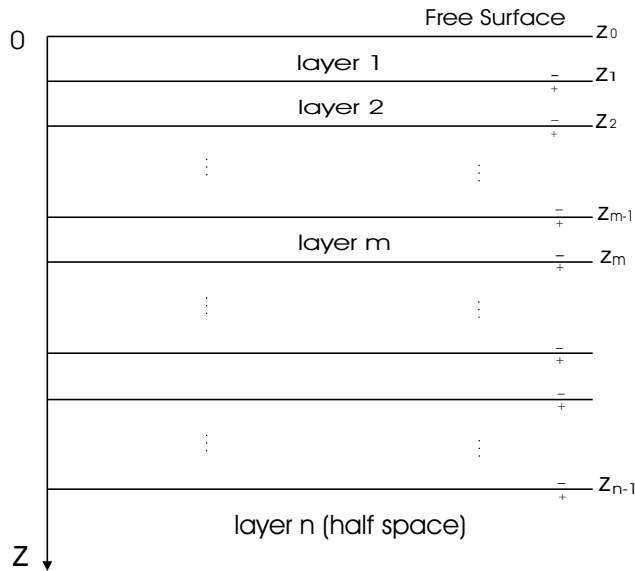


Figure A.2: Stratified layers over a half-space

Evaluating Propagator Matrix Using equation (A.32) for layers of constant elastic parameters we can integrate this equation within the limits z_0 and z .

$$\frac{d\mathbf{b}(z)}{dz} = \mathbf{A}\mathbf{b}(z) \quad (\text{A.40})$$

$$\int_{z_0}^z \frac{d\mathbf{b}(z)}{\mathbf{b}(z)} = \mathbf{A} \int_{z_0}^z dz \quad (\text{A.41})$$

$$\mathbf{b}(z) = e^{(z-z_0)\mathbf{A}} \mathbf{b}(z_0) \quad (\text{A.42})$$

Comparing this with equation (A.33), we can see that the exponential term in the above equation is same as $\mathbf{P}(z, z_0)$. Therefore:

$$\mathbf{P}(z, z_0) = e^{(z-z_0)\mathbf{A}} \quad (\text{A.43})$$

The exponent of a matrix can be calculated by using Jordan decomposition of \mathbf{A} . If \mathbf{A} is composed of independent vectors it can be decomposed in a following way:

$$\mathbf{A} = \mathbf{E}\mathbf{J}\mathbf{E}^{-1} \quad (\text{A.44})$$

where \mathbf{E} is a similarity matrix composed of eigenvectors and \mathbf{J} is the Jordan canonical form of \mathbf{A} whose diagonal elements are eigenvalues of \mathbf{A} . Now we can write the exponential terms :

$$e^{(z-z_0)\mathbf{A}} = \mathbf{E}e^{(z-z_0)\mathbf{J}}\mathbf{E}^{-1} \quad (\text{A.45})$$

Substituting the value of \mathbf{A} in equation (A.42) we get:

$$\mathbf{b}(z) = [\mathbf{E}e^{z\mathbf{J}}\mathbf{E}^{-1}]\mathbf{b}(z_0) = \mathbf{P}(z, z_0)\mathbf{b}(z_0) \quad (\text{A.46})$$

Finding the value of \mathbf{E} and \mathbf{J} : (*Zhu and Rivera, 2002*)

1. The eigenvalues for Love Waves and SH waves can be as follows using equation (A.17):

$$|\mathbf{A} - \lambda\mathbf{I}| = \begin{vmatrix} -\lambda & \mu^{-1} \\ k^2\mu - \omega^2\rho & -\lambda \end{vmatrix} = 0 \quad (\text{A.47})$$

This gives us eigenvalues $\lambda = \pm\sqrt{k^2 - \omega^2/\beta^2} = \pm\nu_\beta$.

For these values of λ we get 2 eigenvectors:

$$\begin{aligned} u^1 &= [-1, \mu \frac{\nu_\beta}{k}] \\ u^2 &= [1, \mu \frac{\nu_\beta}{k}] \end{aligned}$$

This yields to:

$$\mathbf{E} = \begin{bmatrix} -1 & 1 \\ \mu \frac{\nu_\beta}{k} & \mu \frac{\nu_\beta}{k} \end{bmatrix} \quad (\text{A.48})$$

$$\mathbf{J} = \begin{bmatrix} -\mu_\beta & 0 \\ 0 & \mu_\beta \end{bmatrix} \quad (\text{A.49})$$

$$e^{(z-z_0)\mathbf{J}} = \begin{bmatrix} e^{-\mu_\beta(z-z_0)} & 0 \\ 0 & e^{\mu_\beta(z-z_0)} \end{bmatrix} \quad (\text{A.50})$$

$$\mathbf{E}^{-1} = \begin{bmatrix} -1 & \frac{k}{\mu\nu_\beta} \\ 1 & \frac{k}{\mu\nu_\beta} \end{bmatrix} \quad (\text{A.51})$$

By substituting these values we can get the calculate the propagator matrix:

$$\boxed{\mathbf{P}(z, z_0) = e^{(z-z_0)} \mathbf{A} = \mathbf{E} e^{(z-z_0)} \mathbf{J} \mathbf{E}^{-1} = \begin{bmatrix} C_\beta & -\frac{Y_\beta}{\mu} \\ -\mu X_\beta & C_\beta \end{bmatrix}} \quad (\text{A.52})$$

where $C_\beta = \cosh(\nu_\beta(z - z_0))$, $X_\beta = \mu_\beta \sinh(\nu_\beta(z - z_0))/k$ and $Y_\beta = k \sinh(\nu_\beta(z - z_0))/\nu_\beta$.

Now if our point z lies in n -th layer, using equation (A.38) we can write :

$$\mathbf{P}(z, z_0) = \mathbf{P}(z, z_{n-1}) \mathbf{P}(z, z_{n-2}) \dots \mathbf{P}(z, z_0) \quad (\text{A.53})$$

$$= \exp[(z - z_{n-1}) \mathbf{A}_{n-1}] \prod_{i=1}^{n-1} \exp[(z_i - z_{i-1}) \mathbf{A}_i] \quad (\text{A.54})$$

2. In the same fashion we can obtain the propagator matrix for P-SV motion. From the displacement-stress vector found in equation (A.29) we obtain 4 different eigenvalues $\pm\nu_\alpha$ and $\pm\nu_\beta$, where α and β are compressional and shear velocities and ν_α and ν_β are amplitude decay constants. Thus the Jordan (eigenvalue vector) \mathbf{J} is:

$$\mathbf{J} = \begin{bmatrix} -\nu_\alpha & 0 & 0 & 0 \\ 0 & -\nu_\beta & 0 & 0 \\ 0 & 0 & \nu_\alpha & 0 \\ 0 & 0 & 0 & \nu_\beta \end{bmatrix} \quad (\text{A.55})$$

Now by calculating the eigenvectors we determine \mathbf{E} and \mathbf{E}^{-1} :

$$\mathbf{E} = \begin{bmatrix} -1 & -\frac{\nu_\beta}{k} & 1 & \frac{\nu_\beta}{k} \\ \frac{\nu_\alpha}{k} & 1 & \frac{\nu_\alpha}{k} & 1 \\ -2\mu\gamma_1 & -2\mu\frac{\nu_\beta}{k} & 2\mu\gamma_1 & 2\mu\frac{\nu_\beta}{k} \\ 2\mu\frac{\nu_\alpha}{k} & 2\mu\gamma_1 & 2\mu\frac{\nu_\alpha}{k} & 2\mu\gamma_1 \end{bmatrix} \quad (\text{A.56})$$

$$\mathbf{E}^{-1} = \frac{\gamma}{2} \begin{bmatrix} -1 & -\gamma \frac{k}{\nu_\alpha} & \frac{1}{2\mu} & \frac{k}{2\mu\nu_\alpha} \\ \gamma_1 \frac{k}{\nu_\beta} & 1 & -\frac{k}{2\mu\nu_\beta} & -\frac{1}{2\mu} \\ 1 & -\gamma_1 \frac{k}{\nu_\alpha} & -\frac{1}{2\mu} & \frac{k}{2\mu\nu_\alpha} \\ -\gamma_1 \frac{k}{\nu_\beta} & 1 & \frac{k}{2\mu\nu_\beta} & -\frac{1}{2\mu} \end{bmatrix} \quad (\text{A.57})$$

where $\gamma = 2k^2\beta^2/\omega^2$ and $\gamma_1 = 1 - 1/\gamma$.

Using these values of \mathbf{J} , \mathbf{E} and \mathbf{E}^{-1} we can compute propagator matrix for P-SV motion. Let us consider for the n -th layer. By using propagator matrix we can relate the displacement-stress vector at top and bottom of layer:

$$\mathbf{b}(z_n) = \mathbf{P}(z_n, z_{n-1})\mathbf{b}(z_{n-1}) \quad (\text{A.58})$$

For this case we can compute propafator matrix using the values computed for \mathbf{J} , \mathbf{E} and \mathbf{E}^{-1} .

$$\begin{aligned} \mathbf{P}(z_n, z_{n-1}) &= \mathbf{E} e^{(z_n - z_{n-1})\mathbf{J}} \mathbf{E}^{-1} \\ &= \gamma \begin{bmatrix} C_\alpha - \gamma_1 C_\beta & \gamma_1 Y_\alpha - X_\beta & \frac{C_\beta - C_\alpha}{2\mu} & \frac{X_\beta - Y_\alpha}{2\mu} \\ \gamma_1 Y_\beta - X_\alpha & C_\beta - \gamma_1 C_\alpha & \frac{X_\alpha - Y_\beta}{2\mu} & \frac{C_\alpha - C_\beta}{2\mu} \\ 2\mu\gamma_1(C_\alpha - C_\beta) & 2\mu(\gamma_1^2 Y_\alpha - X_\beta) & C_\beta - \gamma_1 C_\alpha & X_\beta - \gamma_1 Y_\alpha \\ 2\mu(\gamma_1^2 Y_\beta - X_\alpha) & 2\mu\gamma_1(\beta - C_\alpha) & X_\alpha - \gamma_1 Y_\beta & C_\alpha - \gamma_1 C_\beta \end{bmatrix} \end{aligned} \quad (\text{A.59})$$

where $C_\beta = \cosh(\nu_\beta(z - z_0))$, $X_\beta = \mu_\beta \sinh(\nu_\beta(z - z_0))/k$ and $Y_\beta = k \sinh(\nu_\beta(z - z_0)/\nu_\beta)$ and similarly for C_α , X_α and Y_α . $d = z_n - z_{n-1}$ is the thickness of n -th layer.

Bibliography

- Aki, K., and P. G. Richards (1980), *Quantitative Seismology, Theory and Methods*, W. H. Freeman, San Francisco, Calif., USA.
- Brocher, T. M., G. S. Fuis, M. A. Fisher, G. Plafker, M. J. Moses, J. J. Taber, and N. I. Christensen (1992), Thin, low-velocity crust beneath the southern yukon-tanana terrane, east central alaska: Results from trans-alaska crustal transect refraction/wide-angle reflection data, *J. Geophys. Res.*, 97, 1921–1942.
- Haskell, N. A. (1953), The dispersion of surface waves on multilayered media, *Bulletin of the Seismological Society of America*, 43, 17–34.
- Haskell, N. A. (1964), Radiation pattern of surface waves from point sources in a multilayered medium, *Bull Seismol Soc Am*, 54(1), 377.
- Jost, M., and R. Herrmann (1989), A students guide to and review of moment tensors, *Seismological Research Letters*, 60(2), 3757.
- Kanamori, H. (1977), The energy release in great earthquakes, *Journal of Geophysical Research*, 82(20), 2981–2987.
- Kennett, B. L. N. (2000), *Seismic Wave Propagation in Stratified Media*, ANU E Press, Caneberra, Australia.
- Liu, Q., J. Polet, D. Komatitsch, and J. Tromp (2004), Spectral-element moment tensor inversion for earthquakes in southern california, *Bulletin of the Seismological Society of America*, 94(5), 1748–1761.
- Matumoto, T., and R. A. Page (1969), Microaftershocks following the alaska earthquake of 28 march 1964: Determination of hypocenters and crustal velocities in the kenai peninsula-prince william sound area, the prince william sound, alaska, earthquake of 1964 and aftershocks, *U.S. Govt. Printing Office, Washington*, 10(3), 157–173.
- Savage, B., and D. V. Helmberger (2004), Site response from incident *pnl* waves, *Bulletin of the Seismological Society of America*, 94(1), 357–362.

- Slawinski, M. A. (2010), *Waves and Rays in Elastic Continua*, World Scientific Publishing Co. Pte. Ltd.
- Stein, S., and M. Wysession (2005), *An Introduction to Seismology, Earthquakes, and Earth Structure*, Blackwell Publishing.
- Thomson, W. T. (1950), Transmission of elastic waves through a stratified solid medium, *J. App. Phy.*, 21, 89–93.
- Udias, A. (1999), *Principles of Seismology*, Cambridge Univ. Press, Cambridge, United Kingdom.
- Wang, C. Y., and R. B. Herrmann (1980), A numerical study of p-, sv-, and sh-wave generation in a plane layered medium, *Bulletin of the Seismological Society of America*.
- Zhao, L. S., and D. V. Helmberger (1994), Source estimation from broadband regional seismograms, *Bulletin of the Seismological Society of America*, 84(1), 91–104.
- Zhu, L., and D. V. Helmberger (1996), Advancement in source estimation techniques using broadband regional seismograms, *Bulletin of the Seismological Society of America*, 86(5), 1634–1641.
- Zhu, L., and L. A. Rivera (2002), A note on the dynamic and static displacements from a point source in multilayered media, *Geophysical Journal International*, 148(3), 619–627.